Dry Rolling Friction and Wear of Elastomer Systems and Their Finite Element Modelling

Beim Fachbereich für Maschinenbau und Verfahrenstechnik

der Technischen Universität Kaiserslautern

zur Erlangung des akademischen Grades

Doktor-Ingenieur (Dr.-Ing.)

genehmigte Dissertation

von

M. Eng. Dan Xu

aus Liaoning, China

Tag der mündlichen Prüfung:	09 November 2009
Prüfungsvorsitzender:	Prof. Dr.-Ing. P.-L. Geiß
1. Berichterstatter:	Prof. Dr.-Ing. habil. Dr.h.c. J. Karger-Kocsis
2. Berichterstatter:	Prof. Dr.-Ing. B. Sauer

Acknowledgements

The present work was done in the Institute for Composite Materials (Institut für Verbundwerkstoffe GmbH, IVW) of the University of Kaiserslautern, Germany.

Special and sincere thanks to my supervisor Prof. Dr.-Ing habil. Dr.h.c. József Karger-Kocsis. He is a learned man mastering profound knowledge in a wide area. His earnest and very patient supervision led me in the scientific field about polymers and let me fulfill the present work. His goodness and solicitude make me very grateful. He is always ready there for providing help and advices not only for research but also for personal life.

I also thank Prof. Dr. -Ing. A. K. Schlarb for giving me the opportunity to go further with my study in such a good institute in Germany and meet the nice people. He also spent time in reviewing my work and discussing questions even though he was very busy as the leader of the IVW.

I thank as well Prof. Dr.-Ing. B. Sauer for being the co-commentator of the PhD thesis and Prof. Dr.-Ing. P.-L. Geiß for presiding over the examination committee.

I appreciate the time, effort and advices for my work from Dr. D. Felhös. His involvements were very helpful for my experiments. I am thankful to Dr. M. Harrass, A. Gebhard; they helped with the usage of the experimental instruments and measuring devices. Especially A. Gebhard, he did me a great favor when I started in the IVW. His help made the necessary things e.g. registration at the university and city hall done smoothly. I thank Dr. S. Grishchuk, Dr. N. Castella and Dr. L. Sorochynska for their advices to my presentation. I am also grateful to S. Yancey and N. Opitz for their kindness and help in various occasions. I thank all other colleagues in IVW, especially S. Schmitt, H. Giertzsch, J. Stephan, R. Schimmele, M. Hentzel, P. Eichert, P. Volk and H. Plocharzik for their kind support in the experiments. I enjoy my stay in the IVW greatly and appreciate the friendly working environment.

I acknowledge the DFG (German Research Foundation) for the financial support (Graduate school GK 814) of my PhD work in the IVW.

Lastly and most importantly, I thank my parents for their love and support to me.

Content

Abstract

Elastomers and their various composites, and blends are frequently used as engineering working parts subjected to rolling friction movements. This fact already substantiates the importance of a study addressing the rolling tribological properties of elastomers and their compounds. It is worth noting that until now the research and development works on the friction and wear of rubber materials were mostly focused on abrasion and to lesser extent on sliding type of loading. As the tribological knowledge acquired with various counterparts, excluding rubbers, can hardly be adopted for those with rubbers, there is a substantial need to study the latter. Therefore, the present work was aimed at investigating the rolling friction and wear properties of different kinds of elastomers against steel under unlubricated condition.

In the research the rolling friction and wear properties of various rubber materials were studied in home-made rolling ball-on-plate test configurations under dry condition. The materials inspected were ethylene/propylene/diene rubber (EPDM) without and with carbon black (EPDM_CB), hydrogenated acrylonitrile/butadiene rubber (HNBR) without and with carbon black/silica/multiwall carbon nanotube (HNBR_CB/silica/MWCNT), rubber-rubber hybrid (HNBR and fluororubber (HNBR-FKM)) and rubber-thermoplastic blend (HNBR and cyclic butylene terephthalate oligomers (HNBR-CBT)). The dominant wear mechanisms were investigated by scanning electron microscopy (SEM), and analyzed as a function of composition and testing conditions. Differential scanning calorimetry (DSC), dynamic-mechanical thermal analysis (DMTA), atomic force microscopy (AFM), and transmission electron microscopy (TEM) along with other auxiliary measurements, were adopted to determine the phase structure and network-related properties of the rubber systems. The changes of the friction and wear as a function of type and amount of the additives were explored. The friction process of selected rubbers was also modelled by making use of the finite element method (FEM).

The results show that incorporation of filler enhanced generally the wear resistance, hardness, stiffness (storage modulus), and apparent crosslinking of the related rubbers (EPDM-, HNBR- and HNBR-FKM based ones), but did not affect their glass transition temperature. Filling of rubbers usually reduced the coefficient of friction (COF). However, the tribological parameters strongly depended also on the test set-up and test duration.

High wear loss was noticed for systems showing the occurrence of Schallamach-type wavy pattern.

The blends HNBR-FKM and HNBR-CBT were two-phase structured. In HNBR-FKM, the FKM was dispersed in form of large microscaled domains in the HNBR matrix. This phase structure did not change by incorporation of MWCNT. It was established that the MWCNT was preferentially embedded in the HNBR matrix. Blending HNBR with FKM reduced the stiffness and degree of apparent crosslinking of the blend, which was traced to the dilution of the cure recipe with FKM. The coefficient of friction increased with increasing FKM opposed to the expectation. On the other hand, the specific wear rate (W_s) changed marginally with increasing content of FKM.

In HNBR-CBT hybrids the HNBR was the matrix, irrespective to the rather high CBT content. Both the partly and mostly polymerized CBT ((p)CBT and pCBT, respectively) in the hybrids worked as active filler and thus increased the stiffness and hardness. The COF and W_s decreased with increasing CBT content.

The FEM results in respect to COF achieved on systems possessing very different structures and thus properties (EPDM_30CB, HNBR-FKM 100-100 and HNBR-(p)CBT 100-100, respectively) were in accordance with the experimental results. This verifies that FEM can be properly used to consider the complex viscoelastic behaviour of rubber materials under dry rolling condition.

Kurzfassung

Die verbreitete Anwendung von Elastomer-Systemen als Bauteilkomponente, welche der Rollreibung ausgesetzt sind, unterstreicht die Bedeutung von Studien, fokussiert auf die tribologische Untersuchung von Elastomeren gegen verschiedene Gegenkörper. Der Schwerpunkt der bisherigen Foschungen bezüglich Reibung- und Verschleißverhaltens bei Elastmer-Werkstoffen lag bei der Abrasions- und Gleitreibung. Aus diesem Grunde wurde der Schwerpunkt der vorliegender Arbeit auf Rollreibung und -verschleiß von verschiedenen Elastomeren gegen Stahl gelegt.

In dieser Arbeit wurden Rollreibung und -verschleiß von verschiedenen Elastomeren mit Hilfe zwei Arten von Kugel-auf-Platte Prüfstände, welche sich in der Bewegung der Kugel unterscheiden, im Trockenlauf untersucht. Die Materialien waren Ethylen-Propylen-Dien-Kautschuk (EPDM) mit und ohne Rußfüllung, hydrierter Acrylnitril-Butadien-Kautschuk (HNBR) gefüllt mit Ruß, Siliciumdioxid und mehrwändigen Kohlenstoffnanoröhren (MWCNT), gummiartige Hybridsysteme bestehend aus Kautschuk/Kautschuk bzw. Kautschuk/Thermoplast Kombinationen (Mischung aus HNBR und Fluorelastomer (HNBR-FKM), bzw. aus HNBR und zyklischen Butylen Terephthalat Oligomeren (HNBR-CBT)). Die Versagensmechanismen beim Rollverschleiß wurden durch Untersuchungen der Verschleißflächen mittels Rasterelektronenmikroskop (REM) analysiert, und in Abhängigkeit der Rezeptur und Untersuchungsbedingungen analysiert. Dynamische Differenzkalorimetrie, dynamisch-mechanische Thermoanalyse (DMTA), Rasterkraftmikroskopie (AFM) und Transmissionselektronenmikroskopie (TEM), zusammen mit anderen Hilfstechniken wurden zur Bestimmung der Phasenstruktur und Netzwerk-Eigenschaften von den untersuchten Systemen verwendet. Die eingesetzten Änderungen bei Rollreibung und -verschleiß als Funktion des Elastomertyps und Menge der Füllstoffe wurden untersucht. Der Reibungsvorgang von ausgewählten Elastomeren wurde auch mit Hilfe der Methode der finiten Elemente (FE) modellhaft untersucht.

Die Ergebnisse zeigen, dass die Zugabe von Füllstoffen die Reibung, der Verschleißwiderstand, die Härte, die Steifigkeit (Speichermodul) und die Vernetzung der jeweiligen Elastomere (EPDM-, HNBR- und HNBR-FKM basierend) verbessert, aber keine Auswirkung auf ihre Glasübergangstemperatur hat. Die Füllstoffzugabe ermäßigt normalerweise den Reibungskoeffizient. Anderseits zeigten die tribologischen Parameter

eine starke Abhängigkeit von dem Maschinentyp und der Prüfungsdauer. Mit dem Auftritt der Schallamach-Muster erhöhte sich die Verschleißrate.

Bei den Mischungen (HNBR-FKM und HNBR-CBT) liegt eine Zweiphasenstruktur vor. Der Fluorelastomer im HNBR-FKM ist in Form von großen Mikrodomänen in der HNBR Matrix eingebettet. Diese Struktur verändert sich durch die Additivierung mit MWCNT nicht, die MWCNT wird bevorzugt in die HNBR-Matrix eingebaut. Durch die Zumischung von FKM verschlechtert sich die Steifigkeit und reduziert sich die Vernetzungsdichte der HNBR-FKM-Mischungen (infolge einer „Verdünnung“ der Vernetzungsadditive durch die Zugabe von FKM). Je höher der Anteil an Fluorelastomer ist, desto kleiner wird die Vernetzungsdichte. Der Reibungskoeffizient steigt mit zunehmendem Anteil an Fluorelastomer an. Die spezifische Verschleißrate ändert sich jedoch nur geringfügig. Die dynamisch mechanischen Eigenschaften stellen nicht die Summe der Einzeleigenschaften dar.

Im Hybrid HNBR-CBT übernimmt HNBR die Rolle der Matrix. Über die Polymerisation von CBT ergibt sich im Sinne eines aktiven Füllstoffes eine deutliche Steifigkeitserhöhung. Der Reibungskoeffizient und die spezifische Verschleißrate sinken mit zunehmendem CBT Gehalt der jeweiligen Rezepturen.

Die FEM-Ergebnisse, erzielt an EPDM, HNBR-FKM Mischungen und HNBR-CBT Hybridsystemen stimmen mit den experimentellen Resultaten gut überein. Dies zeigt, dass die FEM zielgerecht eingesetzt werden kann um das komplexe viskoelastische Verhalten von Elastomeren bei Rollreibung zu beschreiben, quantifizieren.

List of Abbreviations and Symbols

Abbreviations

AFM	atomic force microscopy
BR	polybutadiene
CB	carbon black
CBT	cyclic butylene terephthalate oligomers
CNT	carbon nanotube
curedHNBR	cured HNBR
curedHNBR-(p)CBT 100-100	blend composed of 100 part curedHNBR and 100 part (p)CBT
DMTA	dynamic-mechanical thermal analysis
DSC	differential scanning calorimetry
EA TPV	elastomer alloy thermoplastic vulcanizates
EPDM	ethylene/propylene/diene
EPDM_0	unfilled EPDM
EPDM_30	EPDM with 30 phr carbon black
EPDM_45	EPDM with 45 phr carbon black
EPDM_60	EPDM with 60 phr carbon black
FE	finite element
FEM	finite element method
FKM	fluororubber

HNBR	hydrogenated acrylonitrile/butadiene rubber
HNBR_PURE	unfilled HNBR
HNBR_10silica	HNBR with 10 phr silica
HNBR_20silica	HNBR with 20 phr silica
HNBR_30silica	HNBR with 30 phr silica
HNBR_10MWCNT	HNBR with 10 phr MWCNT
HNBR_20MWCNT	HNBR with 20 phr MWCNT
HNBR_30MWCNT	HNBR with 30 phr MWCNT
HNBR_20CB	HNBR with 20 phr carbon black
HNBR-FKM	blend composed of HNBR and FKM
HNBR-FKM 100-33.3	blend composed of 100 part HNBR and 33.3 part FKM
HNBR-FKM 100-100	blend composed of 100 part HNBR and 100 part FKM
HNBR-FKM_MWCNT	blend composed of HNBR and FKM with 10 phr MWCNT
HNBR-FKM 100-33.3 MWCNT	blend composed of 100 part HNBR and 33.3 part FKM with 10 phr MWCNT
HNBR-FKM 100-100 MWCNT	blend composed of 100 part HNBR and 100 part FKM with 10 phr MWCNT
HNBR-(p)CBT	blend composed of HNBR and (p)CBT
HNBR-(p)CBT 100-0	blend composed of 100 part HNBR and 0 part (p)CBT
HNBR-(p)CBT 100-50	blend composed of 100 part HNBR and 50 part (p)CBT
HNBR-(p)CBT 100-100	blend composed of 100 part HNBR and 100 part (p)CBT

HNBR-(p)CBT 100-150	blend composed of 100 part HNBR and 150 part (p)CBT
HNBR-pCBT	blend composed of HNBR and pCBT
HNBR-pCBT 100-0	blend composed of 100 part HNBR and 0 part pCBT
HNBR-pCBT 100-50	blend composed of 100 part HNBR and 50 part pCBT
HNBR-pCBT 100-100	blend composed of 100 part HNBR and 100 part pCBT
HNBR-pCBT 100-150	blend composed of 100 part HNBR and 150 part pCBT
IPN	interpenetrating network
IR	isoprene rubber (polyisoprene)
MWCNT	multiwall carbon nanotube
NR	natural rubber
O	oxygen
Orbital-RBOP	orbital rolling ball-on-plate
Oscillating-RBOP	oscillating rolling ball-on-plate
PBT	polybutylene terephthalate
(p)CBT	partly polymerized cyclic butylene terephthalate
pCBT	fully polymerized cyclic butylene terephthalate
phr	part per hundred part rubber
R-O-O-R'	peroxide compound
RO·	free radical from a peroxide
SBS	styrene/butadiene/styrene rubber
SEM	scanning electron microscopy

semi-IPN	semi-interpenetrating network
Si	silicon
tc1	first time curve
tc2	second time curve
TDV	thermoplastic dynamic vulcanizates
TEM	transmission electron microscopy
TPEs	thermoplastic elastomers
TPO	thermoplastic olefin elastomers
TPO-O	TPO produced without dynamic curing
TPO-V	TPO produced with dynamic curing
unHNBR	uncured HNBR
unHNBR-(p)CBT	blend composed of unHNBR and (p)CBT
unHNBR-(p)CBT 100-50	blend composed of 100 part unHNBR and 50 part (p)CBT
unHNBR-(p)CBT 100-100	blend composed of 100 part unHNBR and 100 part (p)CBT
unHNBR-(p)CBT 100-150	blend composed of 100 part unHNBR and 150 part (p)CBT
unHNBR-(p)CBT 100-200	blend composed of 100 part unHNBR and 200 part (p)CBT
WAXS	wide-angle X-ray scattering
WLF	Williams-Landel-Ferry

Symbols

C_{01}	[MPa]	material constant for Mooney-Rivlin Material Model, second Mooney-Rivlin parameter
C_{10}	[MPa]	material constant for Mooney-Rivlin Material Model, first Mooney-Rivlin parameter
C_{11}	[MPa]	material constant for Mooney-Rivlin Material Model
C_{20}	[MPa]	material constant for Mooney-Rivlin Material Model
C_{30}	[MPa]	material constant for Mooney-Rivlin Material Model
COF		coefficient of friction
d_z	[mm]	fixed position in vertical direction
E	[MPa]	Young's modulus, elastic modulus of the spring
E_0	[MPa]	glassy modulus of the elastomer
e_i		i-th spring-dashpot constant
E_i	[MPa]	elastic modulus of the i-th spring
E_{pl}	[MPa]	plateau modulus (read from DMTA)
E_∞	[MPa]	plateau modulus of the elastomer over T_g
E'	[MPa]	storage modulus
E*	[MPa]	complex modulus
F	[N]	friction force/load
F_s	[N]	friction force just sufficient to resist the onset of relative motion or slip

F_k	[N]	friction force to resist relative motion after sliding is under way
G'	[MPa]	shear storage modulus
G''	[MPa]	shear loss modulus
G*	[MPa]	shear complex modulus
H	[MPa]	Martens hardness
I_1		first invariant of the elastic strain
I_2		second invariant of the elastic strain
L	[mm]	length, overall rolling distance
m_{air}	[g]	mass of the object in the air
M_c	[g/mol]	mean molecular mass between crosslinking
m_{liquid}	[g]	mass of the object in the liquid
N	[N]	normal force/load
r_1	[mm]	radius of the outer circle of the rotating guiding groove
r_2	[mm]	radius of the inner circle of the rotating guiding groove
R	[J/(K·mol)]	universal gas constant
R_a	[µm]	arithmetic roughness
T	[mm]	thickness
T	[°C]/[K]	temperature
T_g	[°C]	glass transition temperature
T_m	[°C]/[K]	melt temperature

t	[s]	time
tanδ		loss factor
t_i	[sec]	relaxation time constant of the i-th spring dashpot element
T_{ref}	[°C]	reference temperature
v	[mm/s]	velocity
V_1	[mm/s]	velocity of the outer circle of the rotating guiding groove
V_2	[mm/s]	velocity of the inner circle of the rotating guiding groove
$V_{2max\text{-}slide}$	[mm/s]	maximal value of the sliding speed
$V_{3max\text{-}slide}$	[mm/s]	maximal value of the sliding component
v_c	[mol/m^3]	apparent network density
v(t)	[mm/s]	velocity of the steel ball
ΔV	[mm^3]	volume loss
W	[MPa]	strain energy
W	[mm]	width
W_s	[mm^3/N·m]	specific wear rate

Greek symbols

δ	[°]	phase lag between stress and strain
η	[m^2/s]	viscosity of the dashpot
η_i	[m^2/s]	viscosity coefficient of the i-th dashpot

μ_s		static coefficient of friction
μ_k		dynamic/kinetic coefficient of friction
ω_1	[rad/s]	angular velocity of the guiding ring
ω_2	[rad/s]	angular forward rolling velocity of the steel ball
$\omega(t)$	[rad/s]	angular velocity of the sphere
ρ	[g/cm^3]	density
ρ_{object}	[g/cm^3]	density of the object
ρ_{liquid}	[g/cm^3]	density of the liquid
σ	[MPa]	stress
σ_0	[MPa]	initial stress
σ_D	[MPa]	stress of the dashpot
σ_M	[MPa]	Maxwell Model stress of Standard Linear Solid Model
σ_S	[MPa]	stress of the spring
σ_{S1}	[MPa]	stress of the first spring in standard Linear Solid Model
σ_{S2}	[MPa]	stress of the second spring in standard Linear Solid Model
σ_{Total}	[MPa]	total stress
τ	[sec]	relaxation time
ε		strain
ε_0		initial strain
ε_D		strain of the dashpot

ε_M	Maxwell Model strain of the Standard Linear Solid Model
ε_S	strain of the spring
ε_{S1}	strain of the first spring in the Standard Linear Solid Model
ε_{S2}	strain of the second spring in the Standard Linear Solid Model
ε_{Total}	total strain

1 Introduction

Rubber, having excellent elasticity combined with unique physical and chemical properties, is used to produce not only products for people's daily usage and medical need, but also rubbery equipments or parts supplied to mining, transport, construction, machinery, electronics and other industries. Rubber industry is one of the important basic industries for national economy. In the past three centuries, rubber was discovered, studied, developed and optimized by researchers and scientists and used and familiarized gradually by ordinary people.

The rubber stuff was obtained firstly from the sap of some plants by solidification and subsequent drying, which is classified as natural rubber (NR) nowadays (cf. Figure 1.1). Its name came from the Indian words "cahuchu" or "caoutchouc", meaning "weeping wood". The word "rubber" was given by English chemist J. Priestley (1733-1804) in 1770 after he observed that this material could erase the pencil marks on paper very well. However, this material was discovered by the French explorer, geographer, and mathematician C. M. de La Condamine (1701-1774) in around 1736 in his South America exploration. He also presented a paper to the Academy in 1751, written by French scientist F. Fresneau (1703-1770), which was regarded as the first scientific paper on rubber [1-4].

Figure 1.1 Rubber latex being collected from a tapped rubber tree [3].

But after American C. Goodyear (1800-1860) succeeded firstly in linking the natural rubber molecular chains by heating it together with sulphur in 1839, rubber became competent in practical usage. This process is called vulcanization and could greatly improve the durability and utility of rubber. In 1845, the vulcanized rubber was already applied as tyre material and in the 19th century 90's spread extensively for cars. As the number of cars increased dramatically, the need of natural rubber leaped [1-4].

In the First World War, for solving the lack of natural rubber resource, a team headed by F. Hofmann (1866-1956) succeeded in creating the first synthetic rubber, viz. polyisoprene in Germany in 1909 [4]. Subsequently, different kinds of synthetic rubbers were produced, e.g. rubber synthesized from butadiene, commercialized under the trade name Neoprene, and Buna rubbers, which were even copolymers (i.e. made up of two monomers) [4]. Neoprene is the polychloroprene, which had good properties and made people realize that man-made rubbery products can perform as well as natural rubber based ones. One Buna rubber, a copolymer of butadiene and styrene, became the basis of the synthetic rubber production for Germany, America and the Soviet Union during World War II [1-4].

With the deeper and deeper understanding of the microstructure of rubbery materials and the invention of new catalysts and polymerization methods, the rubber industry developed very fast. Many new products having higher resistance to temperature, various solvents (including oil) and new species, e.g. liquid, powder and thermoplastic rubbers appeared. Although the properties of synthesized rubber are not as comprehensive as natural one, the former has high elasticity, insulation, gas tightness, resistance to oil and high or low temperature. Therefore synthetic rubbers are applied widely in agriculture, military, traffic and daily life [1-4].

Rubber is used abundantly to produce tyres and rollers, and also in the field of power and motion transmission, where rolling friction and wear are key properties (cf. Figure 1.2). Some of them are working in severe conditions. For example, the aeroplanes' tyres experience extremely high stress friction during the moment of landing, which can cause much higher wear than in normal conditions. For the sake of long lifetime and safety, the requirements of the planes' tyres are very demanding, and of course, they are very expensive. Hence, it is necessary to study the rolling tribological

properties of the rubbery materials in order to increase the service life of rubbery parts. However, the related research is far below the needs, at least based on the information one can get from the open literature.

Figure 1.2 Castors, Drive Rolls and Rolls.

Therefore, in this work the rolling friction and wear properties of various rubbery materials (rubber matrices filled with different fillers and rubbery compounds) were studied in orbital rolling ball-on-plate test configuration (Orbital-RBOP) and oscillating rolling ball-on-plate test rig (Oscillating-RBOP) under dry condition. The wear mechanisms were inspected by scanning electron microscopy (SEM) and discussed. Differential scanning calorimetry (DSC), dynamic-mechanical thermal analysis (DMTA) and atomic force microscopy (AFM) and some other experimental methods were adopted to determine the phase structure and physico-mechanical properties of the rubber compounds.

Besides the experimental work, attention was paid to summarize the results by mathematical treatise. Note that rubber is characterized by high elastic and strong viscoelastic properties. The non linear elastic and linear viscoelastic properties can be calculated nowadays. For example, some existing simplified analytical methods can estimate well for example the friction resistance or internal heat generation in viscoelastic materials during rolling contact. However, they do not offer proper resolutions for more complex stress states or for the behaviour under repeated stresses [5]. With the progress in the computers' software and hardware, the finite element method (FEM) can be adopted to simulate the complex mechanical behaviours of rubbery materials accurately (e.g. [6-8]). Therefore, FE simulation was

done to the tests in Orbital-RBOP and Oscillating-RBOP rigs with representative rubbery materials. The results were compared with those of the experimental measurements.

2 Background

2.1 Elastomers and their special properties

2.1.1 Types

Elastomer is a kind of polymer, distinguished with its large elasticity from the other two types of polymers, namely from thermosets and thermoplastics. Elastomers can be divided into two categories: traditional thermoset and relatively novel thermoplastic types. This distinction is linked to characteristics of the crosslinking: chemical bonds (thermoset) or physical interactions (thermoplastic) are linking the molecular chains. Elastomer can also be called rubber, which is preferably used to refer to vulcanizates. Vulcanizates are obtained by a special curing process with the addition of sulphur or other curatives under high temperature. The related process is known as vulcanization. It is a chemical process in which polymer molecules link to each other and form a chemically cross-linked structure [9].

Elastomer can be formed from a single monomer (homopolymer), or two or more monomers (copolymer). It can also be composed of different elastomers (elastomer/elastomer blend); or may represent a mixture of thermoset and thermoplastic components (thermoset/elastomer or thermoplastic/elastomer hybrids).

2.1.1.1 Elastomers

2.1.1.1.1 Traditional or thermoset

The molecule chains in a thermoset rubber are linked by covalent bonds between sulphur-carbon and carbon-carbon atoms and form a three-dimensional network structure. This network structure determines its properties (hardness, resistance to chemical attack, etc.), making it not dissolvable in solvents and not reprocessable via remelting. Due to this beneficial property combination thermoset rubbers are more widely used than thermoplastic ones.

Homopolymer and copolymer [9, 10]

When the chain backbone is from only one monomer, the related polymer is termed to homopolymer (cf. Figure 2.1 (1)). Various rubbery products belong to this type, e.g. natural rubber (NR), polybutadiene (BR), silicone rubber, fluoroelastomers.

Opposed to a homopolymer, a heteropolymer or copolymer is a polymer derived from two (or more) monomeric species.

Since a copolymer consists of at least two constitutional units (not structural units), it can be classified based on how these units are arranged along the chain (cf. Figure 2.1):

(1) Alternating copolymers, possessing regularly alternating monomer units (cf. Figure 2.1 (2)).

(2) Periodic copolymers, monomer units arranged in a repeating sequence (e.g. (A-B-A-B-B-A-A-A-A-B-B-B)$_n$).

(3) Random copolymers, monomer units in a random sequence (cf. Figure 2.1 (3)).

(4) Statistical copolymers, monomer units arranged according to a known statistical rule.

(5) Block copolymers in which two or more homopolymer subunits are linked by covalent bonds (cf. Figure 2.1 (4)). The linkage of the homopolymer subunits may require an intermediate non-repeating subunit, known as a junction block. Block copolymers with two or three distinct blocks are called diblock copolymers and triblock copolymers, respectively.

The copolymers here refer to those with rubbery characteristics.

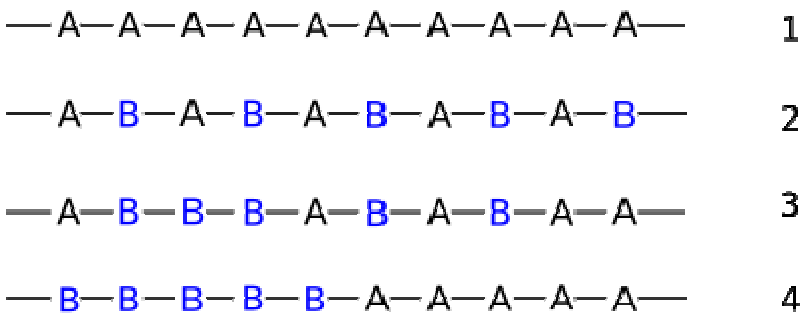

Figure 2.1 Types of polymers. (1) homopolymer, (2) alternating copolymer, (3) random copolymer, (4) block copolymer.

2.1.1.1.2 Thermoplastic [11, 12]

Thermoplastic elastomers (TPEs), sometimes referred to as thermoplastic rubbers, are a class of copolymers or a physical mix of polymers (usually a thermoplastic and a rubber) which consist of materials with both thermoplastic and elastomeric properties. The principal difference between thermoset elastomers and thermoplastic elastomers is the type of their crosslinking. In fact, crosslinking is a critical structural factor which contributes to impart high elasticity. The crosslinking of TPEs are formed physically through weak Van der Waals forces, dipole bond, hydrogen bond, crystalline thermoplastic hard domains [12] or just by the physical aggregation of parts of the molecules. Hence, unlike thermoset, TPEs dissolve in suitable solvents and they are recyclable, i.e. remelten and reused like thermoplastics [12].

Thermoplastic elastomers show advantages typical of both rubbery and plastic materials. TPEs are used where conventional elastomers cannot provide the range of physical properties needed in the product. For instance, butadiene-styrene block copolymers are used in shoe soles for their ease of processing.

TPE requires little or no compounding. The price of TPE is relatively high due to their synthesis and related raw materials. Cost reduction by adding low cost fillers, such as carbon black, is not straightforward. TPEs usually exhibit poor chemical and heat resistance, high compression set, low thermal stability and abrasion resistance.

Types

Commercially there are six generic classes of TPEs. They are styrenic block copolymers, polyolefin blends, elastomeric alloys (TPE-v or TPV), thermoplastic polyurethanes, thermoplastic copolyester and thermoplastic polyamides.

2.1.1.1.2.1 Block copolymers [10]

Thermoplastic block copolymers are derived from two (or more) monomeric species (thermoplastic and rubber-like, respectively) (cf. Figure 2.1 (4)). Physical crosslinks forms by "microphase separation" of the thermoplastic component in the rubbery one. The phase separated domains may be amorphous (as in the styrene-butadiene-styrene (SBS) block copolymer shown in Figure 2.2) or crystalline (in thermoplastic polyurethanes, copolyesters and polyamides). Above the glass transition temperature

(T_g) of amorphous and crystal melting point of semicrystalline types, respectively, the related materials are processable as thermoplastics. By subsequent cooling, phase segregation takes place again. This is the reason to call the related structure as thermoreversible physically crosslinked one.

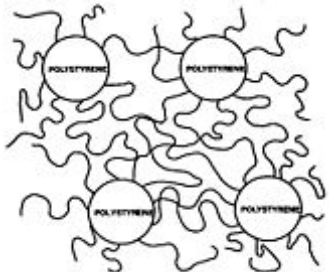

Figure 2.2 Schematic microstructure of a SBS block copolymer. Note: domains are composed of amorphous polystyrene. Their size can be tailored via synthesis upon request.

2.1.1.1.2.2 Dynamic vulcanizates [13]

Thermoplastic dynamic vulcanizates (TDV), also called elastomer alloy thermoplastic vulcanizates (EA TPV), belong to a novel family of thermoplastic rubbers. TDVs are produced by dynamic crosslinking (curing/vulcanization) of blends composed of thermoplastic resins and curable elastomers. The term “dynamic” or “in-situ” (cf. section 2.1.1.2.2) cross-linking means the selective curing of the thermoset rubber component and its fine dispersion in a molten thermoplastic resin occurs via an intensive mixing and kneading process. This process yields a fine dispersion of partially or fully cross-linked, micron-size rubber particles in a thermoplastic matrix. The main difference between TDVs and other thermoplastic elastomers produced from rubber/plastic blends is that the rubber component in the latter systems is not cross-linked. Therefore, a clear difference is made between thermoplastic olefin elastomers (TPO) produced without (TPO-O) and with dynamic curing (TPO-V).

2.1.1.2 Blends

Polymers can be blended with another polymer to produce polymer blends/hybrids, which can offer good compromise of properties, or even novel ones, not available in a single polymer. Blends may be homogeneous (components truly thermodynamically miscible) or heterogeneous (components thermodynamically immiscible but mechanically compatible) [12]. The term miscible describes that polymer blends have theoretical thermodynamic miscibility down to the segmental (molecular) level; the term compatible describes that polymer blends have useful practical properties, regardless of whether they are miscible or immiscible [14]. When two polymers are completely miscible down to molecular level, they form a single homogeneous phase, and properties are generally proportional to the ratio of the two polymers in the blend [14]. The heterogeneous blend is phase-separated, each phase is actually not pure (polymer A or polymer B), but rather a solution of B in A and a solution of A in B [14]. The rubber in polymer blends is usually crosslinked, and the blend itself shows elastomeric properties [12].

2.1.1.2.1 Phase morphology [12, 14]

The phase structure of blends is referred to as the morphology [14]. Thermodynamic functions and kinetic conditions determine the number of phases of a blend. The morphology of multiphase blends is controlled by the volume ratio, the solubility, and the viscosity of both components as well as the shape and packing density of the dispersed component [12].

The volume ratio of the two components limits the ability of the minor component to form a continuous phase in a multiphase system [12]. Generally the major phase will form the continuous matrix and control most properties, while the minor phase will form dispersed micro domains and contribute certain specialized properties to the blend. Dispersed domains usually have spherical shapes, which normally have the minimal surface energy. Generally, increasing attraction between the phases tends to decrease the size of the spheres and increase the technological compatibility. With increasing concentration of the minor phase, the dispersed domains may tend to become rodlike; and at fairly equal concentrations, the two phases may become lamellar. Another factor of the morphology is the shear flow during melt processing. This elongates spherical domains into platelike or fibrillar forms. Such nonspherical

morphology is generally accepted to have important effects on the practical properties [14]. If both components of a melt are able to form a continuous phase, then the molecules of the more polar component will associate and form the dispersed phase [12]. A further factor is the rheology: the less viscous phase tends to form the continuous matrix (even if it is present in rather small amount), while the more viscous one the dispersed domains [14]. A great variety of polymer blends can obviously be produced. Their properties depend on the number of phases, the mobility of the molecules in the various phases (T_g, crosslinking), and the phase structure itself (e.g. core-shell structures). The industry therefore uses very different polymer blends: rubber blends, homogeneous blends of thermoplastics, heterogeneous blends of compatible thermoplastics, rubber-modified thermoplastics, etc [12].

2.1.1.2.2 Production methods

Polymer blends can be produced by mixing two polymers (as melts, latices, or in solution), by in situ polymerization of a monomer in the presence of a dissolved polymer, by consecutive polymerization, etc. All processes have advantages and disadvantages with respect to the process, the properties of blends, and economics [12]. In situ polymerization involves solutions or gels of polymers P in monomers M, which are subsequently polymerized. Three processes can be distinguished. In process 1, a non-crosslinkable polymer P is dissolved in a non-crosslinkable monomer M that is subsequently polymerized. The industrially most important process 2 involves a graftable and crosslinkable rubber R in a monomer M that will be converted to a thermoplastic by polymerization. Process 3 utilizes an already crosslinked polymer X in a crosslinkable monomer M; this process results in interpenetrating networks [12].

2.1.1.2.3 Rubber blends [12]

Miscible mixtures of rubbers do not form separate phases; they become homogeneous elastomer blends on vulcanization. Homogeneity is present if domain structures cannot be resolved by the electron microscope. The existence of only one glass transition requires the cooperative movement of many chain segments and the related domain size is in the range of ≤ 50 nm.

Other rubber blends are heterogeneous in their uncrosslinked state. Such rubber blends show two glass temperatures, each of which is approximately identical with that of the parent rubber. Upon vulcanization, the rubber blends retain their phase structures and become heterogeneous elastomer blends. Such heterogeneous rubber blends may create problems, for example during vulcanization. The vulcanization agents (sulphur, accelerators, etc.) may become enriched in one of the phases that are then overvulcanized.

2.1.2 Dynamic mechanical properties

2.1.2.1 Glass transition

The glass transition is a phase transition in which amorphous polymers transform from a brittle, glassy amorphous status to rubbery, viscous amorphous status when heated, or reversely when cooled. For a semi-crystalline material the glass transition refers to what happens to the amorphous part of the material as the temperature changes. The transition temperature is named glass transition temperature (T_g), which strongly affects the properties of the polymers in their applications. In glassy state most of the bonds are intact, while above T_g non-covalent bonds between the polymer chains become weak. Hence polymers become soft and capable of plastic deformation without fracture above T_g. This is one aspect that makes many plastics useful [15].

T_g is dependent on the materials properties, e.g. degree of crosslinking, presence of additives. And as a thermodynamic parameter, it is influenced also by the measurement conditions (frequency of applied stress/strain, cooling ratio, etc), too. Accordingly, the T_g measured is just one point on the temperature scale if the change is imposed at one particular frequency [15].

T_g can be measured by dynamic mechanical thermal analysis (DMTA) and differential scanning calorimetry (DSC) (see section 4.2.1). Figure 2.3 shows a DMTA measurement of rubber for storage modulus (E') as a function of temperature (T). T_g is determined as the temperature when the stiffness of the rubber drops dramatically (cf. Figure 2.3). It can also be seen that when T_g has been reached, the stiffness stays stable for a while (around E'_2). This region where the E' keeps stable is called

the rubber plateau. Note that T_g can be defined from DMTA measurements by other ways, as well (peak of the loss factor or peak of the loss modulus).

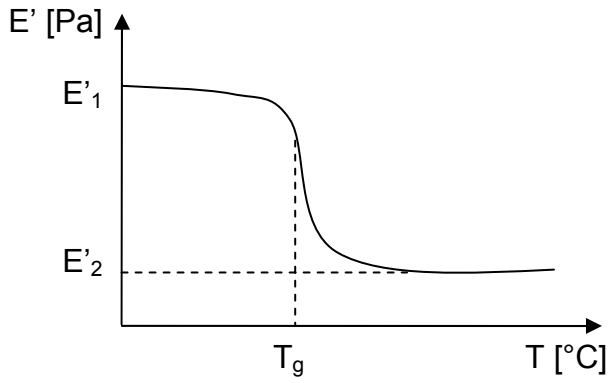

Figure 2.3 Storage modulus (stiffness) (E') versus temperature (T).

2.1.2.2 Complex modulus [16]

Dynamic modulus is the ratio of stress to strain under vibratory conditions (calculated from data obtained from either free or forced vibration tests performed in shear, compression, or elongation type loading). It is a property of viscoelastic materials.

2.1.2.2.1 Viscoelastic stress-strain phase-lag

Viscoelasticity is studied using the dynamic mechanical analysis where we apply small oscillatory strain and measure the resulted stress. In purely elastic materials the stress and strain occur in phase, so that the response of one occurs simultaneously with the other. In purely viscous materials, there is a phase difference between stress and strain, where strain lags by a 90 degree behind the stress. Viscoelastic materials exhibit behavior in between that of purely viscous and purely elastic materials, exhibiting some phase lag in strain.

Stress and strain in a viscoelastic material can be represented using the following expressions:
Strain:

$$\varepsilon = \varepsilon_0 \sin(t\omega) \tag{2.1}$$

Stress:

$$\sigma = \sigma_0 \sin(t\omega + \delta) \tag{2.2}$$

where ε_0 and σ_0 are initial strain and stress, respectively, ω is period of strain oscillation, t is time, δ is phase lag between stress and strain.

2.1.2.2.2 Storage and loss modulus

The storage and loss modulus in viscoelastic solids measure the stored energy, representing the elastic portion, and the energy dissipated as heat, representing the viscous portion, respectively. The tensile storage and loss moduli are as follows:
Storage modulus:

$$E' = \frac{\sigma_0}{\varepsilon_0} \cos\delta \tag{2.3}$$

Loss modulus:

$$E'' = \frac{\sigma_0}{\varepsilon_0} \sin\delta \tag{2.4}$$

$\tan\delta$ is termed as loss factor.

Similarly shear storage and loss modulus are defined as G' and G''.

Complex moduli E* and G* are given by:

$$E^* = E' + iE'' \tag{2.5}$$

$$G^* = G' + iG'' \tag{2.6}$$

where $i = \sqrt{-1}$.

2.1.2.3 Network-related properties

According to the rubber elasticity theory the inverse of the plateau modulus ($1/E_{pl}$) at a given temperature above T_g correlates with the mean molecular mass between crosslinking (M_c):

$$M_c = \frac{3\rho RT}{E_{pl}} \tag{2.7}$$

where E_{pl} is the modulus at an absolute temperature above T_g, ρ is the density, R is the universal gas constant (8.314 J/(K·mol)), and T is the absolute temperature. E_{pl}

is usually read at a temperature T_g + 40-50 K. From this reason we have determined E_{pl} at room temperature, i.e. T = 298 K.

It is more straightforward to consider the apparent network density (v_c) given by:

$$v_c = \frac{\rho}{M_c} \tag{2.8}$$

Mechanical properties of an elastomer depend strongly on network density. Modulus and hardness increase monotonically with increasing network density, and the material becomes more elastic (or stated alternatively, less hysteretic). Fracture properties, such as tear and tensile strength, pass through a maximum as crosslinking is increased [17].

Both M_c and v_c are apparent values. “Apparent” means that not only chemical crosslinking but also rubber-filler, filler-filler, and also other types of interaction (e.g. interpenetrating network (IPN) interaction, if exists), are involved in these terms.

2.1.3 Viscoelastic properties

Viscoelastic materials have the following properties: hysteresis, stress relaxation and creep.

2.1.3.1 Hysteresis

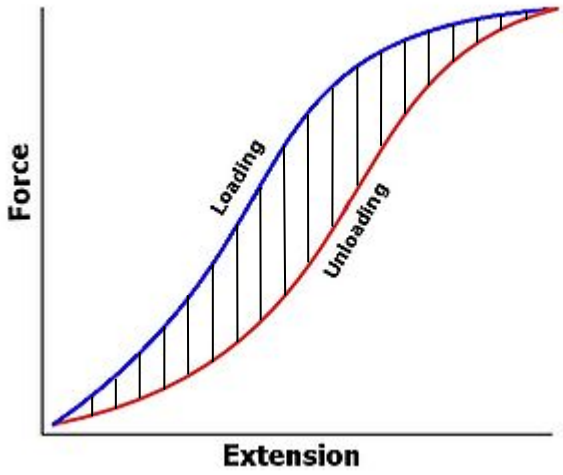

Figure 2.4 Elastic hysteresis of an idealized rubber band. Note: the shadowed area represents the hysteresis [18].

The hysteresis phenomenon means that a lag occurs between the application and the removal of the force in respect to the resulting response (see also 2.1.2.2.1). A system with hysteresis is path-dependent. A typical force-extension relationship of a rubber band is shown in Figure 2.4. The area in the centre of the hysteresis loop is the energy dissipated as heat.

2.1.3.2 Stress relaxation

Stress relaxation describes a phenomenon of viscoelastic materials whereby the stress inside the materials decreases with the time as a result of the increasing viscous and the decreasing elastic strain component, when the total strain is kept constant.

2.1.3.3 Creep

Creep is the phenomenon of increasing strain as a result of long term exposure to constant stress which is below the yield strength of the materials. Because of the viscoelasticity, both stress relaxation and creep of polymers behave in a nonlinear way.

2.2 Elastomers and their formulation

2.2.1 Elastomers

2.2.1.1 EPDM

Ethylene/propylene/diene (EPDM) rubber, a copolymer composed of ethylene, propylene and diene, has a wide range of applications, such as seals, belts, electrical insulators, automotive parts, tubes, wire-and-cable covers. It exhibits satisfactory resistance to polar solvents, such as ketones and alcohols. EPDM shows outstanding heat, ozone and weather resistance but attacked by most oils, gasoline, kerosene, aromatic and aliphatic hydrocarbons, halogenated solvents, and concentrated acids [19]. EPDM can be compounded with different kinds of fillers or blended with other polymers to enhance its performance. It also shows good tribological properties under sliding conditions [20-25].

2.2.1.2 HNBR

Hydrogenated acrylonitrile/butadiene rubber (HNBR) was firstly produced in 1984 in Germany. It has excellent resistance to oil, wear, aging, ozone, chemical attack and acceptable dynamic properties at low and high temperatures. These characteristics qualify it to be used in extreme automotive and oilfield applications. For instance, more than 50 % automotive transmission belts are produced from HNBR. Moreover, its properties can be tailored by blending with other rubbers, thermoplastics or incorporating fillers (e.g. Ref. 26-28). The known fillers for rubbers, e.g. carbon-type (carbon black, carbon fiber and carbon nanotube), silica-type (layered silicate and silica), zinc dimethacrylate, etc., are all capable of reinforcing the HNBR (e.g. Ref. 29-33).

2.2.2 Blends

2.2.2.1 Elastomer/elastomer

2.2.2.1.1 HNBR/FKM

FKM is the abbreviation of a fluororubber which is of the polymethylene type that contains vinylidene fluoride as a comonomer and have further fluoro, alkyl, perfluoroalkyl or perfluoroalkoxy groups in the polymer chain, with or without a curesite monomer [34]. It is the right selection when superior heat and chemical resistances are needed [35]. Blending of HNBR and FKM can be practiced as their peroxide curing recipe is very similar. Hirano et al. [36] achieved better low temperature characteristics than the parent materials with this combination. Moreover, blending HNBR with FKM may be an interesting strategy to influence the adhesion component related to friction and wear. Similar to polytetrafluoroethylene, FKM is expected to reduce the friction and enhance the resistance to wear owing to its high fluorine content when blended with cocurable rubbers.

2.2.2.2 Elastomer/thermoplastic

2.2.2.2.1 HNBR/CBT

Rubber/thermoplastic combinations offer various benefits, e.g. cost efficiency (thermoplastics are normally cheaper than rubbers), property improvements (e.g.

chemical and thermal resistance, tailored friction and wear properties), easy recycling (e.g. via remelting). A very promising new option is to combine rubbers with cyclic butylene terephthalate oligomers (CBT).

Cyclic butylene terephthalate (CBT) oligomers can be polymerized above its melting (T≈ 140-150 °C) into polybutylene terephthalate (pCBT). This temperature range is closely matched with that of rubber curing. Moreover, the polymerization temperature and time of CBT can be adjusted to the requirements by selecting suitable catalysts [37, 38]. The designation pCBT considers that its properties (molecular mass, crystallinity, ductility) somewhat differ from those polybutylene terephthalates (PBT) which have been produced in traditional polycondensation processes. A peculiar feature of the CBT polymerization is that it can be performed below the melting temperature of the resulting pCBT (T≈ 220 °C). In that case the pCBT crystallizes from an undercooled melt, again in a peculiar manner, which is still a topic of intensive dispute [39-41].

CBT can work as active filler in cured rubbers when partly or fully polymerized (designated further on by (p)CBT and pCBT, respectively). It was reported that the stiffness and strength of the related hybrids are highly enhanced compared to the parent rubber [27, 42]. In addition, the CBT acts as viscosity reducer for the parent rubber mixes. Preliminary results on the tribological properties of such hybrids were also very encouraging [27].

2.2.3 Reinforcements, fillers

Polymers are rarely used alone, without fillers, additives, different modifiers. For the practical aims (e.g. lower the cost, enhance the performance) different additives are mixed with polymers [12].

The mixing of polymer with additives and modifiers is termed to compounding. It can be performed by adding additives one by one, by using additive systems, or by employing master batches. Additive systems are carefully adjusted mixtures of additives that are formulated to avoid mutually antagonistic effects. Master batches are concentrates of additives in polymers; they facilitate the dosage of small amounts of additives. Powdery and liquid adjuvants can be admixed with polymer powders or liquids by paddle mixers, ball mills, turbo mixers, and similar devices; the mixing

requires energies of 35-100 kJ/kg. Much higher energies are required for the working-in of particulate adjuvants into thermoplastics (ca. 700 kJ/kg) and rubbers (ca. 1300 kJ/kg). Heavy machinery such as kneaders, double-screw extruders, Banbury mixers, and roll mills are required here [12]. The properties of compounds depend strongly on the conditions of the compounding process therefore it is often carried out by specialized companies (compounders). For example, only heterogeneous compounds result when poly(vinyl chloride) is mixed with additives in regular mixers. The related compounds (premix) cannot be processed directly to final products. High-performance mixers deliver free-flowing powders; and these dry blends can be extruded and injection molded accordingly [12].

Fillers

Fillers are added in order to improve mainly the economics of the more costly polymers (inactive fillers or extenders) or certain mechanical properties (active fillers or reinforcing agents). The length/diameter ratio (the so called aspect ratio or axial ratio) of the latter is larger than 1 [12]. Fillers have large surface area to interact with the rubber and to close particle-to-particle spacing in the compound [17]. The chemical structure of the fillers is not very important for their action although their chemical and physical surface structure might be of great importance. For good adhesion the surface of some fillers are treated specially. The proportion of fillers added varies widely from polymer to polymer. Industry standards are about 30 wt-% of fillers in thermoplastics and 60 wt-% in thermosets [12]. Fillers may increase the tensile strength and modulus of elasticity by reducing the flexibility of the molecule chains (restricting the number of conformational positions of chain segments near the filler surface), or increase the impact strength by adsorbing polymer chains on their surfaces to form physical bonds between fillers and polymers [12]. The selection of appropriate fillers is critical to the performance of elastomers.

Carbon black (CB), silica and multiwall carbon nanotube (MWCNT) are commonly used and/or promising additives for rubbers in wear resistant polymeric composites. Even though the above fillers are different in their chemical build-up and physical structure, their tribological functions can still be compared because all of them are “active”, i.e. reinforcing-type fillers for rubbers.

2.2.3.1 Traditional

CB and silica are very effective for reinforcing rubbers. They can be produced with a primary particle size as small as 10 nm. The corresponding surface area covers a few hundred m^2 per gram of filler [17].

2.2.3.1.1 CB

CB is “preformed” nanofiller, composed of amorphous carbon, which has a high specific surface. It is mainly used as pigment and reinforcement in various rubber and plastic products. The abrasion wear properties of CB filled rubber products are excellent. Carbon black is most effective for the reinforcement of non-crystallizing elastomers.

In the CB the primary particles are aggregated which form the so-called agglomerates. To provide the highest reinforcement, these CB agglomerates must be broken down into aggregates and thoroughly dispersed in the rubber. This requires mixing at high shear stress. During shear mixing, rubber and CB become partly chemically linked. The interactions between rubber and CB include a spectrum of strengths, with some chains chemically attached to the CB while others possess physical bonds of varying magnitude [17].

2.2.3.1.2 Silica

The CB reinforced products are black. When there is a special demand for colored products, “preformed” silica (SiO_2) is often adopted to replace CB. By increasing the interaction between rubber matrices and silica, using different silanes, rubber compounds with very good abrasion resistance can be produced (e.g. [43]).

2.2.3.2 Novel

2.2.3.2.1 MWCNT

Carbon nanotube (CNT), discovered by Iijima in 1991 [44], is considered as a very promising reinforcement for different polymers. This is due to the high stiffness, strength and high aspect ratio of the CNTs even in case of their multiwall variants (viz. MWCNT). The CNT-containing polymer composites have outstanding

mechanical performance, strongly improved electric and thermal conductivities if the nanotubes are well dispersed (exfoliated) and well adhered to the matrix [45]. Research works already addressed the potential use of MWCNT for wear resistant polymeric systems [46-53].

2.2.3.2.2 CBT

As mentioned above (cf. section 2.2.2.2.1), CBT can work as active filler in cured rubbers in both partly or fully polymerized states. It can enhance the stiffness, strength and tribological properties of the related hybrids compared to the parent rubber [27, 42], and also it contributes to the reduction of viscosity of the parent rubber mixes.

2.2.4 Vulcanization additives

Usually, the actual chemical cross-linking (vulcanization) is done with sulphur, but there are other technologies, including peroxide-based systems. The combined cure package in a typical rubber compound comprises the cure agent itself (sulphur or peroxide), together with accelerators, activators, like zinc oxide and stearic acid, and further rubber additives [54].

Four types of curing systems are in common use. They are [54]:
1) Sulphur systems,
2) Peroxides,
3) Urethane crosslinkers,
4) Metallic oxides.

They are used to vulcanize different types of elastomers. At present, the most widely used vulcanizing agent is sulphur [17].

2.2.4.1 Sulphur [17]

For sulphur crosslinking the elastomer must contain double bonds with allylic hydrogens. General purpose diene elastomers, such as ethylene/propylene/diene (EPDM) rubber, NR and isoprene rubber (IR) meet this basic requirement.

Crosslinking with sulphur alone is quite inefficient and requires curing times of several hours. To increase the rate and efficiency of sulphur crosslinking, accelerators are normally added. These are organic bases and can be divided into five major categories: guanidines, thiazoles, dithiocarbamates, xanthates, and thiurams. Accelerated sulphur curing is more efficient when activators, zinc oxide and stearic acid, are added. It is thought that these additives combine to create soluble zinc ions that activate intermediate reactions (complex formation) involved in the crosslinking reactions.

2.2.4.2 Peroxide [17, 55]

Peroxides are another type of curing agent for elastomers. Unlike sulphur vulcanization, carbon-carbon double bonds are not required for peroxide curing and thus, peroxides may be used to crosslink saturated elastomers, e.g. ethylene-propylene copolymers, chlorinated polyethylene, chlorosulfonated polyethylene, HNBR, and silicone rubber. In addition, peroxides readily crosslink diene elastomers. Peroxide is a compound containing a specific functional group or a molecule containing an oxygen-oxygen single bond (R-O-O-R'). It tends to decompose easily to free radicals of the form RO·. Peroxide curing takes place via this free-radical and leads to carbon-carbon crosslinks, which are quite stable. The crosslinked materials show good aging resistance and low compression set.

2.2.5 Other additives

Rubber mixes may contain other additives listed below [17]:

1) Extenders: are added to rubber compositions to reduce cost. Oil extension of rubber, especially in tire treads, is widely practiced. Other types of extenders are particulate solids with primary particle sizes greater than about 1 μm. These stiffen rubber compositions, but either have little effect on strength or diminish it. Examples include clay, calcium carbonate and ground coal.

2) Anti-oxidants: oxygen and ozone can react with elastomers and alter the network structure by causing chain scission and/or crosslinking. Antioxidants and antiozonants, which can function chemically or physically, have been developed to

inhibit the action of these reactive components of air. The most common types of chemical protectants are aromatic amines, phenolics, and phosphites.

3) Processing aids: additives that lower viscosity and thus enable a rubber compound to be fabricated with less energy. They also increase the melt stability so that the rate of processing can be increased. There are two general kinds of process aids: chemical peptizers and physical plasticizers.

4) Tackifiers: a class of resins added to elastomers to improve tack, which is the ability of two materials to resist separation after being in contact for a short time under light pressure. They must be compatible with the related rubbers.

2.3 Friction and wear of elastomeric materials

2.3.1 Friction

Friction is the resistance against the relative movement of two bodies contacting each other. It depends in a complex, and not yet clear way, on both the surface roughness and the mechanical properties of the specimen [12]. The three basic parameters are friction force (F), normal force (N) and coefficient of friction (COF), which are measures of the friction.

Friction force (F) is the resisting force tangential to the interface between two bodies when, under the action of an external force, one body moves or tends to move relative to the other. Normal force (N) is the component, perpendicular to the surface of contact, exerted by one object in the friction pair, on the other object. The COF is defined as:

$$\mu = F/N \tag{2.9}$$

$$\mu_s = F_s/N \tag{2.10}$$

$$\mu_k = F_k/N \tag{2.11}$$

where μ_s is static COF, F_s is the friction force just sufficient to resist the onset of relative motion or slip, μ_k is dynamic/kinetic COF, F_k is the friction force to resist relative motion after sliding is under way [56]. When relative motion starts, the friction between the two surfaces converts from static to kinetic type.

2.3.1.1 Classification

There are different classifying ways of friction and thus, accordingly various friction types. The common classifications are [57]

1) according to the motion of the contacting pair:
Sliding friction: between two relatively sliding objects,
Rolling friction: between two objects at least one of which makes rolling motion to the other.
2) according to the moving status of the contacting pair:
Static friction: between two contacting areas having only relative moving tendency,
Dynamic/kinetic friction: between two relatively moving objects.
3) whether friction happens to a single object:
Internal friction: within internal parts of one object. Internal friction is the force resisting motion between the elements making up a solid material while it undergoes deformation [58],
Outer friction: between two objects.
4) if lubrication exists:
Dry friction: when there is no lubricant in contacting area,
Lubricated (fluid) friction: between two solid surfaces separated by gas or liquid,
Mixed friction: combination of the above types.

2.3.1.2 Friction history [59, 60]

The history of friction is very long, which can date back to 2000 years ago, when Aristotle (384-322BC) mentioned that concept. But the quantitative research started from the 15th century. The whole development history can be divided into four periods:

(1) L. da Vinci (1452-1519) introduced for the first time the concept of the COF as the ratio of the friction force to the normal force. His conclusion was that the friction force equaled one fourth of its weight. His summary obtained from the experiments with hard wood or iron-hard wood group. He also thought that lubricant or other similar medium decreased the friction between the friction pairs.

(2) French scientific instrument inventor and physicist, one of the pioneers in tribology G. Amontons (1663-1705), proposed his theory, the well known Amontons' law: the largest static friction force in the contact area is proportional to the normal force. It is relative to the properties and status of the contact surfaces, but independent of the area and shape of the contacting surface. The sliding friction force is proportional to the normal force, independent of the contacting area.

(3) in the 18th century, the very famous French physicist C.-A. de Coulomb (1736-1806) summarized the experiments and theories of Da Vinci and Amontons and after lots of his own experiments, he submitted his theory (Coulomb's law):
1st law: The force of friction is directly proportional to the applied load. The force of friction is independent of the apparent area of contact.
2nd law: Kinetic friction is independent of the sliding velocity.
3rd law: the largest static friction force is larger than the sliding friction force.

In fact the 1st law is the Amontons' law, i.e. static friction law and sliding friction law. The second law is actually not correct as a common law from the viewpoint of the current opinion. The relation between the kinetic COF and sliding velocity is quite complex. Coulomb regarded that COF is an empirical value: it has to be measured experimentally, but can not be found through calculations. COF depends on system variables like temperature, velocity, atmosphere and also what are now popularly described as aging time; as well as on geometric properties of the interface between the materials.

(4) in the 19th century, the friction research addressed the lubrications due to the machines with moving parts which were developed during the industrial revolution. But no friction mechanisms were newly submitted.

Friction mechanisms [59]

Da Vinci, Amontons and Coulomb believed the friction originated from the resistance due to mutual pressing and shearing existing in the tiny bumps and craters of the two relatively moving contacting surfaces. It fits for the friction of wood, etc. However, this explanation can not account for why the smoother the surface is, the larger the friction is. Hence another mechanism emerged.

Firstly suggested by J. T. Desaguliers (1683-1744) [61], then approved and developed by S. Vince (1749-1821), F. P. Bowden (1903-1968) and D. Tabor (1913-2005) [62], the nature of friction was attributed to cohesion and adhesion. This is useful for explaining e.g. why two closely contacting metallic parts have very large friction force.

Besides the two explanations above, there are some others, for example, the theory considering the combination of interlocking and adhesion, the combination theory of interlocking, adhesion and plastic deformation.

Friction is very complex; there is no general theory to clarify all friction phenomena. The above explanations have their own application conditions. As concluded by Suh and Sin, asperity deformation, ploughing by wear particles and hard surface asperities and adhesion between the flat surfaces can all affect the value of COF [63]. The rubbing conditions determine the main active mechanisms [63].

2.3.1.3 Rolling friction of polymers

2.3.1.3.1 Rolling of a sphere on flat rubber

The early emphasis of friction research lied mostly in metallic materials, whose properties are quite different from those of rubbery materials. Therefore the obtained friction theories, e.g. Amontons' law, can not be applied to rubbers. Then the researchers began to notice the time-effect on the friction of rubbers. This aspect has been addressed by scientific works later on.

After the first treatise by Dupuit in 1842 [64], the pioneer work in the rolling friction for rubbery materials were done by D. Tabor, J. A. Greenwood, etc. in 1950s [65-71]. They all attributed rolling friction principally to mechanical hysteresis in the substrate as it is deformed and released by the passage of the rolling body [64]. When a spherical indenter is pressed into rubber a certain amount of elastic work is performed. As the indenter moves forward elastic work is done in deforming the rubber in front of the indenter whilst elastic work is recovered from the rear. If the rubber were ideally elastic the rubber behind the sphere would yield up an identical amount and no net energy would be lost. But in fact, a constant fraction of the input

elastic energy is lost as a result of elastic hysteresis in the rubber. In rolling this is the primary source of the frictional work [66].

2.3.1.3.2 Rolling in Orbital-RBOP rig [29]

In the Orbital-RBOP tribotest device (cf. Figure 2.5) the steel ball is driven by the revolving guiding groove (cf. Figure 2.6). At the contact points of the rotating (ω_1) grooved plate and the rolling ball different velocities evolve (V_1, V_2). This is because of the difference in the radii of the groove by keeping the ball in trace (r_1, r_2). The velocity difference V_1 - V_2 generates a spinning motion of the ball (ω_3) [cf. Figures 2.6 and 2.7(a)]. At the same time, the velocity difference between the upper side (contact with the edges of the rotating guiding groove) and the bottom side (contact with the fixed rubber specimen) of the ball induces a forward rolling (ω_2) [cf. Figures 2.6 and 2.7(b)]. Because of the additional spinning motion, a rotation sliding occurs at the contact ellipse where the sliding speed changes. The elliptical contact surface is due to the fact that the ball rolls in the wear track of the rubber. The maximal value of this sliding component is noted by $V_{3max\text{-}slide}$ [cf. Figure 2.7(a)]. During the forward rolling the ball ‘‘sticks’’ at the bottom point (pole point ‘‘P’’) of the ball. On the basis of the works of Heathcote [72] this sliding zone is complex in respect with the relative displacements. It contains zones both with forward and backward sliding motions [cf. Figure 2.7(b, c)]. If we assume a perfect sticking in the point ‘‘P,’’ the maximal value of this sliding speed [$V_{2max\text{-}slide}$ in Figure 2.7(c)] correlates with the indentation depth of the ball (i.e. depth of the wear groove).

On the basis of the geometry-related calculations and assumptions about the indentation $V_{2max\text{-}slide} \approx 0.33V_{3max\text{-}slide}$ was received. The superposition of the two different sliding fields [Figure 2.7(a, c)] tells the local sliding directions and estimated relative velocities in the contact area (cf. Figure 2.8). Consequently, at the outer side of the contact area the relative sliding speed of the ball against the rubber is larger than at the inner side of the track. The direction of the sliding in the outer side is forward whereas at the inner side it is backward. Therefore the scanning area for SEM inspection were chosen from the outer, centre and inner region, respectively (cf. Figure 2.5).

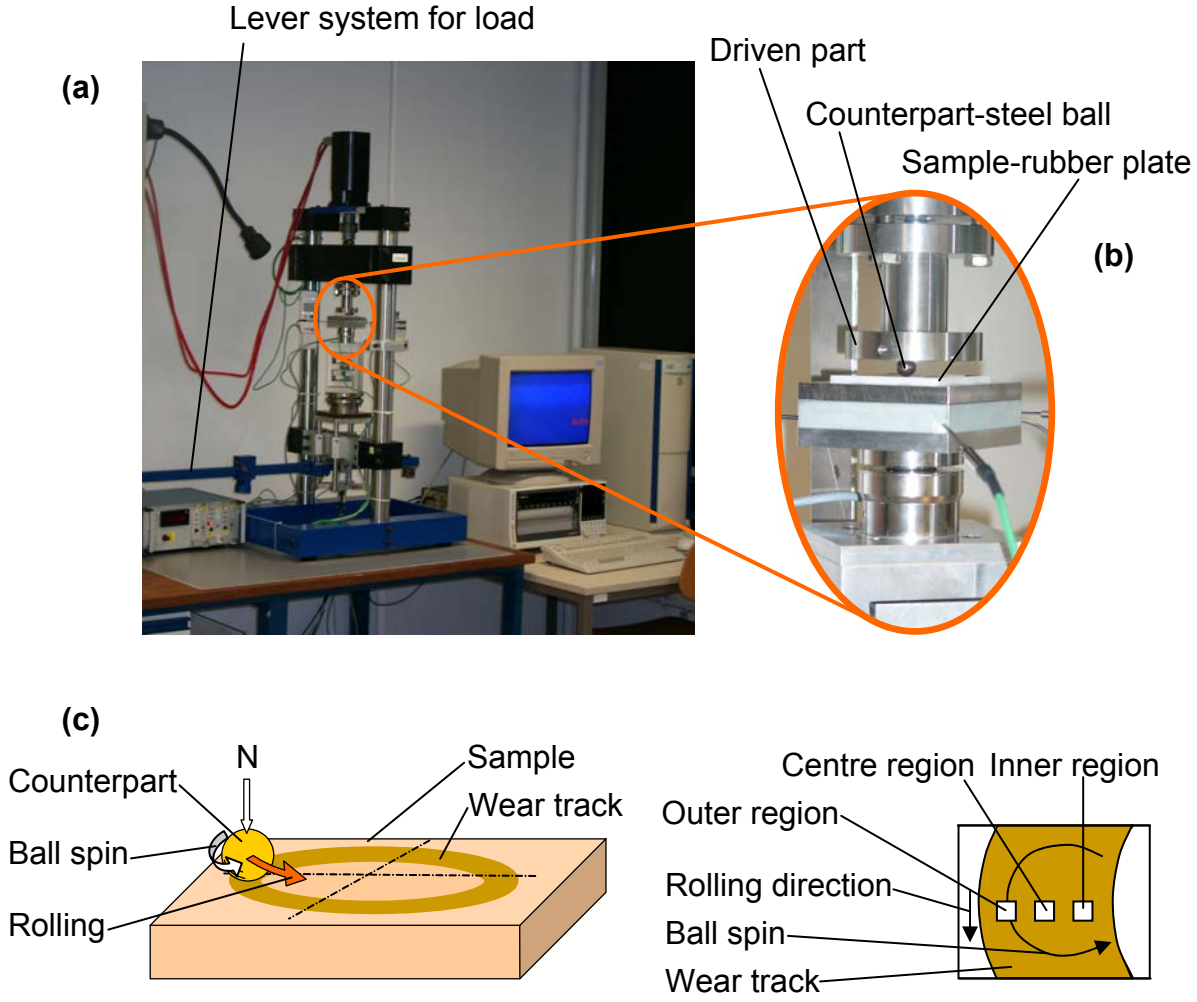

Figure 2.5 Overview of the Orbital-RBOP machine (a) and detailed view of steel ball acting on a flat specimen (b). Scheme of the test configuration of Orbital-RBOP (c). (c) also shows the preparation of the samples for SEM investigations after Orbital-RBOP test.

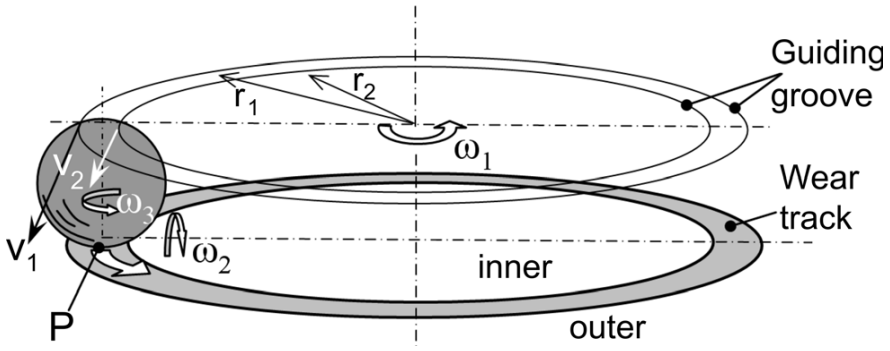

Figure 2.6 Kinematics of the rolling ball in the RBOP device.

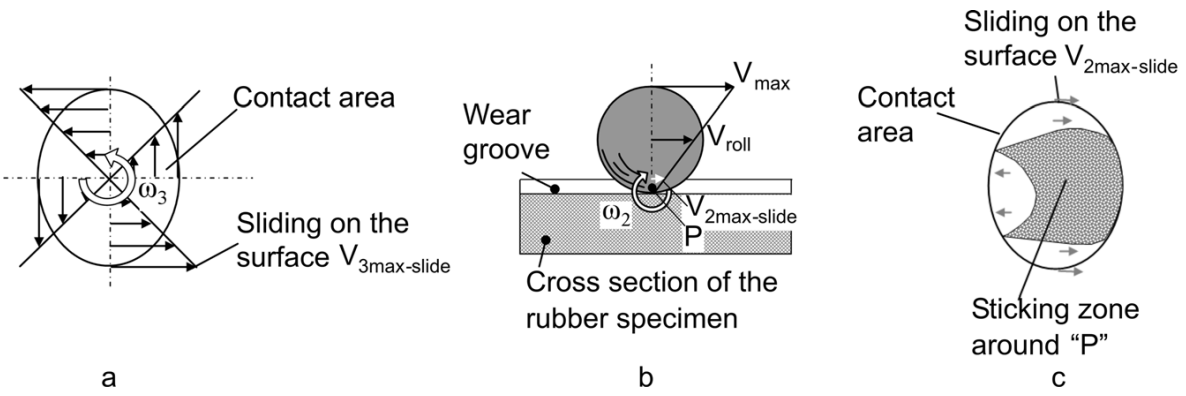

Figure 2.7 Sliding directions at the elliptic contact area of the steel ball and the rubber specimen caused by the spinning-ω_3 (a) and rolling motions-ω_2, (b), a schematic sketch of the forward rolling of the ball in the groove is given in picture (c) shows the contact surface at forward rolling.

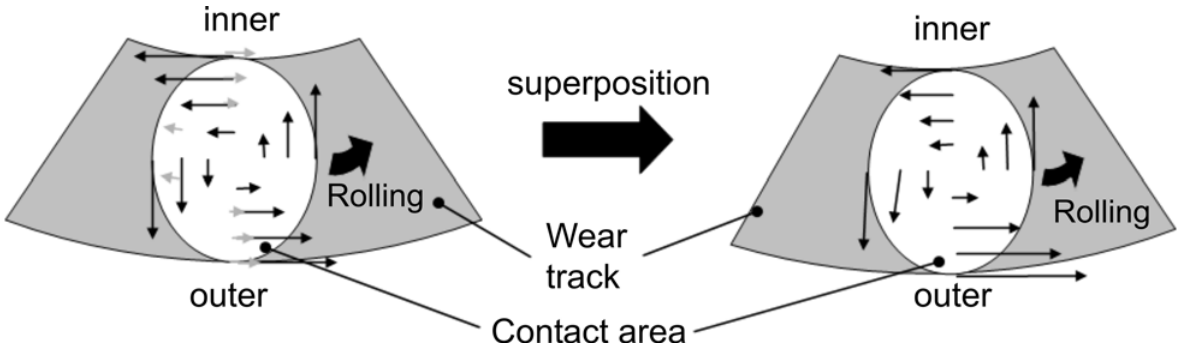

Figure 2.8 Superposition of the sliding velocities in the contact area during orbital rolling.

2.3.1.3.3 Rolling in Oscillating-RBOP rig

The pressure distribution over the contact area in Oscillating-RBOP tests (cf. Figure 2.9) can be estimated with the Hertzian theory (cf. Equation in Figure 2.10) [73]. Accordingly, the wear track is divided into three regions-two side and one centre regions-for the convenience of wear mechanisms' assessment (cf. Figure 2.10).

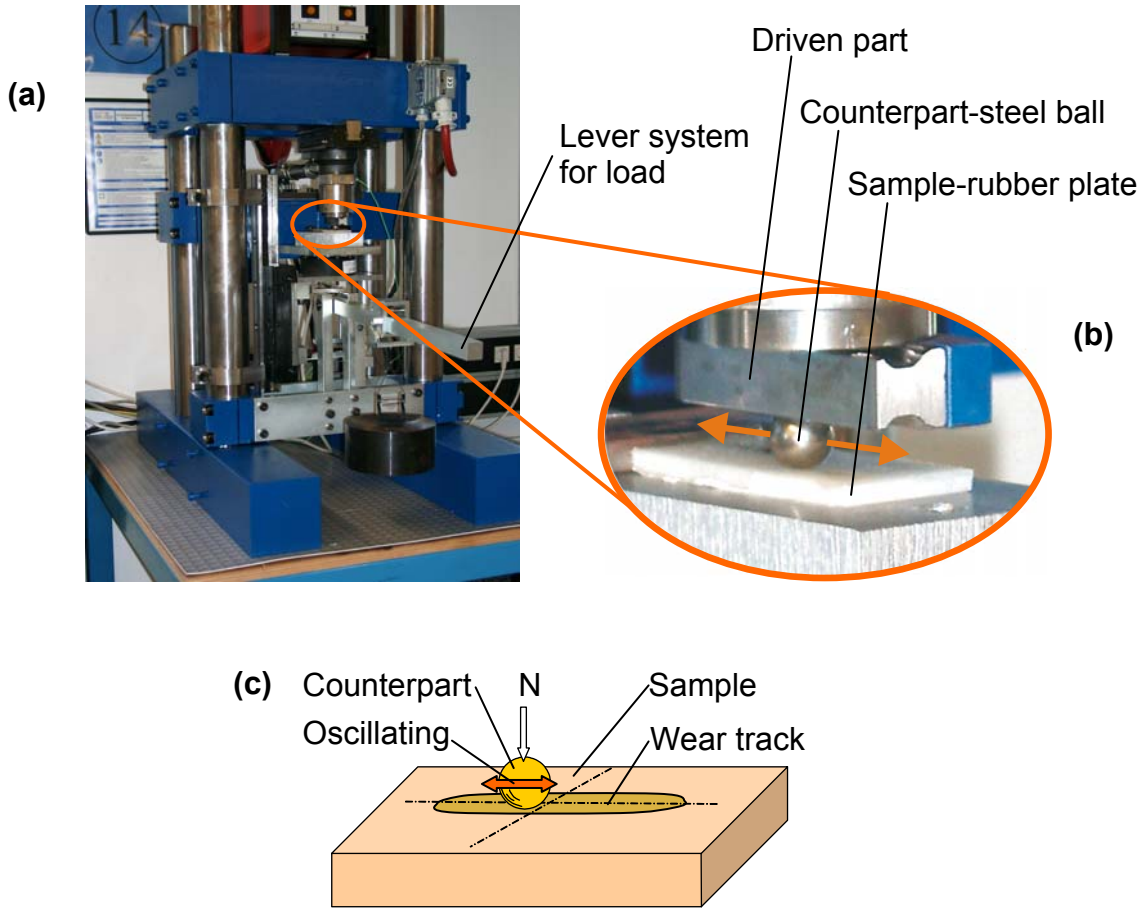

Figure 2.9 Overview of the Oscillating-RBOP machine (a) and detailed view of steel ball acting on a flat specimen (b). Scheme of the test configuration of Oscillating-RBOP (c).

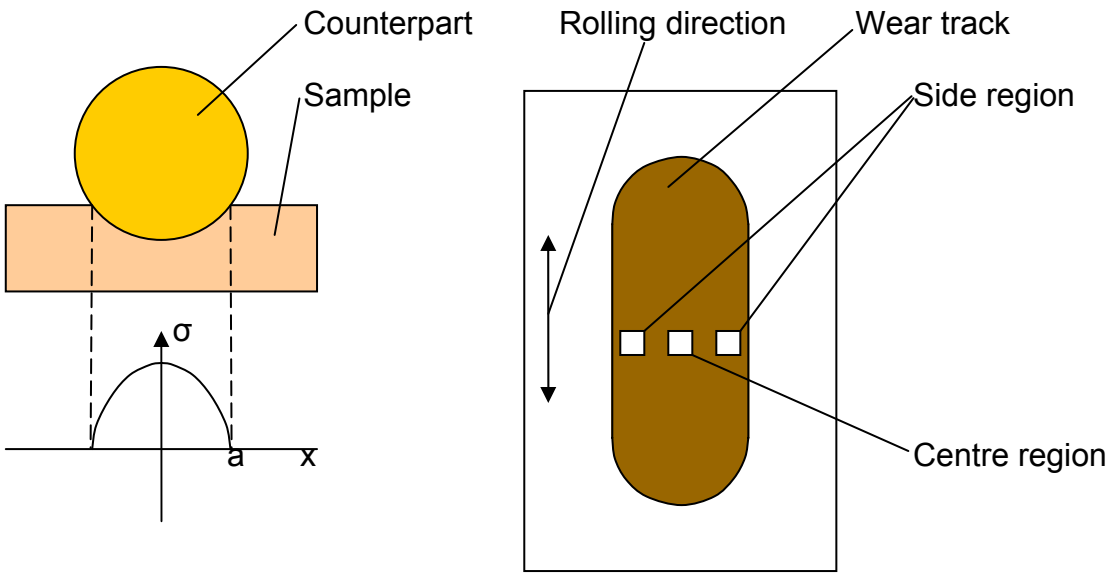

$$\sigma = \frac{3N}{2\pi \cdot a^2}(1-\frac{x^2}{a^2})^{1/2}$$

Figure 2.10 Hertzian theory (equation) and Hertzian pressure distribution over the contact area (left) and three regions designated for Oscillating-RBOP for SEM investigation (right).

2.3.2 Wear

Wear is the progressive loss of substance from the operating surface of a body occurring as a result of relative motion at the surface [63]. It is influenced by many factors, which can be divided into two types: properties of the friction pair and operating conditions (working environment). The former include mechanical, chemical, thermal properties, topography of the pair, etc. Aspects of the working environment include load, speed, temperature, lubrication, contacting way (rolling, sliding, impact, etc.), etc.

The wear degree can be assessed by specific wear rate (W_s):

$$W_s = \frac{\Delta V}{NL} \tag{2.12}$$

where $\Delta V\left[mm^3\right]$ is the volume loss, $N[N]$ is the normal load, $L[m]$ is the overall rolling distance.

Note that the volume loss is more relevant than the mass loss when evaluating the wear property of the materials. This is because the service life of an engineering component is often linked with a maximal allowed dimensional change (when dimensional losses exceed the specified tolerance limits). Besides, the volume loss gives a truer picture than the mass loss when comparing the wear resistance of materials with large differences in their densities.

There are various wear mechanisms. One classifying way for wear mechanisms was given by Burwell in the 1950s, who divided wear into abrasion, adhesion, surface fatigue and tribochemical processes [74]. Suh thought that the wear mechanisms depend on the materials, the environmental and operating conditions and the geometry of the wearing bodies [75]. These wear mechanisms may be classified into two groups: those primarily dominated by the mechanical behaviour of solids and

those primarily dominated by the chemical behaviour of materials. What determine the dominant wear behavior are mechanical properties, chemical stability of materials, temperature and operating conditions [75]. However, Tabor divided wear into three groups: 1) arises primarily from adhesion between the sliding surfaces, 2) derives primarily from non-adhesive processes, and 3) produced by interaction between the adhesive and non-adhesive processes. In addition, the frictional process itself can produce profound structural changes and modifications in the physical and chemical properties of the sliding surfaces. Consequently, unless a single wear process dominates, these surface changes and complex interactions must necessarily make wear predictions extremely difficult and elusive [76].

2.3.2.1 Wear mechanisms for elastomeric materials

(1) Schallamach waves [77]

Visual observations of contact areas between soft rubber sliders and hard tracks, and between hard sliders and soft rubber tracks (cf. Figure 2.11), show that relative motion between the two frictional members is often only due to “waves of detachment” crossing the contact area at high speed from front to rear (cf. Figure 2.12). This material loss pattern in the rubber surface is produced by buckling, which is attributed to tangential compressive stresses.

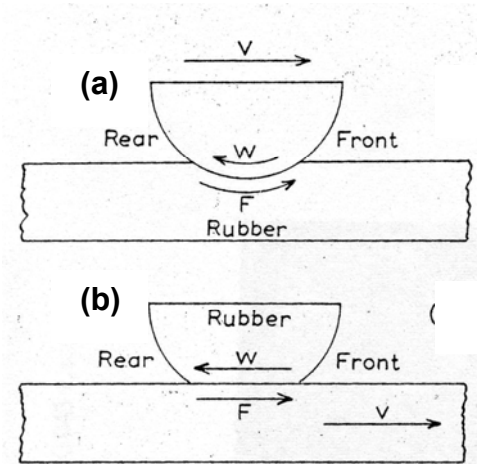

Figure 2.11 Sketches of the relative directions of sliding velocity, wave propagation and friction force F; (a) hard slider on rubber track, (b) rubber slider on hard track.

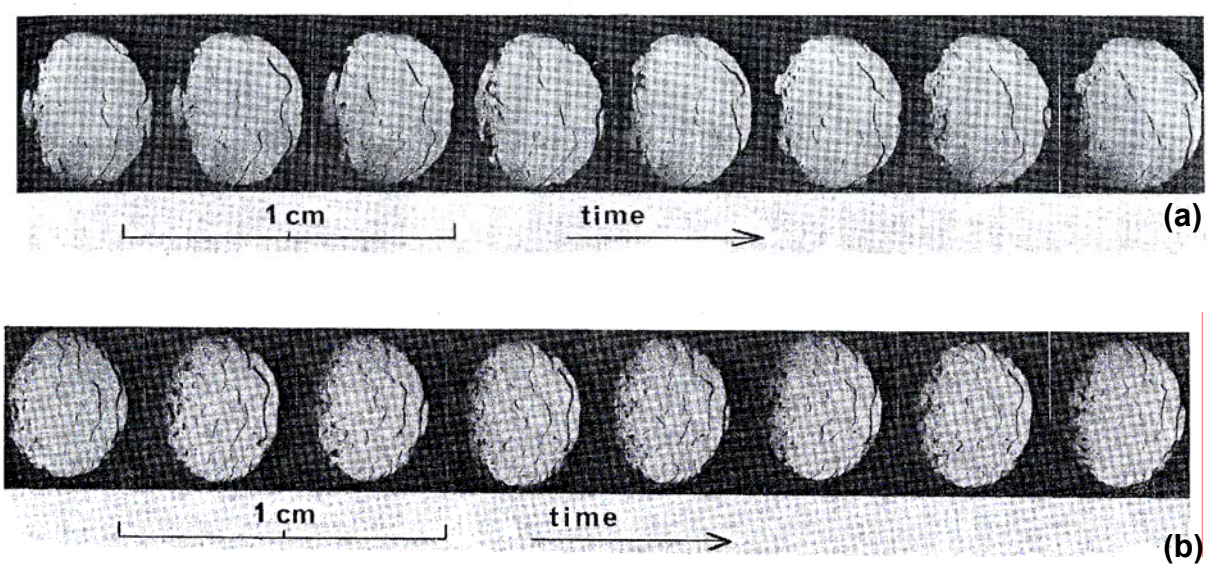

Figure 2.12 Eight frames at (1/32)s intervals of a film of the contact between (a) a transparent rubber track and a hard sphere, (b) a perspex plate and a natural rubber sphere.

(2) Abrasion [78-80]

Figure 2.13 Pattern abrasion of CB filled NR. Direction of abrasion: upward. Magn. 10.8 x.

Abrasion of rubber is due to mechanical failure under the tractive stresses produced frictionally by the asperities of the track. In this process, certain periodic structures are often created on the abraded rubber which have been called “abrasion pattern”.

Abrasion patterns are classified into intrinsic abrasion (occurring in the absence of patterns) and pattern abrasion (sets of parallel ridges at right angles to the direction of motion) (cf. Figure 2.13). The phenomenon of pattern abrasion has the important consequence that the relative abrasion rating of rubber compounds may depend pronouncedly on the conditions of the test.

(3) Surface fatigue and delamination wear mechanisms

Fatigue is the progressive and localized structural damage occurring when a material is subjected to repeated tribological loading (cf. Figure 2.14). This is mainly based on the action of stresses in or below the surfaces [63]. The maximum stress values develop often beneath the surface.

In studying the plastic-elastic stress fields in the sub-surface regions of sliding asperity contacts and the possible dislocation interaction, a “delamination theory of wear” has been proposed by Suh. According to him the generation of sheet-like wear particles is explained as follows (cf. Figure 2.14) [63]:

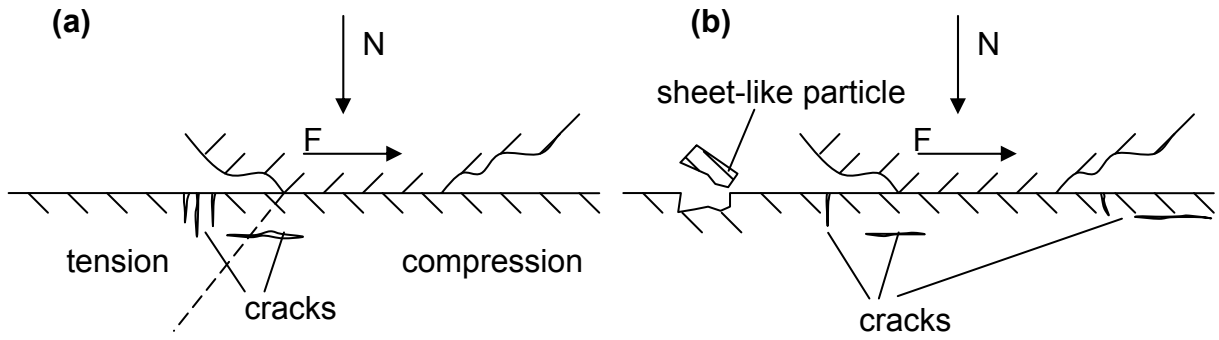

Figure 2.14 Characteristics of surface fatigue (a) and delamination (b) wear model.

Delamination wear model:

1) transmittance of stresses at contact points,

2) incremenal plastic deformation per cycle,

3) subsurface void and crack nucleation,

4) crack formation and propagation,
5) delamination of sheet-like wear particles.

(4) Wear by roll formation [73]

Roll formation is favored in a rubber of inherently low tear strength. It occurs under conditions of adhesion friction (cf. Figure 2.15).

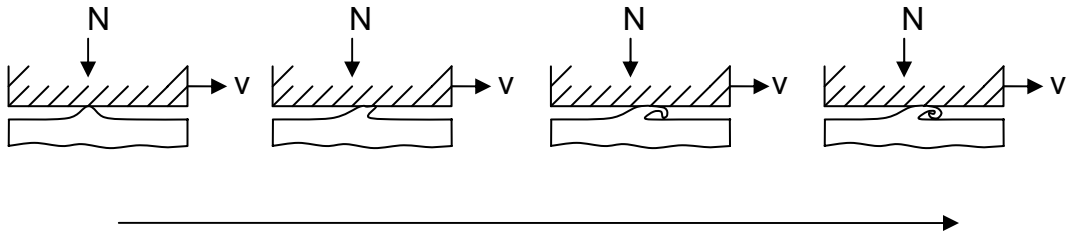

Figure 2.15 Wear by roll formation (v is velocity) [73].

(5) Adhesive wear

The adhesive wear processes are initiated by the interfacial adhesive junctions which form if solid materials are in contact on an atomic scale [63] (cf. Figure 2.16). Adhesive wear is also known as scoring, galling, or seizing. Surface asperities are plastically deformed, adhered together by the high pressure and break as the movement goes on.

Adhesive wear model [63]:
1) asperity contact deformation,
2) removal of surface films,
3) formation of adhesive junctions,
4) fracture of junctions and transfer of material,
5) modification of transferred fragments (e.g. strain energy storage, tribochemical effets),
6) removal of transferred/backtransferred fragments (e.g. by fatigure, fracture, abrasion).

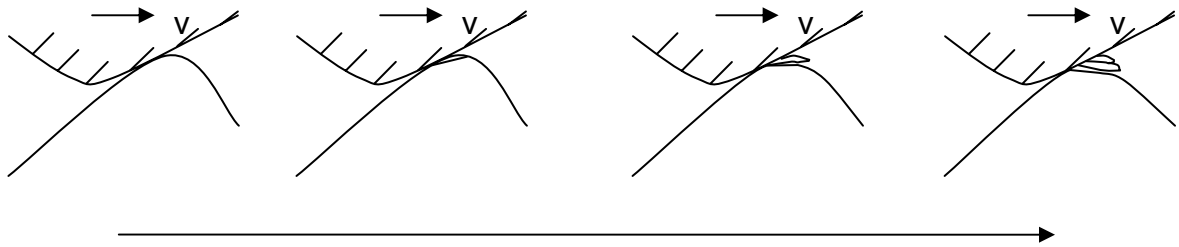

Figure 2.16 Adhesive wear [81].

2.4 Material models for elastomeric materials

2.4.1 Generalized Maxwell Model

As described before, rubbery materials possess time-independent elastic and time-dependent viscous properties demonstrating their viscoelastic behavior. The pure elastic and pure viscous response to deformations can be described by a spring and a dashpot, respectively. A spring is a Hookean body, responding instantaneously by $\sigma = E\varepsilon$ (σ is the stress, E is the elastic modulus of the material, and ε is the strain that occurs under the given stress). As a Newtonian liquid, a dashpot responses according to $\sigma = \eta \cdot d\varepsilon/dt$, where σ is the stress, η is the viscosity of the material, and $d\varepsilon/dt$ is the time derivative of strain [12].

To describe a material with linear viscoelastic properties-among others-the Maxwell, Voigt-Kelvin, Standard Linear Solid and generalized Maxwell Model can be adopted (cf. Figure 2.17). Linear viscoelastic is that process in which the stress, strain, and strain rate can be combined linearly. So, it is usually applicable only for small deformations. Nonlinear viscoelasticity refers to the function formed not in a linear way. It is usually happens at large deformations or when the materials' properties change under deformations [82].

(1) Maxwell model [83]

The Maxwell model combines springs and dashpots in a series (cf. Figure 2.17a). Under an applied axial stress, the total stress σ_{Total} and the total strain ε_{Total} can be defined as follows:

$$\sigma_{Total} = \sigma_D = \sigma_S \tag{2.13}$$

$$\varepsilon_{Total} = \varepsilon_D + \varepsilon_S \tag{2.14}$$

where the subscript D indicates the stress/strain in the dashpot and the subscript S indicates the stress/strain in the spring. Taking the derivative of strain with respect to time, we obtain:

$$\frac{d\varepsilon_{Total}}{dt} = \frac{d\varepsilon_D}{dt} + \frac{d\varepsilon_S}{dt} = \frac{\sigma}{\eta} + \frac{1}{E}\frac{d\sigma}{dt} \tag{2.15}$$

where E is the elastic modulus of the spring and η is viscosity of the dashpot.

This model is good at predicting stress relaxation after the load is removed for many polymeric materials. However, it is not ideal for predicting the creep behaviour since it describes the strain relationship with time as linear. Equation 2.15 is used to describe the response of soft solids: thermoplastic polymers in the vicinity of their melting temperature, fresh concrete (neglecting its ageing), numerous metals at a temperature close to their melting point.

(2) Voigt-Kelvin model [83, 84]

The Voigt-Kelvin model connects spring and dashpot in parallel (cf. Figure 2.17b). Therefore, the strains in each component are identical:

$$\varepsilon_{Total} = \varepsilon_D = \varepsilon_S \tag{2.16}$$

The total stress will be the sum of the stress in each component:

$$\sigma_{Total} = \sigma_D + \sigma_S \tag{2.17}$$

From these equations we get that in a Kelvin-Voigt material, stress σ, strain ε and their rates of change with respect to time *t* are governed by equation:

$$\sigma(t) = E\varepsilon(t) + \eta\frac{d\varepsilon(t)}{dt} \tag{2.18}$$

The equation can be applied either to the shear stress or normal stress of a material.

This model is extremely good to describe the creep of materials, but in respect to relaxation behaviour after the load is removed the model is much less accurate. Its applications cover organic polymers, rubber, and wood when the load is not too high.

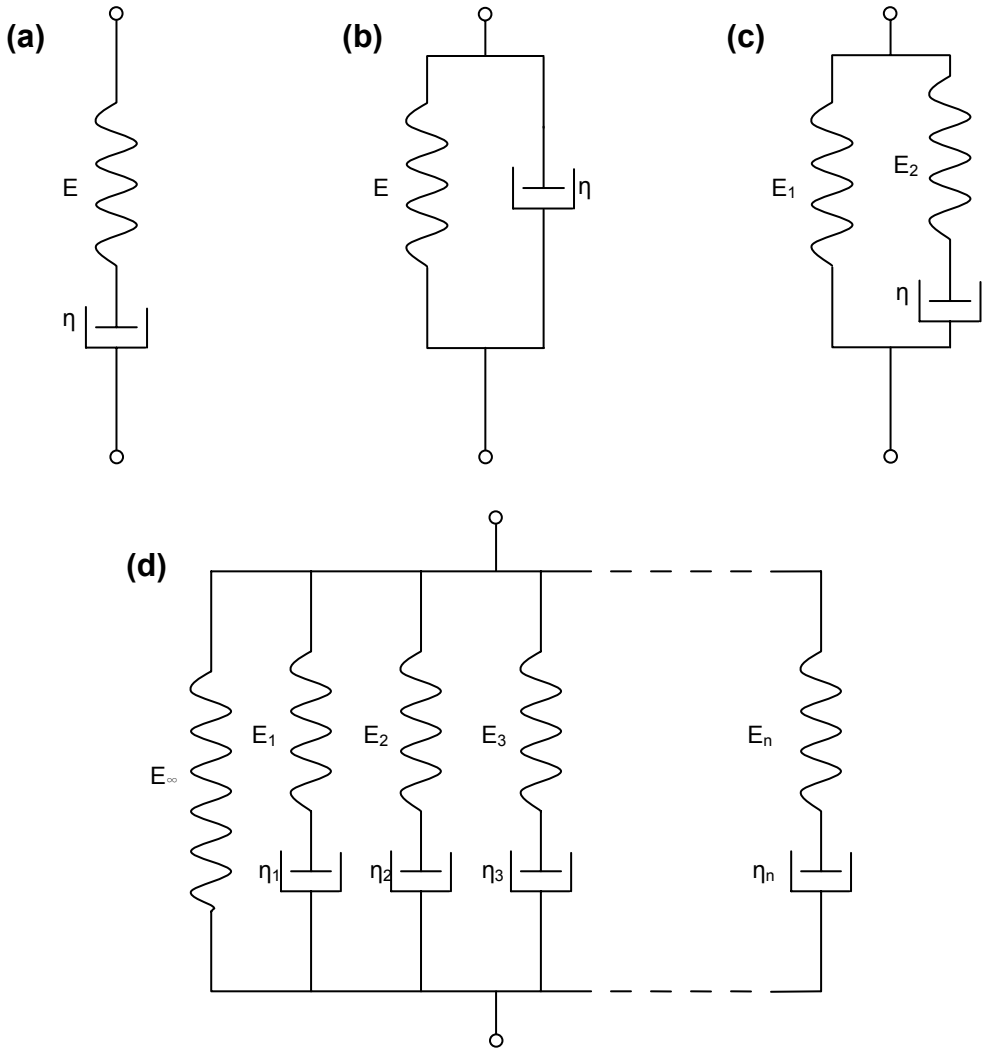

Figure 2.17 Constitutive models of linear viscoelasticity. (a) Maxwell model, (b) Voigt-Kelvin model, (c) Standard Linear Solid Model, (d) Generalized Maxwell Model. Note that E_i is the elastic modulus of the material, η_i is the viscosity of the material.

(3) Standard Linear Solid Model [84]

The Standard Linear Solid Model (cf. Figure 2.17c) effectively combines the Maxwell Model and a Hookean spring in parallel.

For parallel components:

$$\sigma_{Total} = \sigma_1 + \sigma_2 \tag{2.19}$$

$$\varepsilon_{Total} = \varepsilon_1 = \varepsilon_2 \tag{2.20}$$

For series components:

$$\sigma_{Total} = \sigma_1 = \sigma_2 \tag{2.21}$$

$$\varepsilon_{Total} = \varepsilon_1 + \varepsilon_2 \tag{2.22}$$

For the overall system:

$$\sigma_{Total} = \sigma_M + \sigma_{S1} \tag{2.23}$$

$$\varepsilon_{Total} = \varepsilon_M = \varepsilon_{S1} \tag{2.24}$$

$$\sigma_M = \sigma_D = \sigma_{S2} \tag{2.25}$$

$$\varepsilon_M = \varepsilon_D + \varepsilon_{S2} \tag{2.26}$$

where the subscripts M, D, S1,and S2 refer to Maxwell, dashpot, spring one, and spring two, respectively.

So the system can be modeled as:

$$\frac{d\varepsilon}{dt} = \frac{\frac{E_2}{\eta}\left(\frac{\eta}{E_2}\frac{d\sigma}{dt} + \sigma - E_1\varepsilon\right)}{E_1 + E_2} \tag{2.27}$$

τ is relaxation time and equal to

$$\tau = \frac{\eta}{E_2} \tag{2.28}$$

The Standard Linear Solid model combines aspects of the Maxwell and Kelvin-Voigt models to accurately describe the general shape of the strain curve, as well as the behaviour of the material applied to an instantaneous stress. However, it lacks the ability to accurately model material systems numerically and in addition, it is rather difficult to calculate.

(4) Generalized Maxwell model [82]

The Generalized Maxwell also known as the Maxwell-Weichert model (cf. Figure 2.17d) is the most general one among the above mentioned ones. It takes into account that relaxation does not occur at a single time, but at a distribution of time representing the different lengths of molecular segments. Note that the shorter segments contribute less to relaxation than the longer ones. This model represents

accurately the relaxation time distribution by having as many spring-dashpot Maxwell elements, as necessary.

2.4.2 Mooney-Rivlin Material Model

Besides the linear viscoelasticity of the polymers which can be described with the Generalized Maxwell Model, the incompressibility and the non-linear behaviour (non-linear stress-strain curve) can be represented by a certain class of strain energy functions. This function can be used to consider the large strain of elastic materials. The form of this function is [85]:

$$W = C_{10}(I_1 - 3) + C_{01}(I_2 - 3) + C_{11}(I_1 - 3)(I_2 - 3) + C_{20}(I_1 - 3)^2 + C_{30}(I_1 - 3)^3 \quad (2.29)$$

where W is the strain energy, I_1, I_2 are the first and second invariants of the elastic strain. C_{10}, C_{01}, C_{11}, C_{20} and C_{30} are material constants.

This strain energy function can describe the Mooney-Rivlin materials (C_{11}, C_{20}, and C_{30} are zero), which is often used to model the elastic response of rubber-like materials.

2.4.3 Realization of generalized Maxwell Model and Mooney-Rivlin Material Model in MSC.Marc [5]

The viscoelastic properties can be investigated by dynamic mechanical thermal analysis (DMTA) test where the frequency of the applied stress (or strain) and the temperature are changed in parallel (cf. Figure 2.18a). Figure 2.18a shows the tensile mode for the DMTA measurement. Another method is the stress relaxation measurement where a constant strain is applied on the specimen and the reaction force is detected as a function of the time. This measurement is repeated at different temperatures in a wide temperature range. Figure 2.18b shows the single cantilever clamp configuration in DMTA equipment for stress relaxation measurement.

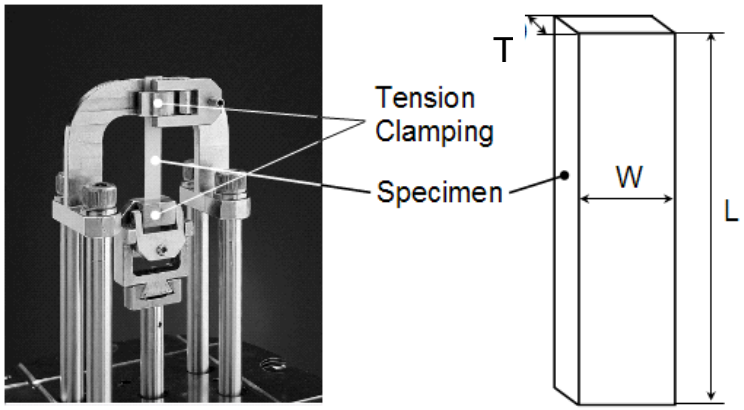

Figure 2.18a Picture of the tension grip with the specimen (W-width, L-length, T-thickness).

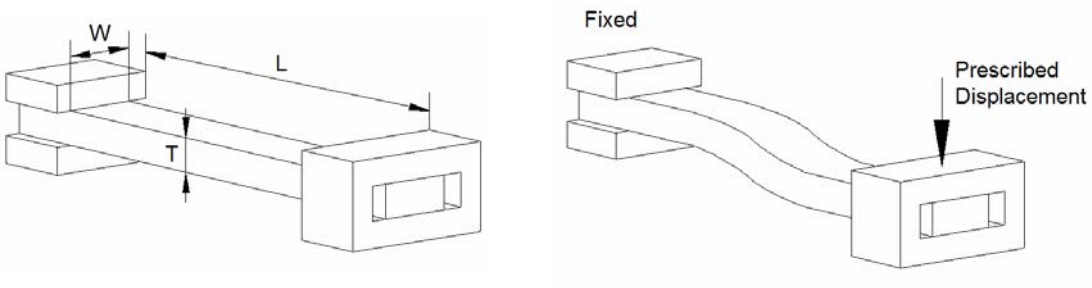

Figure 2.18b Schematic sketch of the single cantilever grip with the specimen (W-width, L-length, T-thickness).

As a result of the DMTA measurements, one can get the change of the storage (E´), and loss moduli (E´´), as well as of the loss factor (tan δ) versus the applied frequency and versus the temperature (cf. e.g. Figure 2.19 left). Based on the Williams-Landel-Ferry (WLF) equation master curves can be created for the storage modulus, loss modulus and loss factor [86] (e.g. cf. Figure 2.19 right). This happens by choosing the reference temperature (e.g. 20 °C) and shifting every other curve into the right direction by the right shift factor. The master curves represent the change of the storage modulus/loss modulus/loss factor versus frequency.

By fitting an n-term ($n \leq 15$) Maxwell Model to the measured master curve, the parameters of the Maxwell Model (relaxation time (t) and dimensionless elastic modulus (spring-dashpot constant) (e) of each Maxwell-element) are specified for the MSC.Marc FE software:

$$E_0 = E_1 + E_2 + ... + E_{15} + E_\infty \tag{2.30}$$

$$e_i = E_i / E_0 \tag{2.31}$$

$$t_i = \eta_i / E_i \tag{2.32}$$

where E_i is the elastic modulus of the spring, η_i is the viscosity coefficient of the dashpot, t_i is the relaxation time constant of each spring-dashpot element.

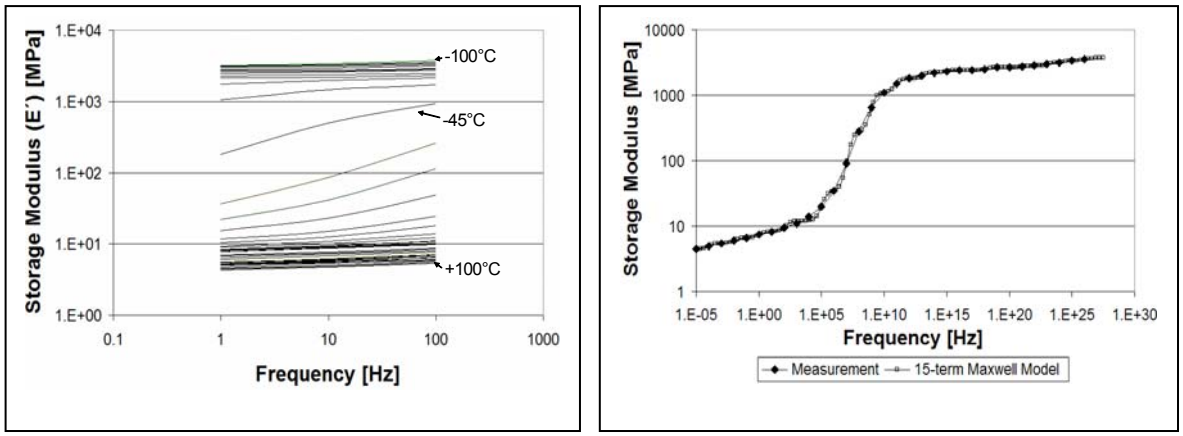

Figure 2.19 Storage modulus curves at different temperatures (left) and storage modulus master curve of the EPDM rubber; reference temperature T_{ref} = 20 °C (right) [5].

The constants of the two term Mooney-Rivlin Model could be calculated by simplified equations [85]:

$$E = 6(C_{10} + C_{01}) \tag{2.33}$$

$$4 = C_{10}/C_{01} \tag{2.34}$$

where, C_{10} - first Mooney-Rivlin parameter, C_{01} - second Mooney-Rivlin parameter, E - Young's modulus (viz. E_0 in Equation 2.30).

3 Objectives

Rubbers and their composites, distinguishing themselves by large elasticity from thermosets and thermoplastics, and with distinct characteristics from metals and ceramics, have their own wide application fields. Moreover, they have replaced some other engineering materials due to their qualified properties and low cost. Although the existing elastomer systems serve mostly satisfactorily, elastomer composites can be further reinforced and their property profile varied by adding additives or mixing with other polymers. Note that the type and amount of filler/polymer have a big influence on the behaviours of the materials produced. In many engineering applications the friction and wear properties are key parameters, which can hardly be predicted being a very complex issue due to the viscoelasticity of the elastomers. Although the tribological performance of elastomer system has been studied in detail, their friction and wear under rolling conditions received far less attention than those grouped into abrasion, erosion, fretting and scratch types. Due to difference between sliding, abrasion and the like, and rolling type of wear the state of knowledge on the former friction types can not be transferred for rolling friction and wear. It is therefore essential to study the rolling friction and wear of elastomers.

Therefore, the aim of this work is to develop rubber compounds with enhanced resistance to rolling wear. In detail, the rolling friction and wear properties of various rubbery materials (rubber compounds with various fillers, with different filler contents, and rubber blends) were studied by both experimental and numerical methods. The phase structure and physico-mechanical properties of the elastomer systems were assessed accordingly. The reinforcing effect of additives (filler and blend component) on the rubber matrix was determined as a function of recipe (type and content of different additives, fillers). Finally, considerable effort was devoted to model the friction behaviour by making use of the FE technique. The FEM was adopted to both testing configurations, i.e. Orbital-RBOP and Oscillating-RBOP rigs.

4 Experimental

4.1 Materials

4.1.1 Elastomers

4.1.1.1 EPDM_CB

The rubber stocks were prepared in a laboratory internal mixer and the curatives were introduced on a laboratory open mill. The EPDM recipe used was as follows: EPDM (Keltan® 512 of DSM Elastomers, Sittard, The Netherlands): 100 part; CB (N550): 0, 30, 45 and 60 part; ZnO: 5 part; stearic acid: 1 part; sulphur: 1.5 part; N-cyclohexyl-2-benzothiazole sulfenamide (CBS, Vulkacit CZ of Bayer, Leverkusen, Germany): 0.6 part; 2-mercapto benzothiazole (MBT, Vulkacit Mercapto by Bayer): 0.6 part; zinc dicyanatodiamine (Rhenogran Geniplex 80 of Rhein Chemie, Mannheim, Germany): 0.6 part; zinc dibenzyl dithiocarbamate (Rhenogran ZBEC-70 of Rhein Chemie): 1.5 part. Note that the CB content was varied between 0 and 60 parts per hundred part rubber (phr). Rubber sheets (ca. 2 and 4 mm thick) were produced by compression molding at 160 °C and 7 MPa pressure using a laboratory press (Weber, Remshalden, Germany). The vulcanization time was selected by considering the thickness of the specimens and the time needed for the 90% crosslinking of the rubber at T= 160 °C. The latter time was deduced from the torque-time curves registered by Monsanto moving die rheometer (MDR 2000 EA-1). The rubbers are further on referred to as EPDM_0/30/45/60CB (the last digits in the designations represent the CB contents).

4.1.1.2 HNBR_CB/silica/MWCNT

The composition of the peroxide curable HNBR was shown in Table 4.1. This mix was produced separately and provided by Lanxess (Leverkusen, Germany). The curing time of this base mix to reach 90% crosslinking was ca. 10 min at T= 175 °C. This peroxide curable HNBR was mixed with 20 phr CB (N550), 10/20/30 phr silica (Ultrasil® VN2 of Degussa, Frankfurt, Germany) and MWCNT (Baytubes® C 150 P from Bayer MaterialScience, Leverkusen, Germany), respectively, on a two-roll mixing mill (LRM-150BE of Labtech, Bangkok, Thailand) at ca. 40 °C by setting a friction ratio of 1.15.

Table 4.1 Compound formation.

	HNBR_PURE (peroxide curable HNBR) [part]
HNBR (Therban® LT VP/KA 8882 of Lanxess, Leverkusen, Germany; acrylonitrile content: 21%, Mooney viscosity ML(1+4)100 °C=74)	100
diphenylamine-based thermostabilizer (Luvomaxx CDPA of Lehmann & Voss, Hamburg, Germany)	1.1
zinc-containing mercapto-benzimidazole compound (Vulcanox® ZMB 2/C5 of Lanxess)	0.4
di(tert-butylperoxyisopropyl)benzene (Perkadox 14-40 B-PD of Akzo-Nobel, Düren, Germany; active peroxide content: 40%)	7.5
MgO	2
triallyl isocyanurate	1.5
ZnO	2

Curing of the CB, silica and MWCNT filled HNBR to about 2 mm thick sheets (100 x 100 mm^2 surface) occurred at T = 175 °C for 15 min in a laboratory press. Specimens for the investigations listed below were cut from these sheets.

The samples prepared are referred to as HNBR_PURE, HNBR_20CB, HNBR_10/20/30silica and HNBR_10/20/30MWCNT, respectively. The digits in the designations represent the content of fillers in phr.

4.1.2 Blends

4.1.2.1 Elastomer/elastomer: HNBR-FKM_MWCNT

The composition of the HNBR was as indicated in section 4.1.1.2. As peroxide curable FKM Viton GF-600S of DuPont Performance Elastomers (Geneva, Switzerland) was selected. Its fluorine content is 70 wt%, and its Mooney viscosity-

ML (1+4) 121 °C: 65. This FKM was added to the above ready-to-cure HNBR by setting the following HNBR/FKM ratios: 100/0, 100/33.3 and 100/100. The related HNBR/FKM mixtures were produced on a two-roll mixing mill (LRM-150BE of Labtech, Bangkok, Thailand) at ca. 50°C by setting a friction ratio of 1.35. To the above mixtures 10 phr MWCNT (Baytubes® C 150 P from Bayer MaterialScience, Leverkusen, Germany) was incorporated in the above mentioned laboratory mill. Note that the cure recipe was not adjusted, i.e. the ready-to-cure HNBR was just diluted by FKM. This means that a direct comparison can only be made between rubber compounds with and without MWCNT filler when their HNBR/FKM ratio is the same. Curing of the rubbers into 2 mm thick sheets (100 x 100 mm^2 surface) occurred at T= 175 °C for 15 min in a laboratory press. The specimens for the investigations were cut from these sheets.

The rubbers involved are further on referred to as HNBR_PURE, HNBR_10MWCNT, HNBR-FKM 100-33.3, HNBR-FKM 100-33.3 MWCNT, HNBR-FKM 100-100, and HNBR-FKM 100-100 MWCNT, respectively.

4.1.2.2 Elastomer/thermoplastic: HNBR-(p)CBT/pCBT

The same HNBR was chosen as in section 4.1.1.2. It was mixed with 50, 100 and 150 phr cyclic butylene terephthalate (CBT® 160, Cyclics Europe, Schwarzheide, Germany) on a two-roll mixing mill (LRM-150BE of Labtech, Bangkok, Thailand) at ca. 40 °C by setting a friction ratio of 1.15. Note that this CBT contained already the polymerization catalyst.

Curing of the HNBR both in presence and absence of CBT occurred at 190 °C for 25 min in a laboratory press. Recall that the temperature is higher and the time is longer than needed to cure the HNBR. However, this processing window was adapted to the polymerization requirements of CBT® 160. The obtained mixes are further on referred to as HNBR-(p)CBT 100-0, 100-50, 100-100 and 100-150, respectively. Note that the digits in these designations represent the phr contents of rubber and CBT, respectively.

Cured sheets were subjected to an annealing process in order to check whether the CBT polymerization can be completed. The sheets were dried at 100 °C for 1 hour (h), and subsequently heated to and kept at 250 °C for 3 h under vacuum in a

thermostatic oven. Afterwards, the oven was cooled to room temperature. The annealed hybrids, for sake of comparison with the not annealed ones, are referred to as HNBR-pCBT 100-0, 100-50, 100-100 and 100-150, respectively. Recall that the designations (p)CBT and pCBT consider a slightly and almost fully polymerized CBT, respectively, in the related hybrid systems. Specimens for the investigations were cut from these sheets of ca. 2 mm thickness.

4.2 Testing

4.2.1 Phase structure

4.2.1.1 Differential scanning calorimetry (DSC) [87]

DSC is a thermoanalytical technique in which the difference in the amount of heat required to increase the temperature of a sample and reference are measured as a function of temperature. Both the sample and reference are maintained at nearly the same temperature throughout the experiment. Generally, the temperature is designed to increase/decrease linearly as a function of time. The reference sample should have a well-defined heat capacity over the range of temperatures to be scanned. The basic principle underlying this technique is that, when the sample undergoes a physical transformation such as phase transitions, more or less heat will need to flow to it than the reference to maintain both materials (sample, reference) at the same temperature. Whether more or less heat must flow to the sample depends on whether the process is exothermic or endothermic. The main application of DSC is to study phase transitions, such as melting, glass transitions, or exothermic decompositions, etc., which involve energy changes or heat capacity changes.

The result of a DSC experiment is a curve of heat flux versus temperature or versus time. There are two different conventions: exothermic reactions in the sample shown with a positive or negative peak; it depends on the different kind of technology used by the instrumentation to make the experiment.

Figure 4.1 is a schematic DSC curve demonstrating the appearance of several common features. Glass transition appears as a step in the recorded DSC curve. This is due to a change in heat capacity; no formal phase change occurs. As the temperature increases, at some point the molecules may obtain enough freedom of

motion to spontaneously arrange themselves into a crystalline form. This is known as the crystallization temperature, which is an exothermic process and hence results in a peak in the DSC signal. As the temperature increases the sample eventually reaches its melting temperature (T_m). The melting process results in an endothermic peak in the DSC curve.

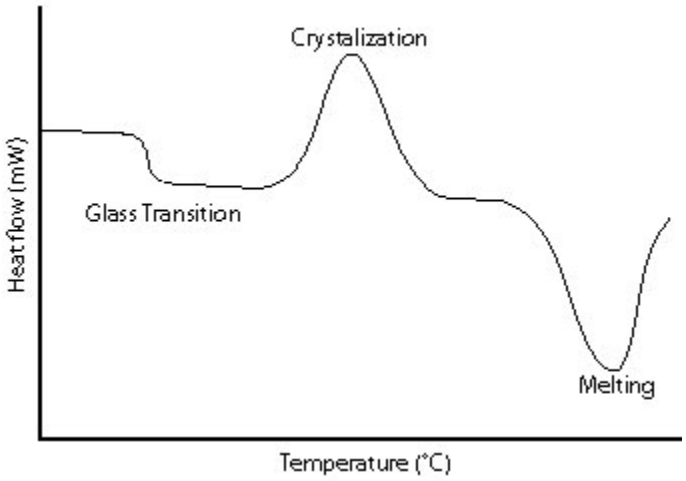

Figure 4.1 A schematic DSC curve demonstrating the appearance of several common features.

In the present work the DSC traces were registered in a DSC device (DSC821e of Mettler Toledo, Giessen, Germany) in a temperature range from 25 to 250 °C at heating and cooling rates of 10 °C/min.

4.2.1.2 Dynamic-mechanical thermal analysis (DMTA)

DMTA, as the name implies, is a very useful technique for observing the viscoelastic nature of polymers. In the measurement a constant strain is applied on the specimen and the reaction force is detected as a function of the time. This measurement is repeated at different temperatures in a wide temperature range (stress relaxation measurement). Another method is to change the frequency of the applied stress (or strain) and the temperature in parallel (cf. section 2.4.3). This method is the most commonly used one today. Samples can be either solids or melts. The testing modes

include tensile, compressing, shearing, bending, torsion, etc (cf. Figures 2.18 and 2.19, section 2.4.3). The output data are stress, strain, time, temperature, frequency, storage modulus, loss modulus, loss factor, etc. By scanning the temperature range from glassy to rubbery state, the T_g can be observed [88].

In this work DMTA spectra were measured on rectangular specimens in tensile mode at a static preload 0.01 N with a superimposed sinusoidal 0.01 % strain. The frequency was 1, 10 and 100 Hz and the spectra were registered in a broad temperature range (from -100 °C to +100/240 °C) using a Q800 device of TA Instruments (New Castle, DE, USA). From -100 °C, the temperature was increased by 5 °C per step and for each step the temperature was stabilized for 3 min. Note that -100 °C to +240 °C was only for HNBR-CBT compounds, -100 °C to +100 for the rest materials.

4.2.1.3 Transmission electron microscopy (TEM)

TEM is a microscopy technique whereby a beam of electrons is transmitted through an ultra thin specimen, interacting with the specimen as it passes through. An image is formed from the interaction of the electrons transmitted through the specimen; the image is magnified and focused onto an imaging device, such as a fluorescent screen, on a layer of photographic film, or to be detected by a sensor such as a charge-coupled device (CCD) camera. TEMs are capable of imaging at a significantly higher resolution than light microscopes, owing to the small de Broglie wavelength of electrons. This enables the instrument to be able to examine fine detail - even as small as a single column of atoms, which is tens of thousands times smaller than the smallest resolvable object in a light microscope [89].

TEM measurements were carried out with a Zeiss LEO 912 Omega transmission electron microscopic (Oberkochen, Germany) applying an acceleration voltage of 120 kV. Thin sections (ca. 50 nm) were cut at -120 °C with a Diatome diamond knife (Hatfield, PA, USA) using a cryochamber equipped Ultracut microtome (Reichert and Jung, Vienna, Austria).

4.2.1.4 Atomic force microscopy (AFM) [90-92]

AFM is a very high-resolution type of scanning probe microscope, with demonstrated resolution of fractions of a nanometer, more than 1000 times better than the optical diffraction limit. The AFM is one of the foremost tools for imaging, measuring and manipulating matter at the nanoscale. The information is gathered by "feeling" the surface with a mechanical probe.

Figure 4.2 shows the scheme of the AFM. The AFM consists of a microscale cantilever with a sharp tip at its end that is used to scan the specimen surface. The cantilever is typically silicon or silicon nitride with a tip radius of curvature on the order of nanometers. When the tip is brought into proximity of a sample surface, forces between the tip and the sample lead to a deflection of the cantilever according to Hooke's law. Depending on the situation, forces that are measured in AFM include mechanical contact force, Van der Waals forces, capillary forces, chemical bonding, electrostatic forces, magnetic, Casimir forces, solvation forces etc. As well as force, additional quantities may simultaneously be measured through the use of specialized types of probe. The scanning motion is conducted by a piezoelectric tube scanner which scans the tip in a raster pattern with respect to the sample (or scans to the sample with respect to the tip). Typically, the deflection is measured using a laser spot reflected from the top surface of the cantilever into a split photodiode detector (photdetector). By detecting the difference in the detector output voltages, changes in the cantilever deflection or oscillation amplitude (i.e. surface information) are determined.

The AFM can be operated in a number of modes, depending on the application. The two most commonly used ones are contact mode and tapping mode, which are conducted in air or liquid environments. In contact mode, the force between the tip and the surface is kept constant during scanning by maintaining a constant deflection.

Tapping mode consists of oscillating the cantilever at its resonance frequency and lightly “tapping” on the surface during scanning. The advantage of tapping mode with respect to contact mode is that it eliminates the lateral, shear forces present in contact mode. This enables tapping mode to image soft, fragile, and adhesive surfaces without damaging them, which can be a drawback of contact mode. Phase

imaging is a powerful extension of tapping mode that provides nanometre-scale information about surface structure and properties. To minimize the influence of the roughness of the surface, the very smooth scan surfaces are required.

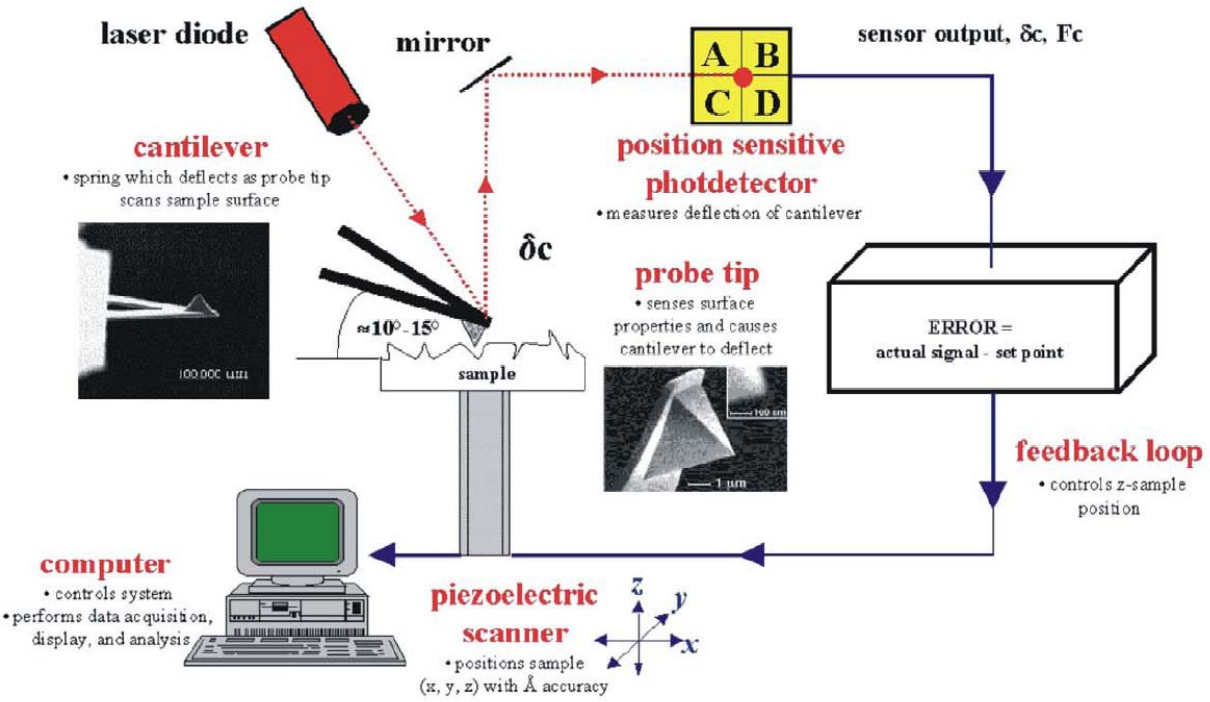

Figure 4.2 Scheme of the major components of an AFM showing the feedback loop for tapping mode operation.

AFM analysis was performed in tapping mode with a scanning probe microscope system (Veeco, Santa Barbara, CA, USA). The Si tipped cantilever (length: 250 µm, spring constant: ~ 20 N/m) operated at a resonant frequency of ~ 350 MHz during the AFM scans.

Amplitude and phase images were taken from the cryofractured surfaces of the rubber compounds. For HNBR-FKM, samples were produced by cutting after immersion in liquid nitrogen. For HNBR-CBT, the samples were broken by tongs after immersion in liquid nitrogen. The AFM scans were executed immediately after producing the broken or cut surfaces of the compounds.

4.2.1.5 Wide-angle X-ray scattering (WAXS) [93]

WAXS is an X-ray diffraction technique that is often used to determine the crystalline structure of polymers. This technique specifically refers to the analysis of Bragg Peaks scattered to wide angles, which (by Bragg's law) implies that they are caused by sub-nanometer sized structures. The diffraction pattern allows determining the chemical composition or phase composition of the film, the crystallite size, etc.

During the measurement the sample is scanned in a wide angle X-ray goniometer, and the scattering intensity is plotted as a function of the 2θ angle. When X-rays are directed in solids they will scatter in predictable patterns based upon the internal structure of the solid. A crystalline solid consists of regularly spaced atoms (electrons) that can be described by imaginary planes. The distance between these planes is called the d-spacing. The intensity of the d-space pattern is directly proportional to the number of electrons (atoms) that are found in the imaginary planes. Every crystalline solid has a unique pattern of d-spacing. The solids with the same chemical composition but different phases can be identified by their pattern of d-spacing.

The WAXS spectra in the present work were recorded by a D500 X-ray diffractometer from Siemens (Munich, Germany). Copper anode in conjunction with a secondary beam monochromator were used to separate the Cu K_α radiation (λ= 0.1504 nm). The WAXS spectra were taken in a 2θ (theta) range from 5 to 45 °.

4.2.1.6 Extraction

Extraction was carried out for HNBR-CBT hybrids to clarify the polymerization ratio of CBT. Because chloroform can solve only unpolymerized CBT and does not attack polymerized CBT, it was chosen as solvent for extraction.

During the process the hybrid compounds of HNBR-(p)CBT/pCBT were kept in chloroform for about 3 days at room temperature. After that, all samples were dried in an oven that was kept at 70 °C for about 3 h. The mass loss was calculated by considering the mass of the samples before and after extraction.

4.2.2 Physico-mechanical properties

4.2.2.1 Density

The density (ρ) of a material is defined as its mass per unit volume. Different materials usually have different densities. Archimedes' principle (buoyancy method with water) was adopted according to the ISO 1183 standard in this work.

Archimedes' principle

It was named after Archimedes (287 BC-212 BC), who first discovered this law. According to Archimedes' principle, "Any object, wholly or partly immersed in a fluid, is buoyed up by a force equal to the weight of the fluid displaced by the object." Archimedes' principle does not consider the surface tension (capillarity) acting on the body. The weight of the displaced fluid is directly proportional to the volume of the displaced fluid (if the surrounding fluid is of uniform density) [94].

The density of the immersed object can easily be calculated without measuring any volumes:

$$\rho_{object} = \frac{m_{air}}{m_{air} - m_{liquid}} \rho_{liquid} \tag{4.1}$$

where ρ_{object} and ρ_{liquid} are the density of the object and the liquid, respectively.

4.2.2.2 Hardness

Hardness is defined as the resistance of a solid material against the penetration of another harder material. The Martens (earlier termed as universal) hardness is the test force divided by the apparent area of the indentation under applied test force [95]. So during this test, the values for the calculation of the hardness are determined under the applied test force. An advantage of this method is the fully automatic measurement of the indentation depth. Another one is the registration of the force/indentation depth values and the benefit of further information in addition of the hardness value, especially the parts of plastic and elastic deformation. For the studied rubber compounds and blends, the Martens hardness was determined according to the standard ISO 14577-1 (2002) in a Shimadzu DUH 202 device of Shimadzu Corporation (Kyoto, Japan) with a Vickers-type diamond indenter. The testing parameters were: maximum force: 5 mN, holding time: 2 seconds.

4.2.2.3 Surface tension [96-98]

Surface tension is an attractive property of the surface of a liquid. It causes the surface portion of liquid to be attracted to another surface. Wetting is the ability of a liquid to maintain contact with a solid surface, resulting from intermolecular interactions when the two are brought together. The degree of wetting (wettability) is determined by a force balance between adhesive and cohesive forces. Therefore they can reflect the surface adhesion by which the surface enrichment of FKM in the blend of HNBR-FKM can be determined.

To check the change in the wettability (surface tension) of the HNBR due to FKM and MWCNT modifications the sessile drop technique has been adopted.

In this technique, a small liquid droplet is placed on a flat horizontal solid surface and the contact angle is measured. The contact angle is defined as the angle made by the intersection of the liquid/solid interface and the liquid/air interface. The contact angle is specific for any given system. The shape of the droplet is determined by the Young Relation. A low contact angle indicates a high solid surface energy or chemical affinity, and a high degree of wetting (cf. Figure 4.3a). A high contact angle indicates a low solid surface energy or chemical affinity. This is also referred to as a low degree of wetting (cf. Figure 4.3b). Contact angle is measured using a contact angle goniometer.

To the surface (cleaned by isopropylalcohol) of the rubber sheets a drop of double distilled water was placed and the contact angle determined using a goniometer of Ramé-Hart (Mountain Lakes, NJ, USA). It was proved that this kind of cleaning did not influence the contact angle data. The reported mean values were derived from at least 10 contact angle measurements.

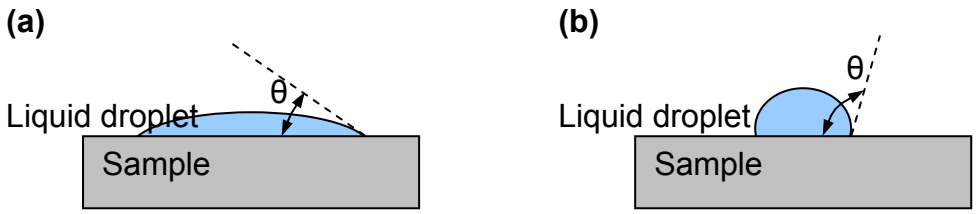

Figure 4.3 Schematic sketch of a water drop on a solid surface in case of hydrophilic (a) and hydrophobic material (b).

4.2.3 Rolling friction and wear

4.2.3.1 Testing

The rolling tribological properties of elastomer system were determined in Orbital- and Oscillating-RBOP test configurations.

In the home-made Orbital-RBOP test rig (cf. Figure 2.5), the rubber sheet is worn by a steel ball (100Cr6, diameter: 14 mm, arithmetical roughness R_a: 1 µm), rolling along a circular path (diameter: 33 mm), pushed by a defined normal load against the rubber sheet. In the Oscillating-RBOP configuration (cf. Figure 2.9), the reciprocating linear rolling of the ball (100Cr6, diameter: 14 mm, arithmetical roughness R_a: 1 µm) occurs at a frequency of 1 Hz with peak-to-peak amplitude of 25.06 mm under a given load applied by a lever system for a fixed duration. The parameters chosen for the configurations were varied for different materials (cf. Table 4.2).

These two tribotesting devices allowed recording the dynamic COF as a function of time. The average of the on-line COF recorded by the testing machines in the whole experimental duration were calculated and shown in the part of experimental results.

The specific wear rate was computed according to equation 2.12. The loss volume (ΔV) (cf. Equation 2.12) was calculated by measuring the depth and width of the wear track and estimating it as a half ellipse. The cross section of the wear track was assessed by a white light profilometer (see 4.2.3.2).

Table 4.2 Experimental conditions for researched elastomer system in Orbital- and Oscillating-RBOP.

No.	Elastomer system	Orbital-RBOP			Oscillating-RBOP	
		Normal load [N]	Revolution [rpm]	Duration [h]	Normal load [N]	Duration [h]
1	EPDM_CB	150	300	3	150	6
2	HNBR_CB/silica/MWCNT	90	280	3		
3	HNBR-FKM_MWCNT	90	280	3		
4	HNBR-(p)/pCBT	90	280	3		

4.2.3.2 Wear mechanisms

The worn surfaces were investigated in a MicroProf white light profilometer (Fries Research & Technology, Bergisch Gladbach, Germany) and in SEM (JSM-6300 of Jeol, Tokyo, Japan and ZEISS SupraTM 40VP, Oberkochen, Germany). The specimens were sputtered with an Au/Pd alloy in a device of Balzers (Lichtenstein) prior to SEM investigation to avoid electrostatic charging.

White light profilometer can scan the wear track and create the surface topography image with the collected data. In this way, the dimension of the wear track can be determined and the wear loss can be calculated.

The SEM is a type of electron microscope that images the sample surface by scanning it with a high-energy beam of electrons in a raster scan pattern [99, 100]. The electrons interact with the atoms that make up the sample producing signals that contain information about the sample's surface topography, composition and other properties such as electrical conductivity. The types of signals produced by an SEM include secondary electrons, back scattered electrons, characteristic x-rays, light (cathodoluminescence), specimen current and transmitted electrons. These types of signal all require specialized detectors for their detection that are not usually all

present on a single machine. The signals result from interactions of the electron beam with atoms at or near the surface of the sample. In the most common or standard detection mode, secondary electron imaging, the SEM can produce very high-resolution images of a sample surface, revealing details about 1 to 5 nm in size. So, SEM micrographs have a very good depth resolution yielding a characteristic three-dimensional appearance which is most useful for understanding the surface structure of a sample.

The various tests adopted for the researched elastomer system are collected in Table 4.3 (marked by X or test name).

Table 4.3 Test methods used for the elastomer systems.

No.	Elastomer system	DSC	DMTA	AFM	Den -sity	Hard- ness	WAXS/TEM/ Extraction/Surfa -ce tension/FEM	Rolling wear
1	EPDM_CB					X	FEM	both
2	HNBR_CB /silica/MW CNT		X		X	X		Orbital
3	HNBR-FKM_MW CNT		X	X	X	X	TEM/Surface tension/FEM	Orbital
4	HNBR-(p)CBT/pCBT	X	X	X	X		WAXS/Extraction/FEM	Orbital

4.3 Finite element (FE) modelling

The FEM models of both Orbital- and Oscillating-RBOP tests are composed of a sphere, defined as rigid body, a rubber plate, defined as deformable body, and a rigid flat surface which was glued onto the bottom of the rubber plate. The dimension of

the models was according to the practical tests. The diameter of the ball was 14 mm, unchangeable with the rig type or material.

The rubber plate was built up from 8-node solid elements. There was no friction applied between the rigid sphere and the rubber plate.

The simulation conditions for Orbital-RBOP test were normal load: 170 for EPDM_30CB and 90 N for HNBR-FKM/(p)CBT 100-100, ball revolution: 3 rpm (20 sec/cycle), duration: 1 cycle; for Oscillating-RBOP tests were normal load: 140 N, cyclic frequency: 1/30 Hz, duration: 1 cycle.

One may notice that the revolution of the ball in Orbital-RBOP tests is much smaller than that in the experimental part of the present work. It has to be underlined that the Orbital-RBOP machine can record at most 15 data per minute. In this situation, if the ball rotated too fast, the recorded data were too few to describe a cycle properly. Then the comparison between experimental and simulated results could not be considered as accurate. The revolution of the guiding ring of 6 rpm (ca. 3 rpm of the steel ball) was almost the lowest speed the machine could provide. So “3 rpm of the ball” was chosen as the simulation condition. Afterwards, the electrical modification to the machine could record the data at every 0.001 sec. However, the revolution for FEM was not changed to be uniform with the results got before the improvement of the machine. For Oscillating-RBOP tests, the frequency of the ball was also reduced compared to that of the experiments. The highest recording frequency of the machine is 1 sec^{-1}. Note that the adopted frequency in the experiments was 1 Hz, i.e. 1 cycle per second. The 1 datum recorded for one cycle can not be used to describe one cycle. Therefore the frequency was decreased to 1/30 Hz in the simulation. However with this setting the simulation results can still be validated and the FEM can be proved whether it considers the viscoelasticity of the rubbers properly.

The normal load was applied by the prescribed displacement of the ball. The ball moved vertically (z direction, cf. Figures 4.4 and 4.5) till a fixed position (d_z) and pressed onto the rubber plate in the time duration 0-1 s (cf. Figure 4.6 tc1). After this the ball remained unchangeable in direction z until the end of the cycle. To ensure the fixed normal force in Orbital-RBOP and Oscillating-RBOP, this value d_z is diverse for different materials. The simulation of the ball’s movement on the rubber plate was realized by the combination of the rotation of the ball (around y axis) and the

movement of the rubber plate (uniform rotation of the rubber plate around z axis for Orbital-RBOP and horizontal oscillation in direction x for Oscillating-RBOP) (cf. Figures 4.4 and 4.5). The movement of the rubber plate was realized by setting the rigid surface moving in the defined way. Note that this rigid surface was glued to the bottom of the rubber plate and hence the rubber would move identically as the surface.

The friction force, normal force and COF spectra got from simulation in one cycle were compared with the results from verification tests.

4.3.1 Model building for Orbital-RBOP

In the Orbital-RBOP rig the rubber sample was glued to the metal plate which was fixed on the machine by screws. The positions of the four screws can be seen in Figure 4.7. For amounting screws the four corners of the tested rubber samples were cut and hence the rubber plate was with the shape depicted in Figure 4.7. The FEM model was built accordingly and the initial meshing of the rubber plates is displayed in Figure 4.4a. Table 4.4 lists the initial number of elements for selected rubber compounds. To increase the accuracy of the simulation and to decrease the computing time at the same time, the “local adaptivity” of mesh adaptivity was turned on for EPDM_30CB. In this way the number of elements in the chosen region was increased when a given mean strain energy density was reached. In the work this value was fixed at 1.5 N/mm^2. It was applied to the whole upper layer elements. The re-meshed elements of the rubber plate at t= 9 s are visible in Figure 4.4b. For HNBR-FKM 100-100 and HNBR- (p)CBT 100-100 mesh adaptivity was turned off because the computer can not deal with so much elements. The angular velocity for the rigid surface (viz. rubber plate) and the rigid sphere was 0 in 0-1 s. In 1-20 s it is 0.314 and 0.741 rad/s (3 rpm) for the rigid surface and sphere, respectively. Note that the additional spin of the steel ball was not involved in the model.

Table 4.4 Rubber plate dimension and number of elements in FEM simulation.

	Orbital-RBOP			Oscillating-RBOP		
	Length	Width	Thickne	Length	Width	Thickne

	[mm]	[mm]	ss [mm]	[mm]	[mm]	ss [mm]
EPDM_30CB	48	48	4	37.6	27.4	4
	1152 elements			38	28	4
				4256 elements		
HNBR-FKM 100-100	48	48	2	37.6	27.4	2
HNBR-(p)CBT 100-100	48	48	2	37.6	27.4	2
	4000 elements			38	28	2
				2128 elements		

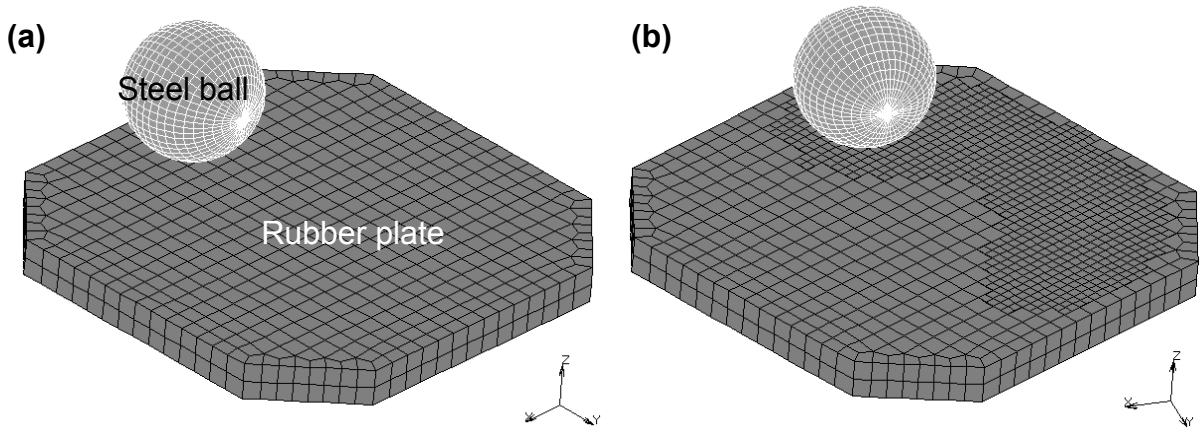

Figure 4.4 FE model for the Orbital-RBOP (dimension 48 mm x 48 mm x 4 mm). (a) original meshing of the rubber plate, (b) remeshing during simulation.

4.3.2 Model building for Oscillating-RBOP [5]

The FEM model of Oscillating-RBOP is shown in Figure 4.5. The dimension and the initial number of elements for the rubber plates are also in Table 4.4. Mesh adaptivity was applied only to the deeper colour elements shown in Figure 4.5a. The re-meshed elements of the rubber plate at t= T/2 are visible in Figure 4.5b.

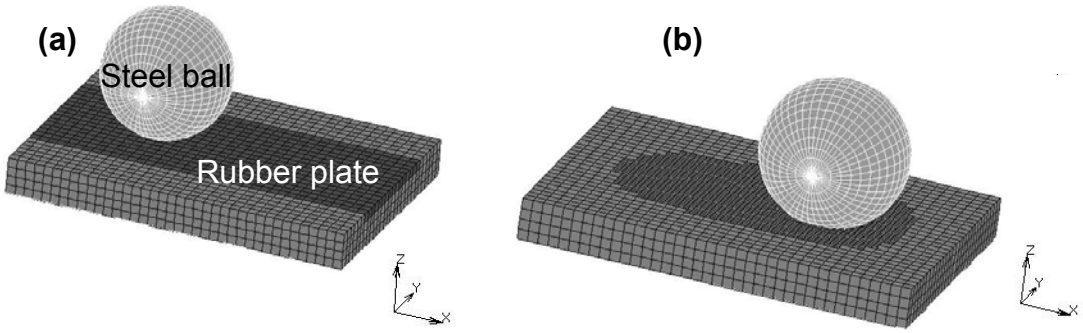

Figure 4.5 FE model for the Oscillating-RBOP (dimension 37.6 mm x 27.4 mm x 4 mm). (a) original meshing of the rubber plate, (b) remeshing during simulation.

The horizontal movement of the rigid surface at the bottom of the rubber plate and the rotation of the sphere can be driven by the same time curve (cf. Figure 4.6 tc2). Considering the value of the sinusoidal time curve (tc2) is zero from t= 0 s to t= 1 s, the velocity of the rubber plate and the angular velocity of the sphere can be described as:

$$v(t) = 1.47\sin\left(\frac{\pi}{15}(t-1)\right) \left[\frac{mm}{s}\right] \tag{4.2}$$

$$\omega(t) = 0.21\sin\left(\frac{\pi}{15}(t-1)\right) \left[\frac{rad}{s}\right] \text{ if } 1s \le t \le 31s. \tag{4.3}$$

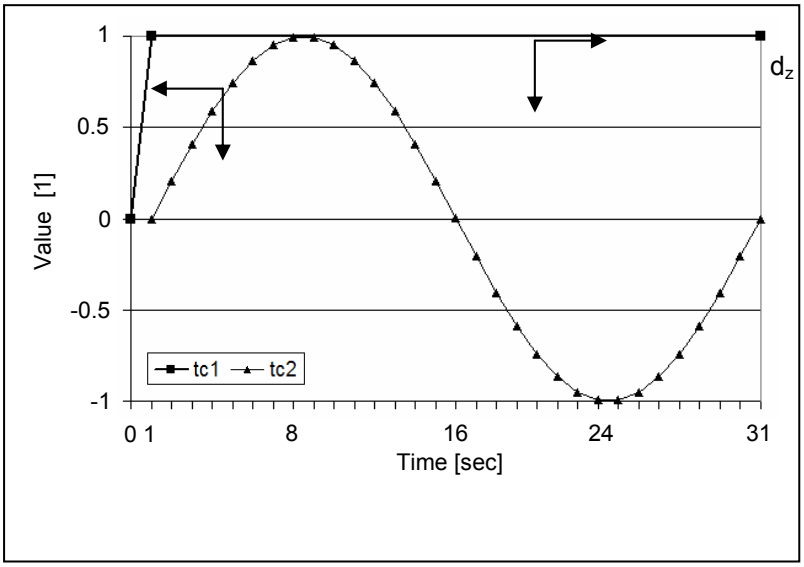

Figure 4.6 Driving time curves for the vertical displacement of the sphere (tc1) for Oribtal- and Oscillating-RBOP tests, for the horizontal velocity of the rubber plate (tc2) and for the angular velocity of the sphere (tc2) for Oscillating-RBOP tests.

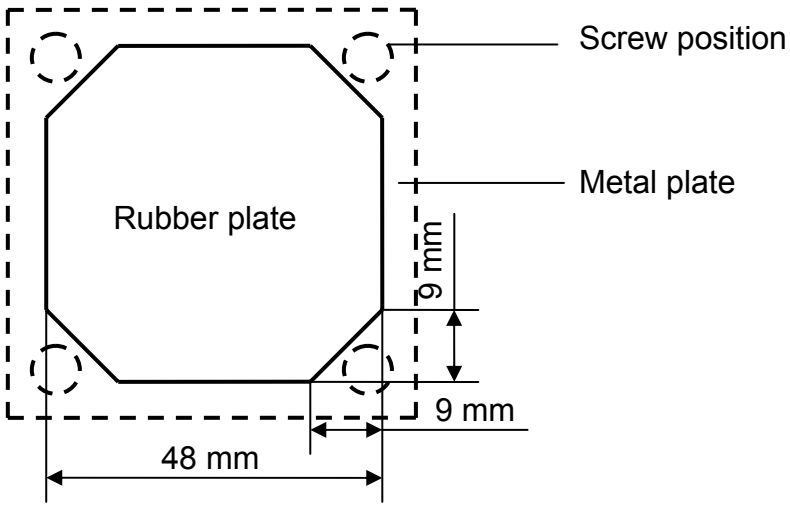

Figure 4.7 Rubber plate sample and the glued metal plate in the Orbital-RBOP tests (top view).

5 Experimental results and discussion

5.1 Traditional elastomers

5.1.1 EPDM_CB: effects of CB

5.1.1.1 Martens hardness

For EPDM rubbers, the Martens hardness increases with increasing CB content (cf. Table 5.1).

Table 5.1 Martens hardness of the EPDM_CB compounds.

	EPDM_0	EPDM_30	EPDM_45	EPDM_60
Martens hardness [MPa]	1.84±0.34	3.28±0.35	7.00±1.48	7.13±1.37

5.1.1.2 Friction and wear

The COF (line) and the specific wear rate (column) of the EPDM rubbers with varying CB contents measured in Orbital-RBOP and Oscillating-RBOP configurations, respectively, are summarized in Figure 5.1. One could get the impression that incorporation of CB increases the COF marginally and decreases the W_s. Note that the COF in Orbital-RBOP configuration is higher than in Oscillating-RBOP for EPDM system. In Orbital-RBOP, already 30 phr CB reduces the W_s markedly compared to the neat material. In Oscillating-RBOP, the specific wear rate seems to decrease monotonously with increasing CB content for EPDM rubbers.

5.1.1.3 Wear mechanisms

5.1.1.3.1 Orbital-RBOP

SEM photos taken from the worn surface of EPDM_0CB after Orbital-RBOP test are shown in Figure 5.2. For the reason mentioned in section 2.3.1.3.2, the worn characteristics are demonstrated separately for the outer, centre and inner region. In

the outer region, massive cracking occurs which is likely due to the missing CB reinforcement (cf. Figure 5.2a). In the centre debris are accumulated (cf. Figure 5.2b). In the inner region, ploughing, tearing events dominate (cf. Figure 5.2c).

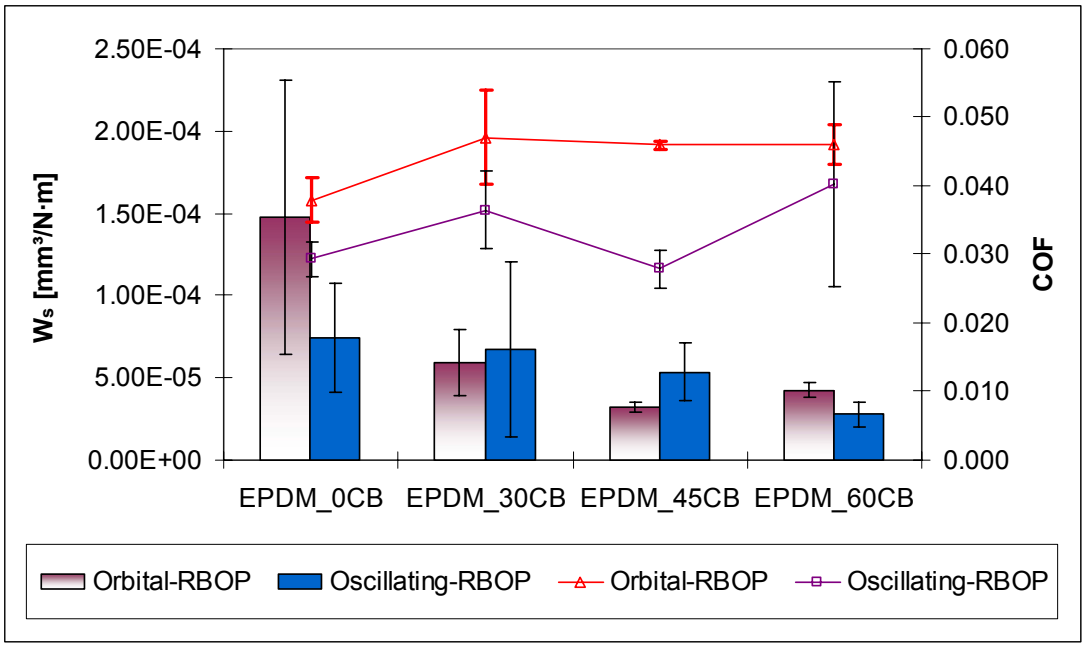

Figure 5.1 Changes of COF (line) and W_s (column) for EPDM_CB in Orbital-RBOP and Oscillating-RBOP tests as a function of CB's content.

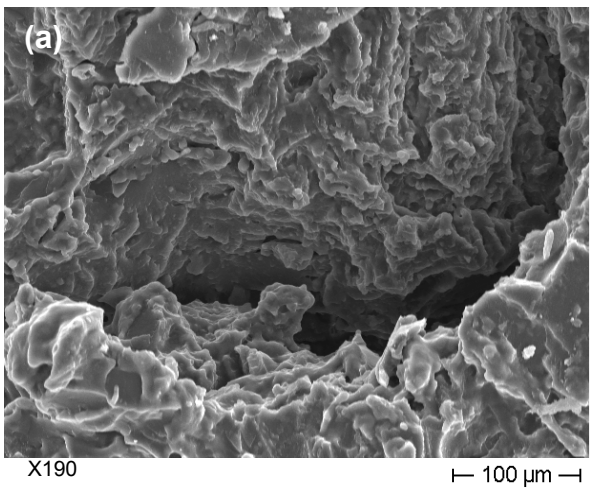

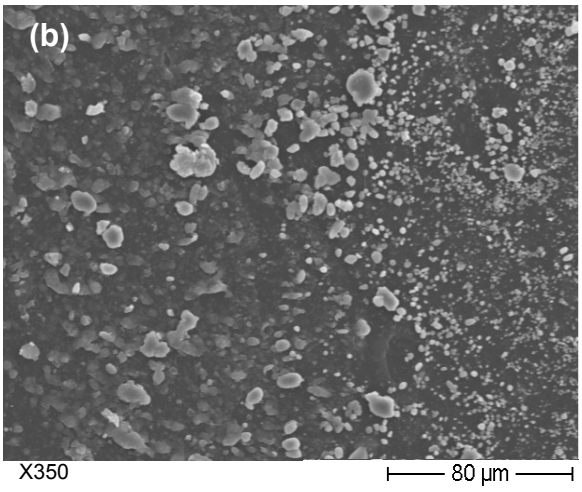

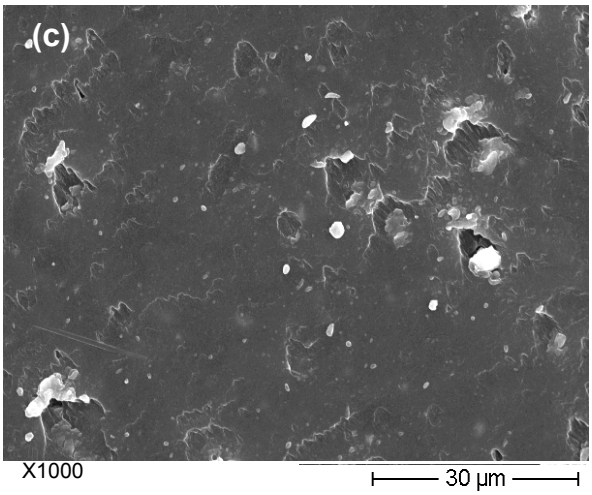

Figure 5.2 SEM photos taken from the rolling wear track of EPDM_0CB after Orbital-RBOP test. (a) outer region, (b) centre region, (c) inner region. Note: rolling direction is downward.

Incorporation of 30 phr CB changes the wear mechanisms fundamentally - a Schallamach pattern [77] appears in the outer region. This is in accord with a reduced specific wear rate compared to that of EPDM_0CB. The wave fronts are more or less transversely oriented to the rolling direction (cf. Figure 5.3a). Further incorporation of CB in EPDM reduces the space between two neighbouring waves and favours roll formation. Besides, some pitting events can be discerned in the wavy pattern (cf. Figure 5.3d). The accumulation of fragments is still the characteristic for the centre region where the spin of the ball is negligible (cf. Figure 5.3b).

Fibrils are found in the inner region of the rolling wear track of EPDM_30CB (cf. Figure 5.3c). They might have been formed by tearing and rolling from earlier developed Schallamach waves. The onset of fibrils always suggests some thermal/tribochemical effects due to which the rubber is decomposed and thus well adhered to the ball. When the ball rotates away, the rubber surface tears, and yields some fibrillar structure which is disrupted further on [29].

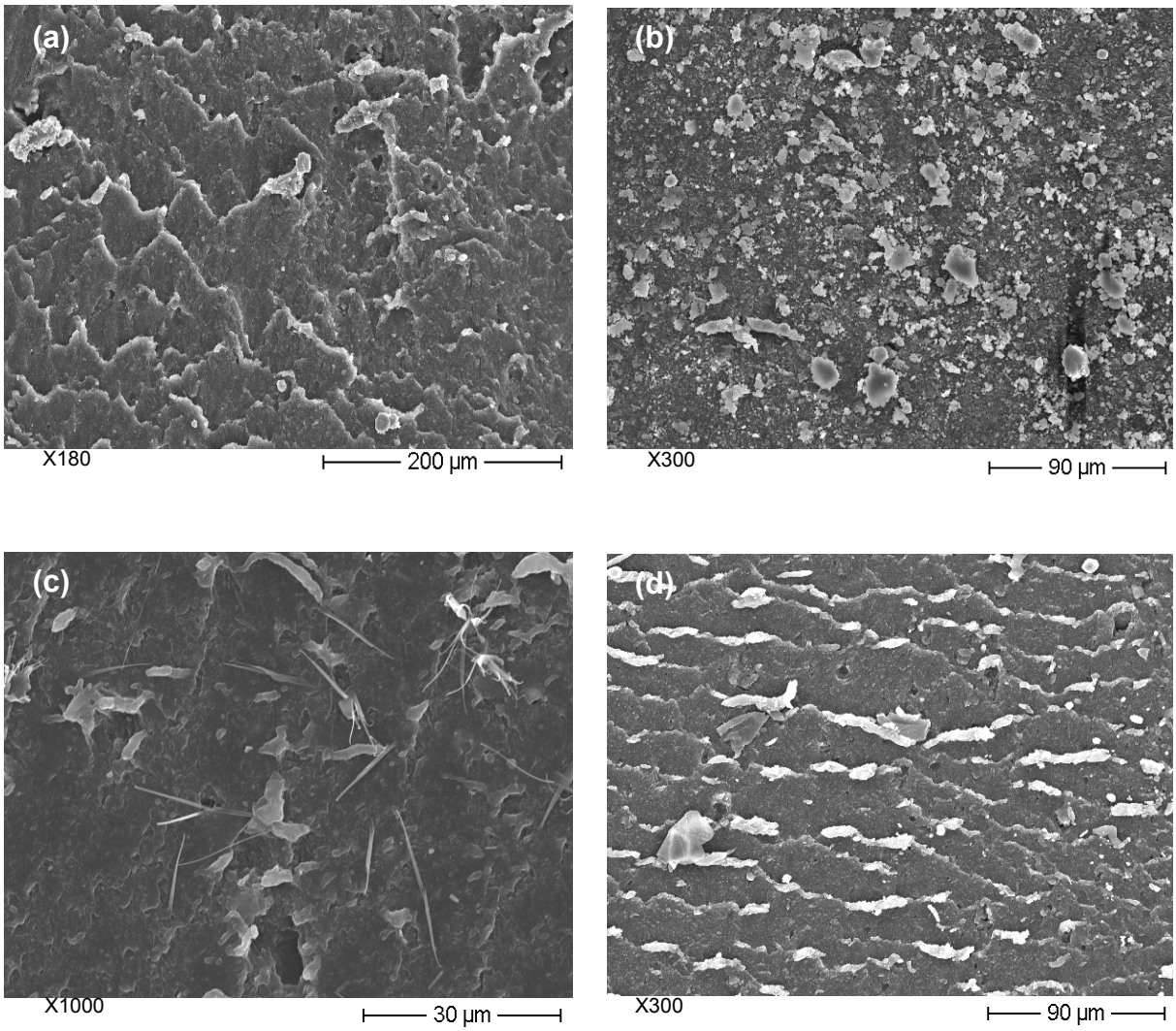

Figure 5.3 SEM photos taken from the rolling wear tracks of EPDM_30CB (a-c) and EPDM_60CB (d) after Orbital-RBOP tests. (a) outer region, (b) centre region, (c) inner region, (d) outer region. Note: rolling direction is downward.

5.1.1.3.2 Oscillating-RBOP

As described before (section 2.3.1.3.3), the wear track is divided into three regions - two side and one centre region because of the stress distribution (cf. Figure 2.10). Figure 5.4 shows an abrasion type pattern [78-80] and formation of large cracks occurring in the side regions of the rolling wear track of EPDM_0CB. No such type of feature was observed in other Oscillating-RBOP tests. Pitting, debris agglomeration and their “ironing” are discerned in the centre region (cf. Figures 5.4c and d). The

pitting is likely due to fatigue induced cracking caused by the repeated cyclic pressure exerted on the surface layer of the rubber by the steel ball.

Fatigue induced damage associated with pitting, flattened particles and fibrils can be observed in the wear track of EPDM_60CB after Oscillating-RBOP test (cf. Figure 5.5). The onset of fibrils has probably the same reason as mentioned above in respect with Orbital-RBOP. The overall smooth surface of EPDM_60CB accounts for its smaller W_s compared to EPDM_0CB.

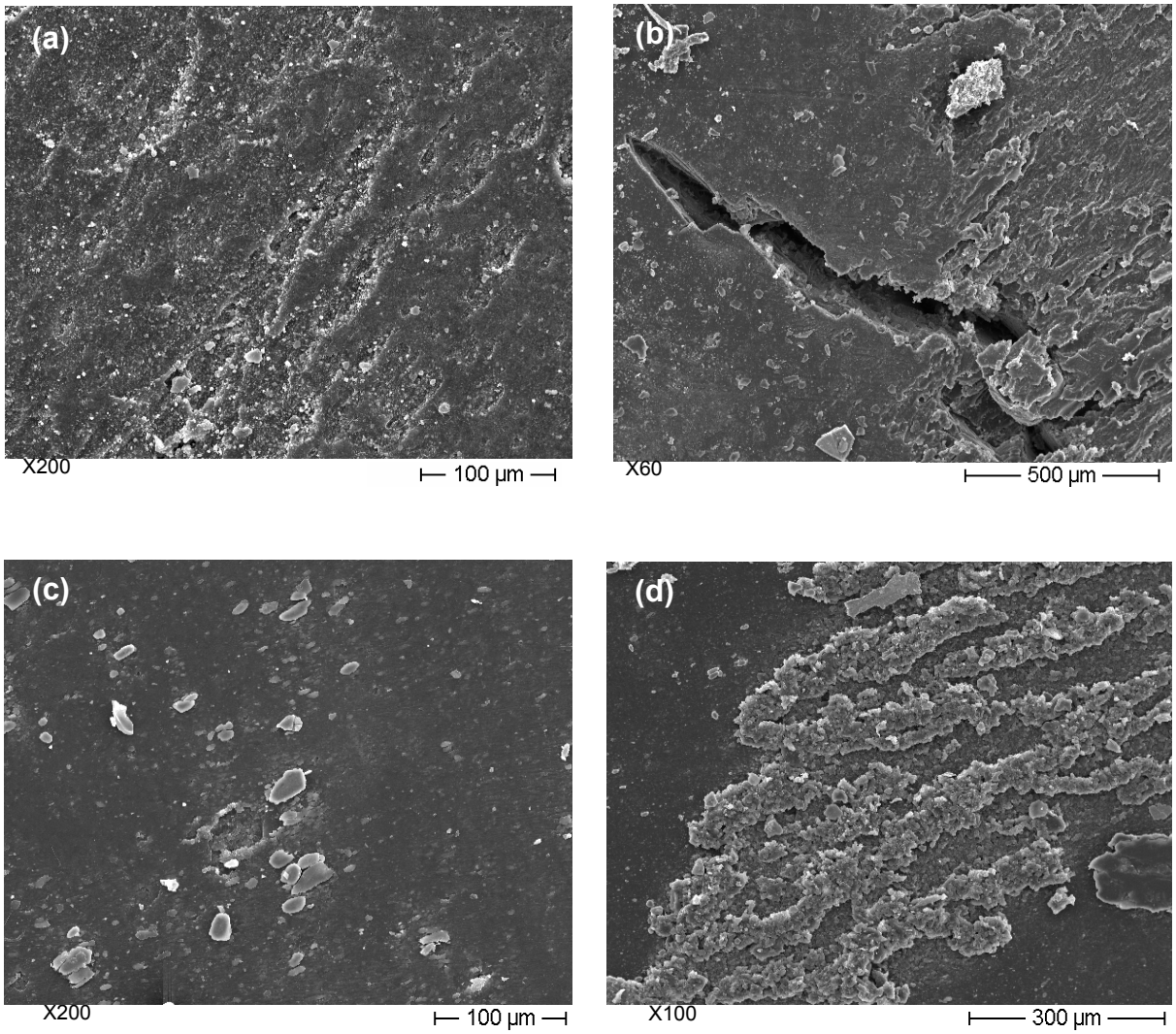

Figure 5.4 SEM photos taken from the rolling wear track of EPDM_0CB after Oscillating-RBOP test. (a) abrasion pattern in side region, (b) cracking in side region, (c) pitting in centre region, (d) agglomerate formation and their “ironing” in centre region. Note: rolling direction is vertical.

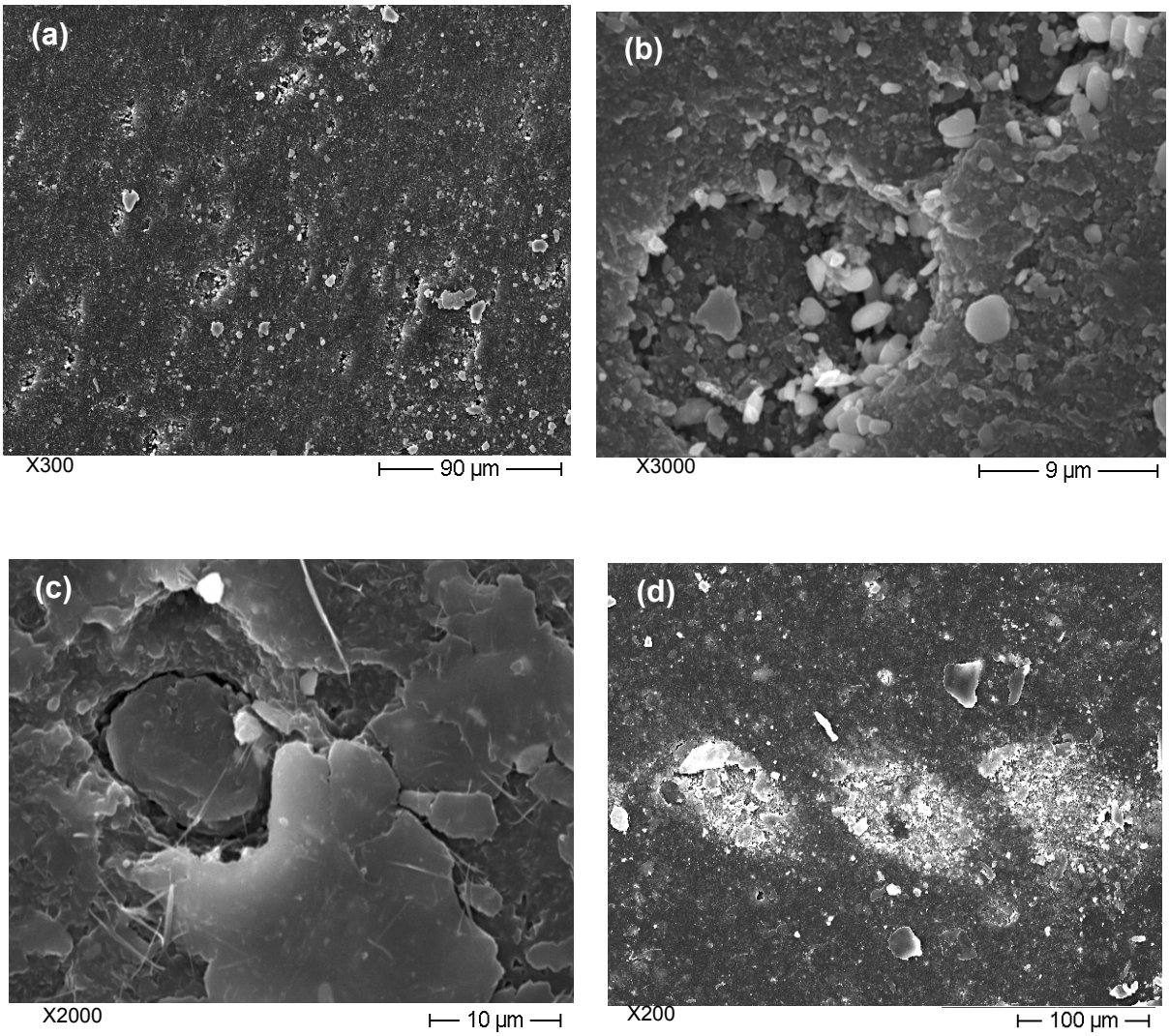

Figure 5.5 SEM photos taken from the rolling wear track of EPDM_60CB after Oscillating-RBOP test. (a) side region, (b) pitting in side region, (c) fatigue-induced surface cracking and fibril formation in side region, (d) centre region. Note: rolling direction is vertical.

By analyzing all SEM photos taken from the EPDM_CB system, it is noticed that fibrils appear in all CB containing EPDM mixes. Because the fibrils were found in both Orbital- and Oscillating-RBOP, their occurrence is not sensitive to the experimental conditions, but depends on the properties of the rubbery material. This claim is confirmed by the fact that fibril formation was observed for CB containing EPDM after dry sliding [101].

It can also be established that the reason why the COF measured in Oscillating-RBOP is lower than that measured in Orbital-RBOP lies in the movement of the ball. The ball in Orbital-RBOP rotates with an additional spin. It removes the debris from the ball's way which exerts additional resisting force to the ball.

5.1.2 HNBR_silica/MWCNT: effects of various fillers

5.1.2.1 HNBR_10/20/30silica/MWCNT: effects of fillers' content

5.1.2.1.1 Network-related properties and hardness

Figure 5.6 demonstrates the measured storage modulus (E') and loss factor (tan δ) as a function of the temperature changing from -100 to 100 °C for selected HNBR_MWCNT compounds. One can observe that with the increasing amount of MWCNT the position of the glass transition temperature of the HNBR composites (T_g ≈ -25 °C) does not shift, but the stiffness in the rubbery stage (plateau modulus, E_{pl}) of the composites increases. The storage modulus was nearly doubled with incorporation of 10 phr MWCNT compared to neat HNBR (4 -> 7 MPa, 25 °C), and increased with one magnitude when added 20 phr MWCNT (4 -> 20 MPa, 25 °C).

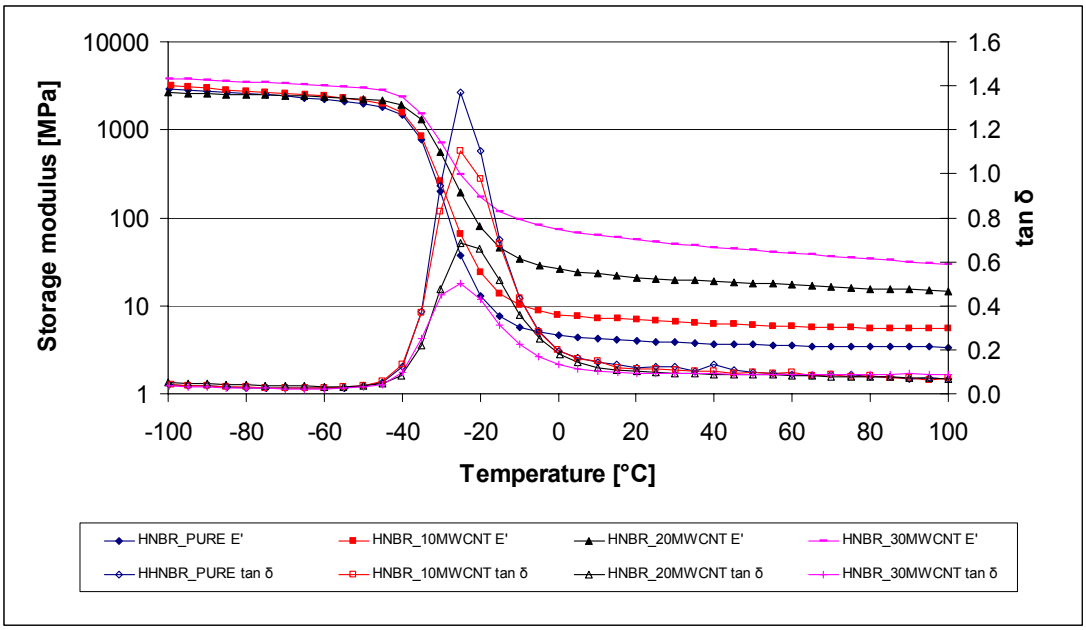

Figure 5.6 Storage modulus (E') and loss factor (tan δ) as a function of temperature for the HNBR_MWCNT compounds.

The M_c and v_c values are listed in Table 5.2. M_c and v_c decreases and accordingly increases, respectively, with the increasing content of MWCNT and silica. The minimum/maximum of M_c/v_c of HNBR_30silica and _30MWCNT reflect that they have the strongest rubber-filler and filler-filler interactions in their own series. The exception is the HNBR_10silica which has the worst crosslinking structure and therefore the smallest wear resistance compared to other silica reinforced HNBR compounds and even to the pure rubber (cf. section 5.1.2.1.2).

The density and the Martens hardness increase with the increasing amount of fillers (marginally for silica) (cf. Table 5.2). The MWCNT filled HNBR compounds have higher hardness than the HNBR mixes with the same amount of silica.

Table 5.2 Network-related properties and hardness of the HNBR_silica/MWCNT compounds.

	HNBR_PURE	HNBR_10silica	HNBR_20silica	HNBR_30silica
M_c [g/mol]	2013	2045	1437	701
v_c [mol/m^3]	525	521	765	1628
tan δ at T_g (-25 °C)	1.37	1.35	1.02	0.88
Density [g/cm³]	1.057	1.066	1.099	1.141
Martens hardness [MPa]	1.02±0.56	1.71±0.18	1.02±0.20	4.86±0.97
	HNBR_PURE	HNBR_10MWCNT	HNBR_20MWCNT	HNBR_30MWCNT
M_c [g/mol]	2013	1176	407	161
v_c [mol/m^3]	525	899	2710	7052

tan δ at T_g (-25 °C)	1.37	1.11	0.68	0.50
Density [g/cm³]	1.057	1.057	1.102	1.135
Martens hardness [MPa]	1.02±0.56	2.20±0.24	3.37±0.71	10.23±0.84

5.1.2.1.2 Friction and wear

The COF changes marginally with the increasing content of silica/MWCNT (cf. Figure 5.7). Using silica or MWCNT additives the wear resistance of the related HNBR mixes was mostly enhanced, compared to that of the pure HNBR, except HNBR_10silica. With increasing filler content the resistance to wear of the HNBR compounds is usually enhanced.

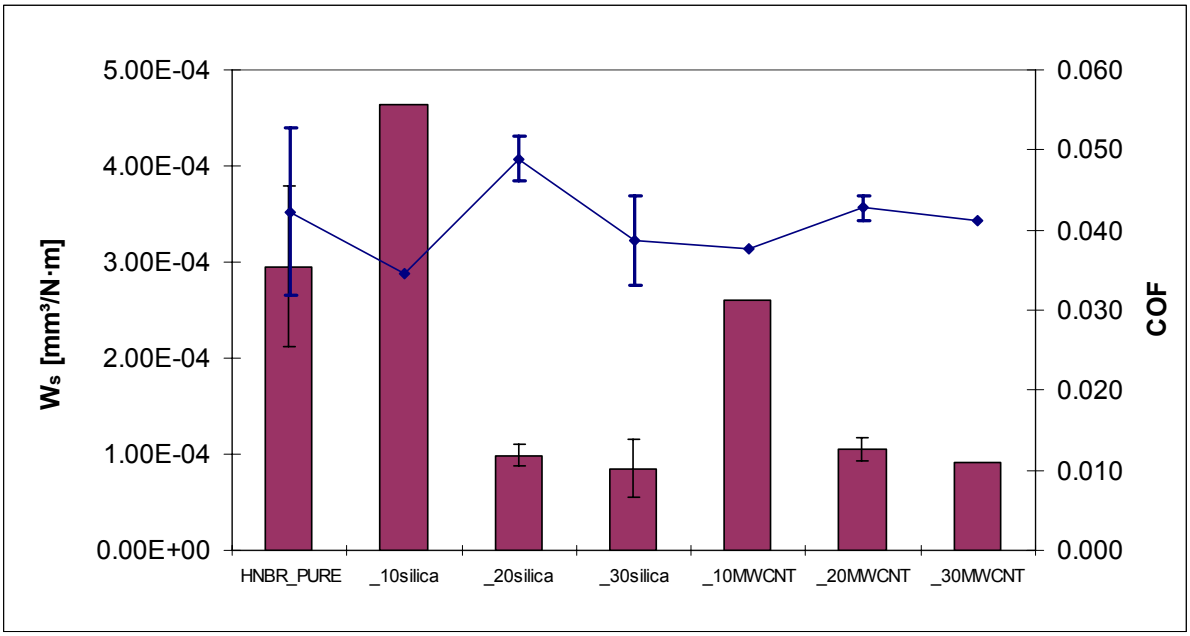

Figure 5.7 Changes of COF (line) and W_s (column) for HNBR_silica/MWCNT in Orbital-RBOP tests as a function of fillers' content.

5.1.2.1.3 Wear mechanisms

The SEM photos in Figures 5.8-5.14 were collected from the wear tracks of HNBR_PURE and HNBR-10/20/30silica/MWCNT. For the pure HNBR rubber Schallamach type pattern with roll head can be found on the both outer and inner sides of the wear track (cf. Figures 5.8a and c). The wave fronts in the two regions are adverse to each other. This reflects that the direction of the ball movement in the two regions is opposite (cf. Figure 2.8). The waves are especially well-developed in the outer side, confirming a larger speed in the outer compared to the inner region (cf. Figure 2.8). In the middle section large agglomerates can be observed (cf. Figure

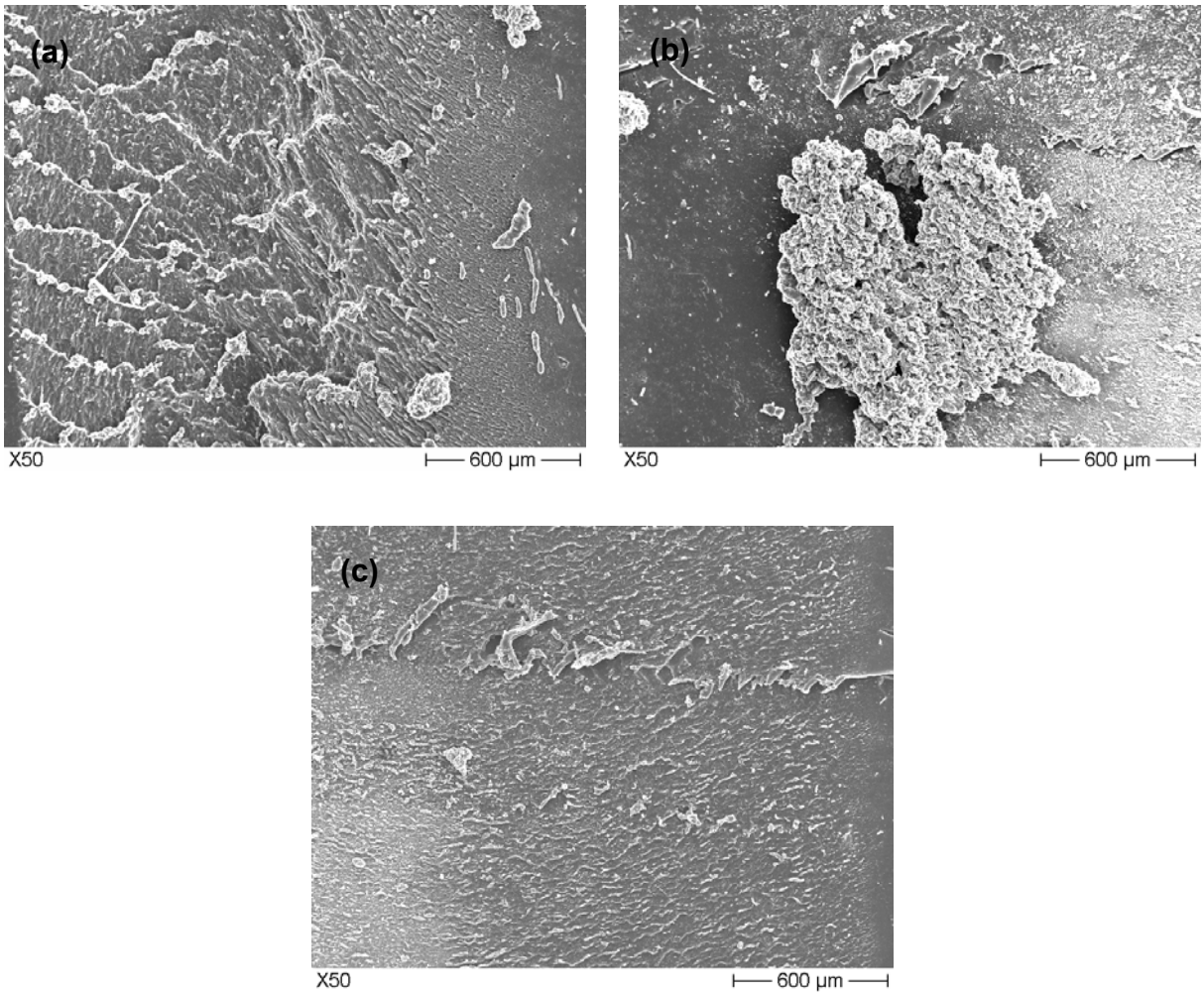

Figure 5.8 SEM photos taken from the rolling wear track of HNBR_PURE (a, b and c) after Orbital-RBOP test. (a) outer region, (b) centre region, (c) inner region. Note: rolling direction is downward.

5.8b). Note that the effect of the spin of the ball is negligible in the centre region. The debris produced in the outer and inner regions were likely swept into the centre region by the spin of the ball favouring the formation of such agglomerates.

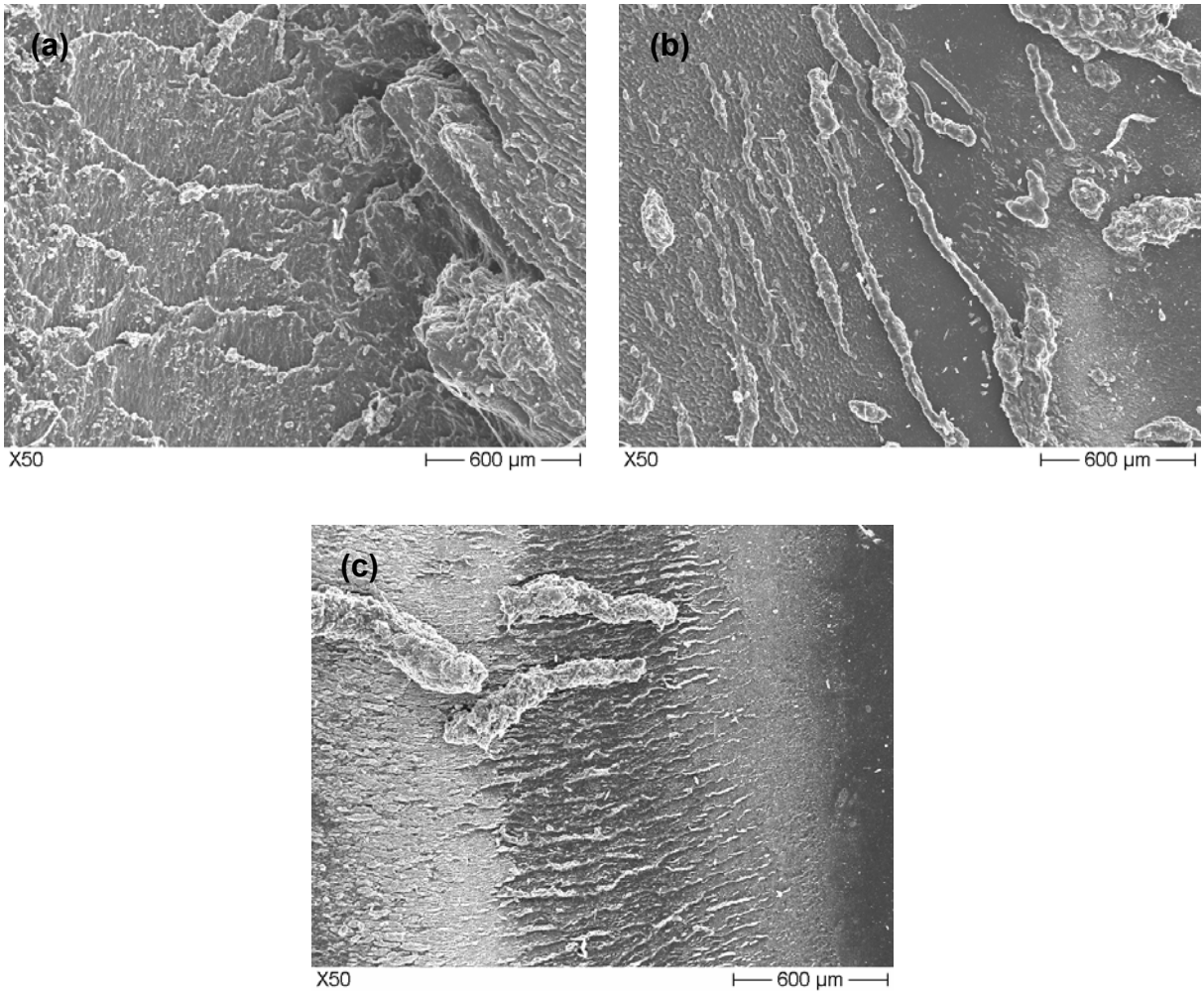

Figure 5.9 SEM photos taken from the rolling wear track of HNBR_10silica after Orbital-RBOP test. (a) outer region, (b) centre region, (c) inner region. Note: rolling direction is downward.

When the HNBR contained 10 phr silica, the wear mechanisms do not change dramatically (cf. Figure 5.9). But the Schallamach type pattern developed better than in pure HNBR. This may explain the higher W_s of this compound compared to that of HNBR_PURE. Figure 5.10 displays the worn surface of HNBR_20silica. In the outer region, Schallamach pattern with roll head, flat particles and agglomerates are

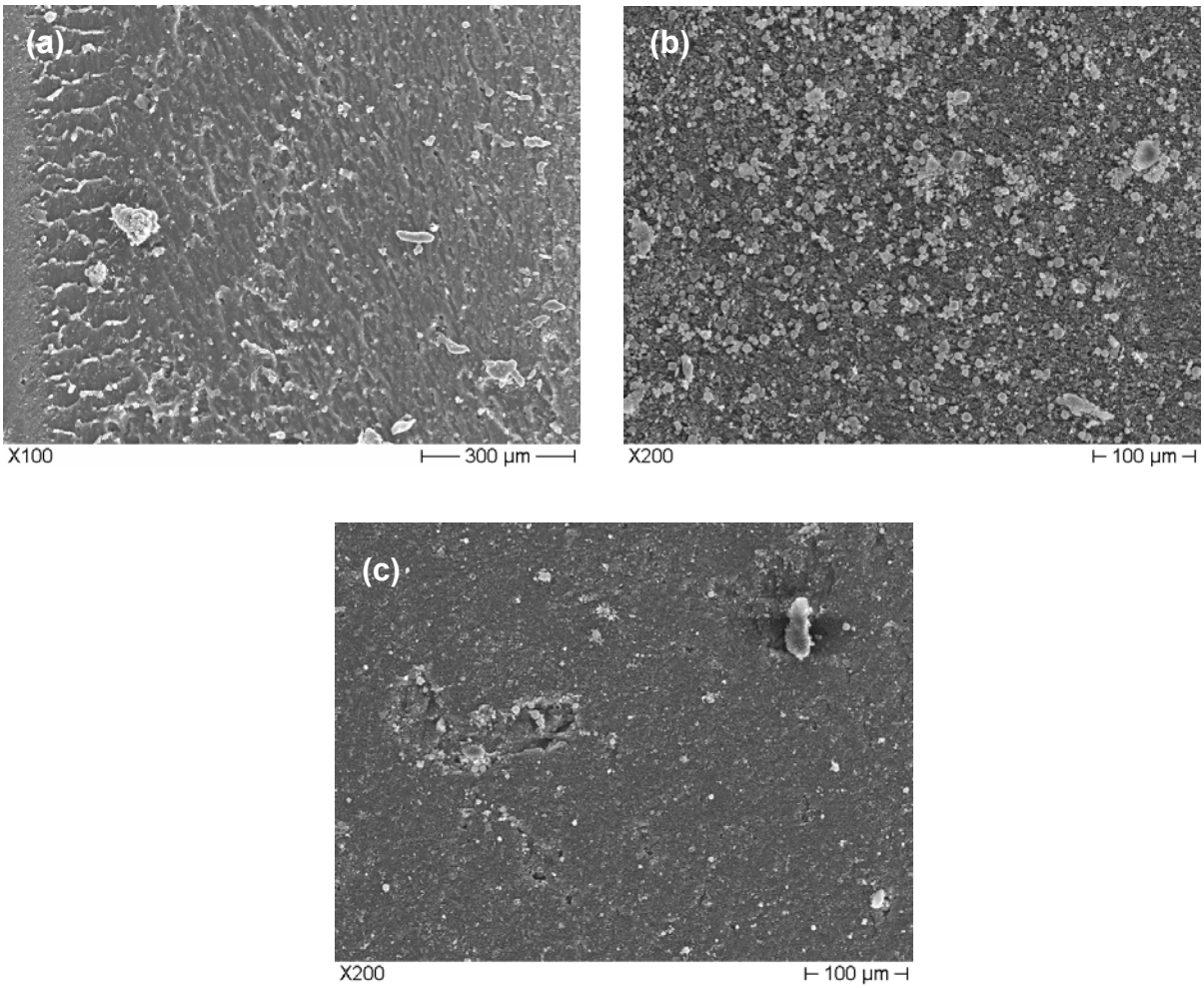

Figure 5.10 SEM photos taken from the rolling wear track of HNBR_20silica after Orbital-RBOP test. (a) outer region, (b) centre region, (c) inner region. Note: rolling direction is downward.

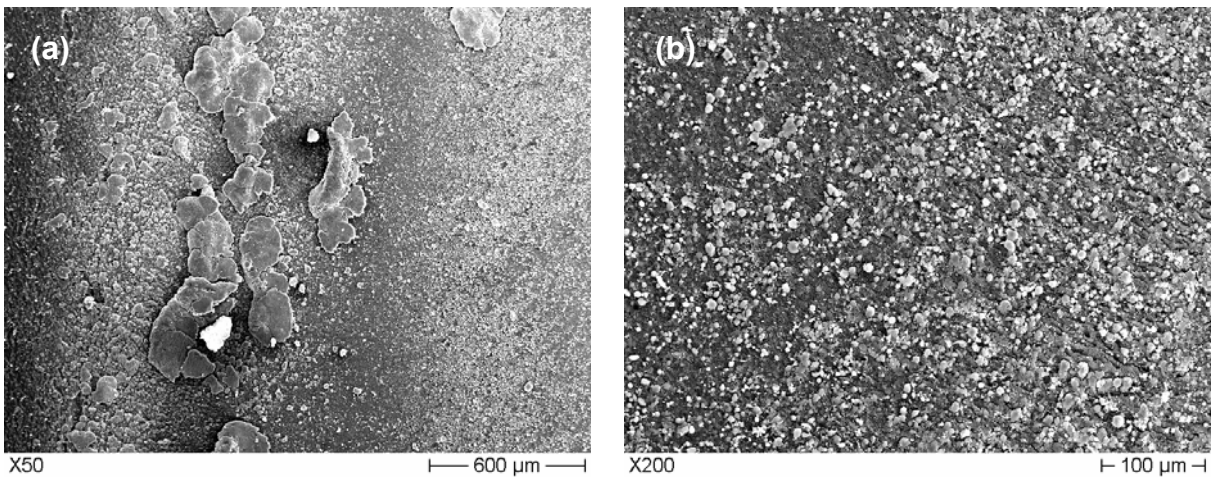

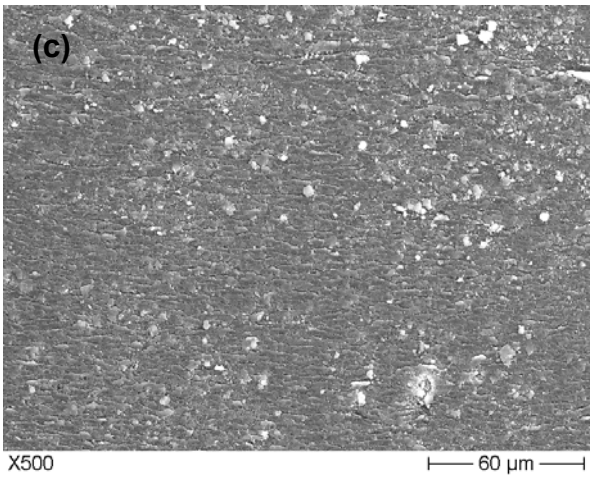

Figure 5.11 SEM photos taken from the rolling wear track of HNBR_30silica after Orbital-RBOP test. (a) outer region, (b) centre region, (c) inner region. Note: rolling direction is downward.

discernible (cf. Figure 5.10a). Fragmentation is the main wear mechanism in the centre region (cf. Figure 5.10b). “Ironed” particles and holes due to fatigue can be observed in the inner region of the worn surface (cf. Figure 5.10c). Note that the enlarged COF was possibly caused by the fragments and particles in the centre and inner region. With further increasing silica content (30 phr silica) the HNBR failed by formation of ironed spherical debris (cf. Figure 5.11). One can see that the particle size becomes finer when moving from the outer towards the inner part of the wear track. On the inner side of the wear track small and dense cracks perpendicular to the rolling direction can also be resolved (cf. Figure 5.11c). It is worth noting that incorporation of 20 or 30 phr silica inhibit the development of the Schallamach waves. This can be linked with the lower wear loss compared to pure or 10 phr reinforced HNBR.

When 10 phr MWCNT was added to the HNBR, the onset of Schallamach type waves and debris deposition are still characteristic for the outer side and for the middle regions, respectively, but no wave formation can be recognized in the inner side (cf. Figure 5.12). The W_s of HNBR_10MWCNT is slightly lower than that of plain HNBR. The surface of the inner side is produced by chipping. Figure 5.13 collects SEM photos taken from the three regions of the wear track of HNBR_20MWCNT. Fatigue induced spalling and fragmentation are the main wear mechanisms in the

outer and centre regions and accounts probably for the higher COF compared to plain HNBR (cf. Figures 5.13a and b). In the inner region flattened debris scatter over the whole area (cf. Figure 5.13c). At 30 phr MWCNT content on the outer and inner side small sized debris can be found on the surface (cf. Figures 5.14a and c). In the centre region dense waviness, offset to the rolling direction, can be resolved (cf. Figure 5.14b).

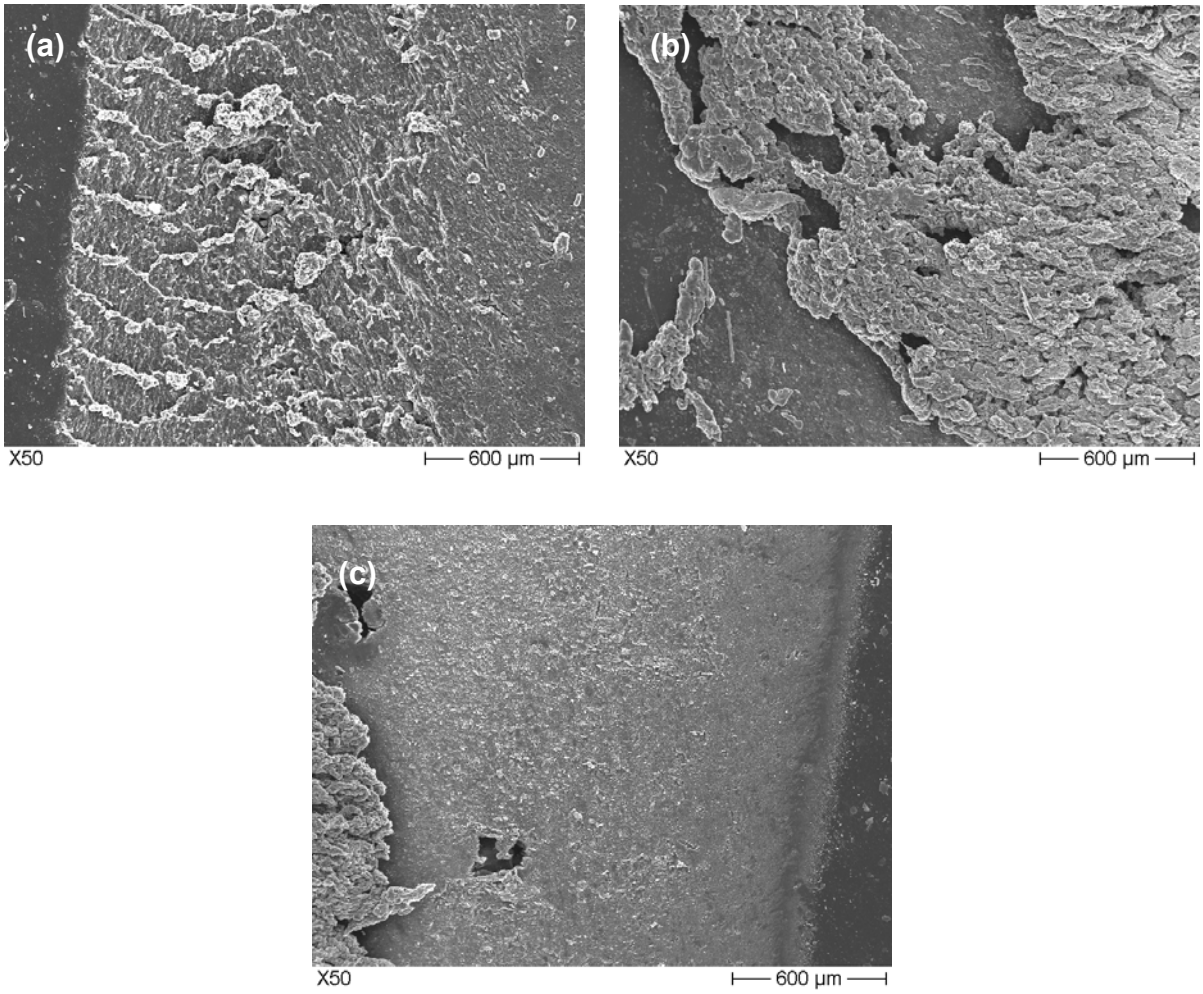

Figure 5.12 SEM photos taken from the rolling wear track of HNBR_10MWCNT after Orbital-RBOP test. (a) outer region, (b) centre region, (c) inner region. Note: rolling direction is downward.

It is noticeable that the wear loss of the filler reinforced HNBR system correlates with the occurrence of the Schallamach type pattern. The dramatically prohibited

waviness corresponds to the decreased W_s for both silica and MWCNT reinforcement. The introduction of active fillers (silica, MWCNT and CB in section 5.1.2.2) is the reason for the less developed or lacking waves, as often observed in rubbery systems with active fillers (e.g. Ref. 101-103). One may also observe that incorporation of 10 phr silica or MWCNT do not enhance the wear resistance prominently or even worsen it. However, when 20 phr fillers were added, the specific wear rate was strongly reduced. Interestingly, only very slight further decrease of W_s was found when the compounds contained more fillers.

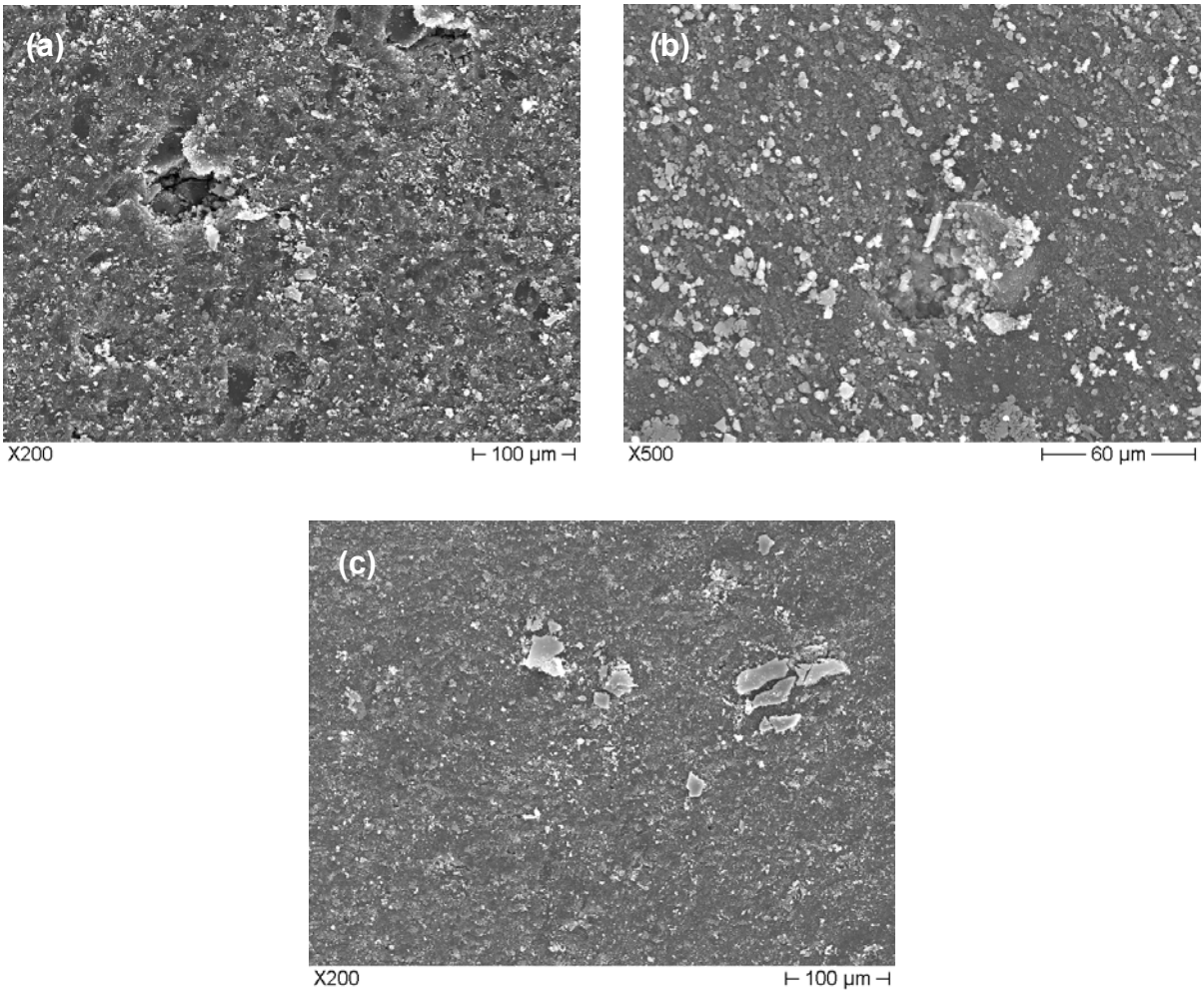

Figure 5.13 SEM photos taken from the rolling wear track of HNBR_20MWCNT after Orbital-RBOP test. (a) outer region, (b) centre region, (c) inner region. Note: rolling direction is downward.

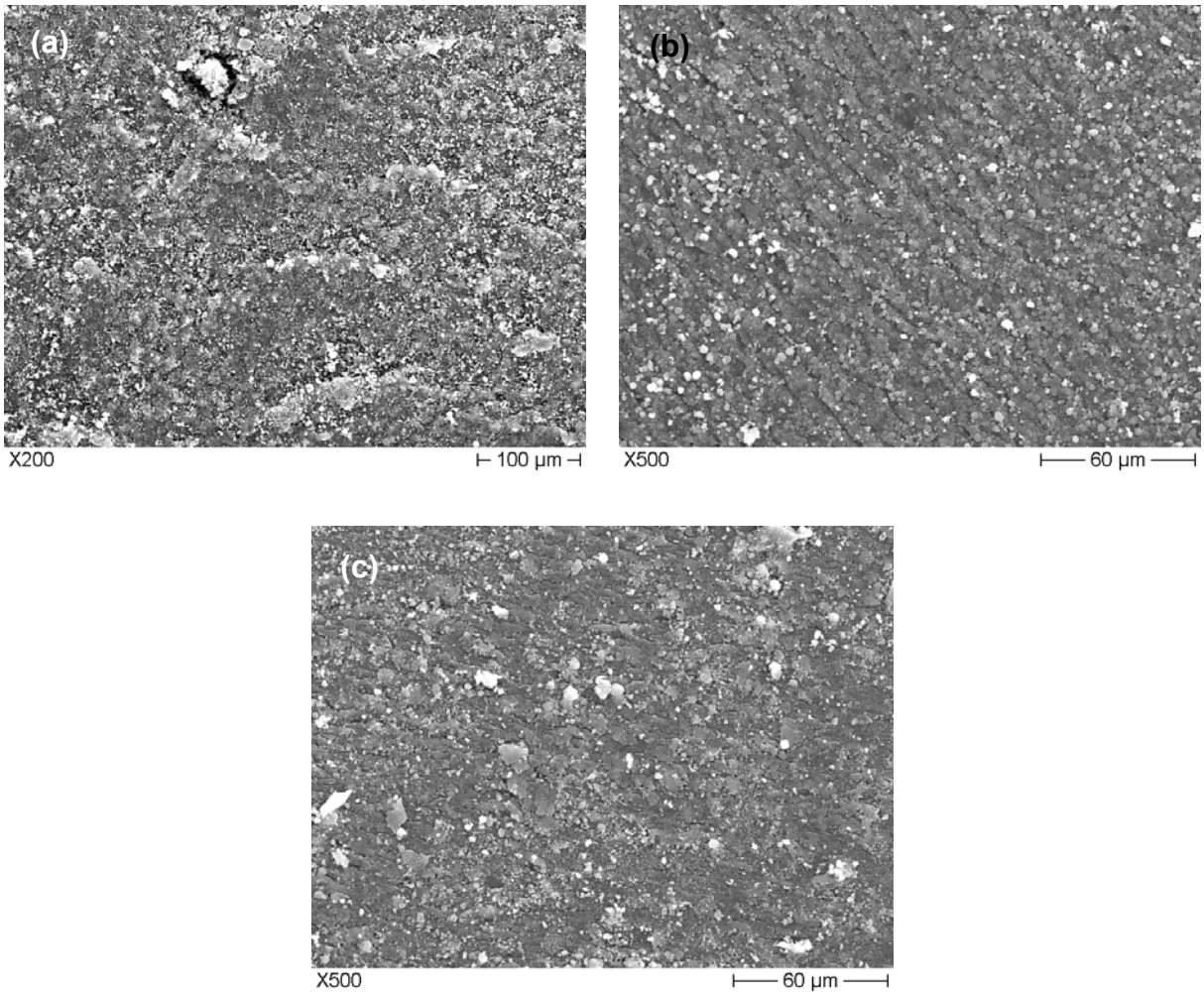

Figure 5.14 SEM photos taken from the rolling wear track of HNBR_30MWCNT after Orbital-RBOP test. (a) outer region, (b) centre region, (c) inner region. Note: rolling direction is downward.

5.1.2.2 HNBR_20CB/silica/MWCNT: effects of filler's type

5.1.2.2.1. Network-related properties and hardness

Figure 5.15 demonstrates the measured storage modulus (E') and loss factor (tan δ) as a function of the temperature (T= -100 to 100 °C). The position of the glass transition temperature of the HNBR composites (T_g ≈ -25 °C) was not affected either by the incorporation or the type of the fillers. One can see that introducing fillers in HNBR increased the stiffness in the rubbery stage of the composites. The MWCNT's effect was much stronger than that of CB and silica.

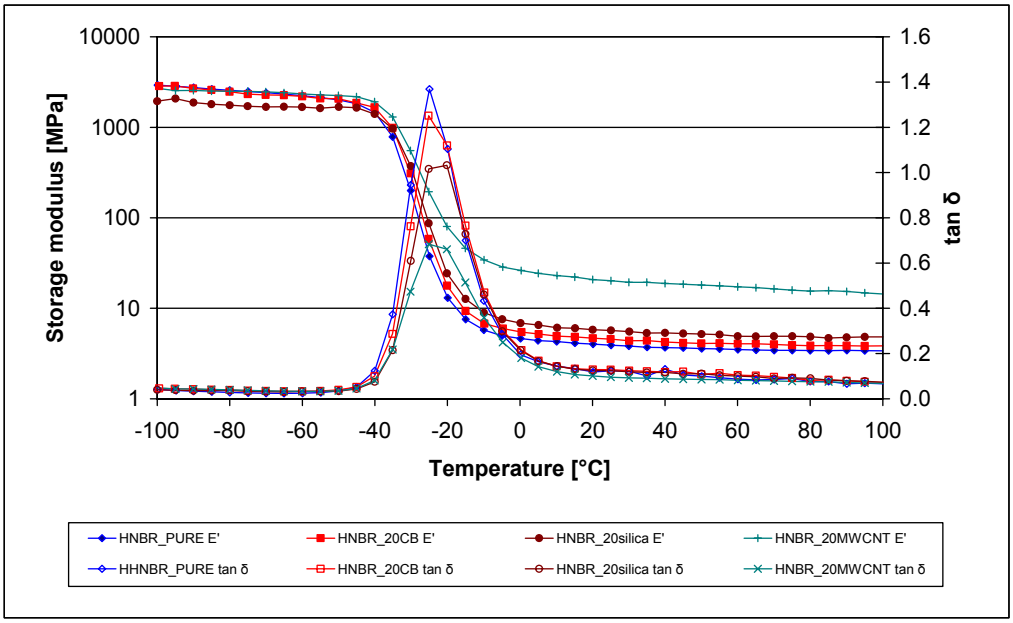

Figure 5.15 Storage modulus (E') and loss factor (tan δ) as a function of temperature for the HNBR_20CB/silica/MWCNT compounds.

The M_c and v_c values are listed in Table 5.3. It is noteworthy that HNBR_20MWCNT has the smallest M_c and accordingly the highest v_c. This reflects that MWCNT is the most efficient reinforcement having the strongest influence on the rubber-filler and filler-filler interactions among the fillers used.

The Martens hardness of HNBR_20MWCNT is the highest among all HNBR compounds studied. Note that the Martens hardness of CB and silica reinforced HNBR is close to that of pure HNBR. However from the Shore A hardness results [104], we can deduce that both the CB and silica were active reinforcement, however they had a weaker effect than MWCNT.

Table 5.3 Network-related properties and hardness of the HNBR_20CB/silica/MWCNT compounds.

	HNBR_PURE	HNBR_20CB	HNBR_20silica	HNBR_20MWCNT

M_c [g/mol]	2013	1775	1437	407
v_c [mol/m^3]	525	615	765	2710
tan δ at T_g	1.37	1.25	1.02	0.68
Density [g/cm^3]	1.057	1.091	1.099	1.102
Martens hardness [MPa]	1.02±0.56	0.66±0.29	1.02±0.20	3.37±0.71

5.1.2.2.2 Friction and wear

Figure 5.16 shows the COF and W_s of HNBR with and without fillers measured in Orbital-RBOP tests. Results in Figure 5.16 suggest that incorporation of CB, silica and MWCNT lowered the W_s and slightly enhanced the COF. CB proved to be better in improving the rolling wear resistance of HNBR compared to silica and MWCNT. Silica and MWCNT have similar effect in enhancing the rolling wear resistance of HNBR (cf. Figures 5.7 and 5.16).

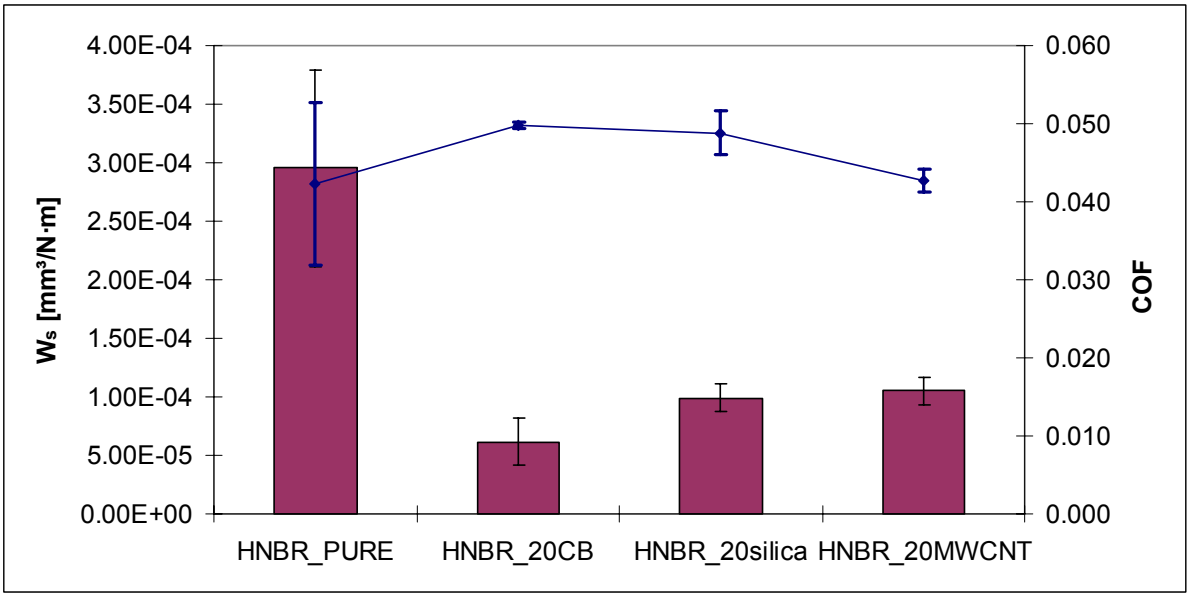

Figure 5.16 Changes of COF (line) and W_s (column) for HNBR_CB/silica/MWCNT in Orbital-RBOP tests as a function of fillers' type.

5.1.2.2.3 Wear mechanisms

The worn surface of HNBR_20CB after Orbital-RBOP test is shown in Figure 5.17. Large agglomerates, debris and fatigue induced holes can be found in the outer, centre and inner region of the wear track, respectively.

By reviewing Figures 5.8, 5.10, 5.13 and 5.17, like silica and MWCNT, the completely disappeared Schallamach-type pattern and the debris fragmented surface in the centre region of the wear track of HNBR_20CB result in a lower W_s and higher COF compared to the pure HNBR, respectively.

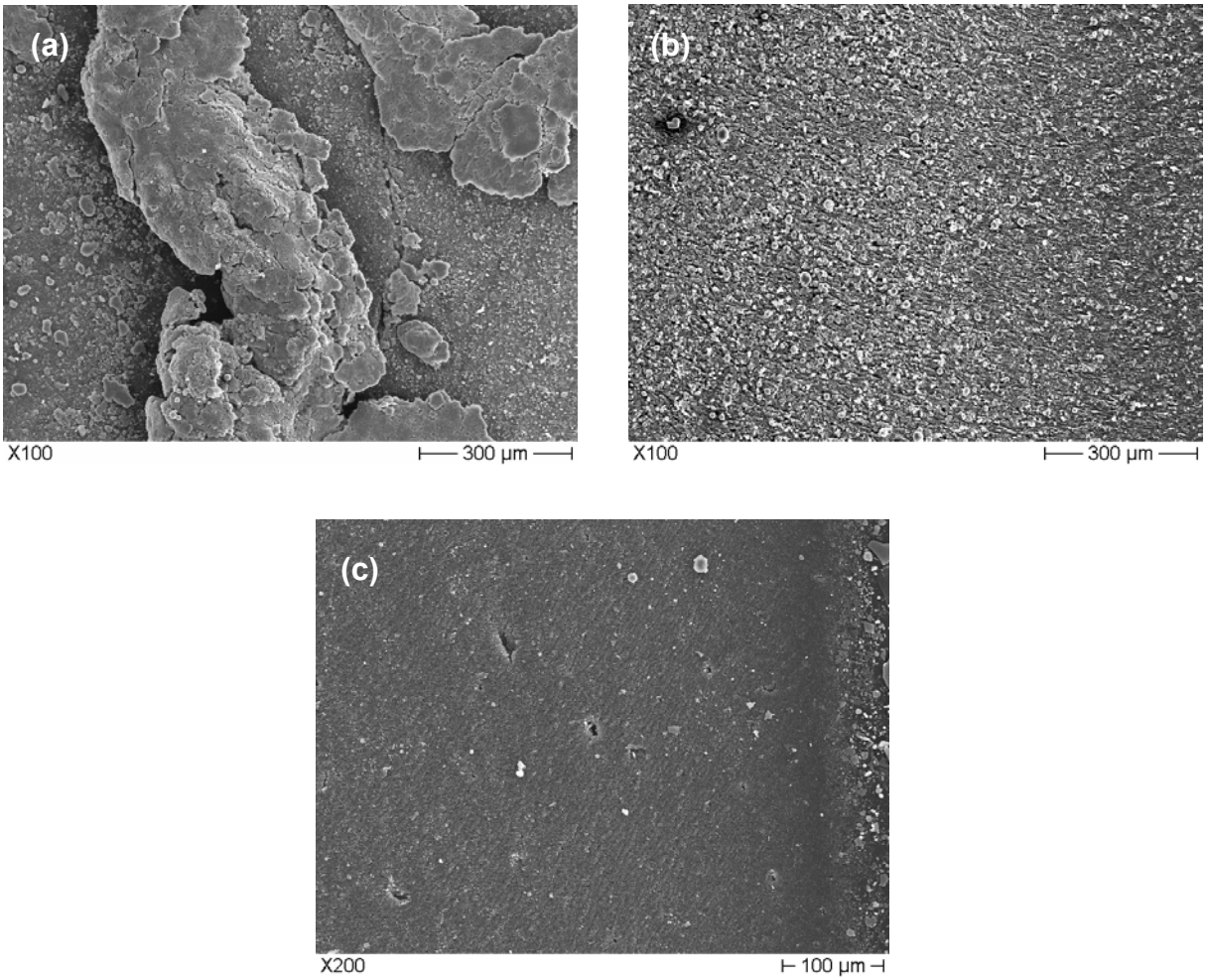

Figure 5.17 SEM photos taken from the rolling wear track of HNBR_20CB after Orbital-RBOP test. (a) outer region, (b) centre region, (c) inner region. Note: rolling direction is downward.

5.2 Elastomer/elastomer blend: HNBR-FKM_MWCNT

5.2.1 Effects of MWCNT

5.2.1.1 Phase structure

5.2.1.1.1 DMTA response

Figure 5.18 demonstrates the change of the storage modulus (E') and loss factor (tan δ) as a function of the temperature (T= -100 …100 °C) for HNBR-FKM 100-33.3, 100-33.3 MWCNT, 100-100, and 100-100 MWCNT. One can see clearly that incorporation of 10 phr MWCNT increased the stiffness of the related compounds. Even in case of the logarithmic plot of E' as a function of T, one can notice that the stiffness increases with decreasing temperature for all compounds. This kind of behavior can be traced to the presence of a more tightly crosslinked rubber.

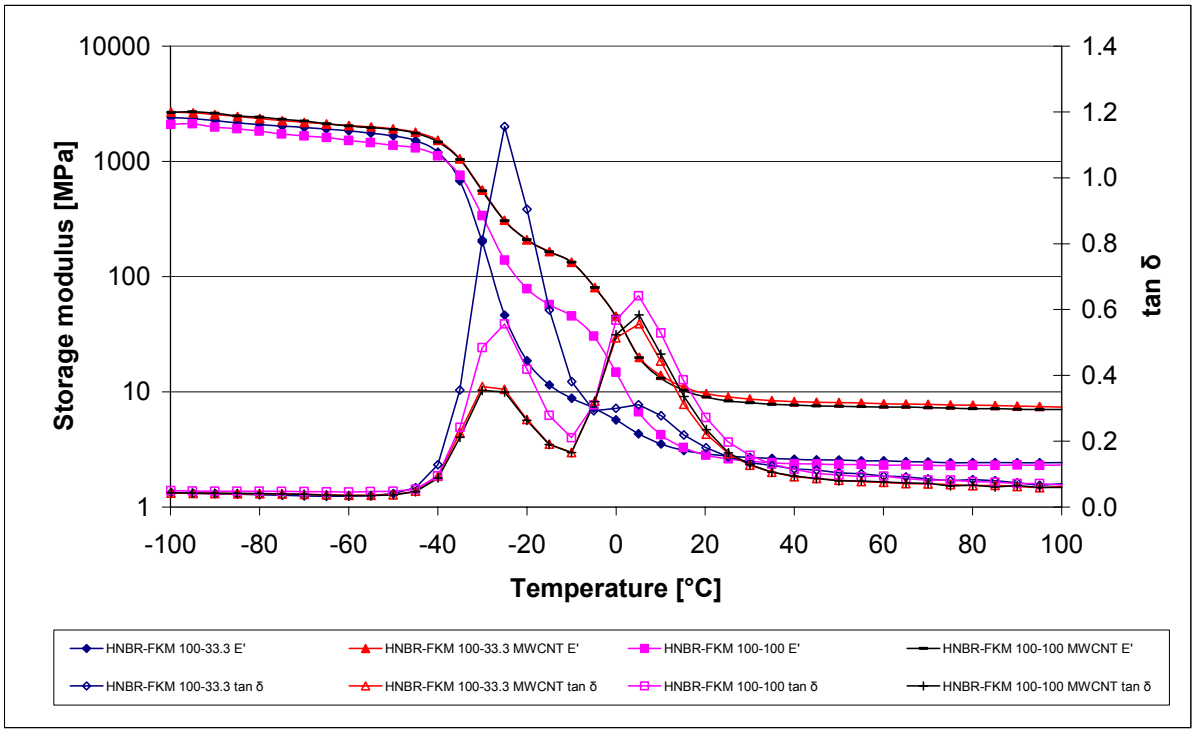

Figure 5.18 Storage modulus (E') and loss factor (tan δ) as a function of temperature for the HNBR-FKM_MWCNT hybrids.

The peaks in the tan δ vs T traces at -25 and +5 °C can be assigned to the glass transition temperatures (T_g) of the HNBR and FKM, respectively. Note that their position does not change with the MWCNT content. Accordingly, these HNBR-FKM mixes are two-phase systems. Based on the fact that the stiffness of the HNBR-FKM compounds drops at the T_g of the HNBR, one can surmise that the latter forms the matrix and FKM is present as dispersed phase within. A closer look at the tan δ vs T traces allows making a further hypothesis in respect to the phase structure. In contrast to the HNBR, the T_g relaxation transition of the FKM is not affected by the MWCNT. The strong reduction of the T_g peak of HNBR owing to MWCNT presence suggests that the MWCNT is located in the HNBR phase preferentially.

The network-related data are summarized in Table 5.4. One can recognize that M_c decreases and v_c increases dramatically when MWCNT is added to the related compound. Data in Table 5.4 indicate also that the incorporation of MWCNT enhanced the density and the Martens hardness.

Table 5.4 Network-related properties and hardness of the HNBR-FKM_MWCNT hybrids.

	HNBR_PURE	HNBR_10MWCNT	HNBR-FKM 100-33.3	HNBR-FKM 100-33.3 MWCNT	HNBR-FKM 100-100	HNBR-FKM 100-100 MWCNT
M_c [g/mol]	2013	1176	3088	1068	3715	1182
v_c [mol/m^3]	525	899	371	1213	352	1119
tan δ at T_g (at -25/+5 °C)	1.37	1.11	1.16/0.31	0.36/0.56	0.56/0.64	0.35/0.58
Density [g/cm³]	1.057	1.057	1.146	1.296	1.309	1.322

Martens hardness [MPa]	1.02±0.56	2.20±0.24	1.19±0.09	2.21±1.08	1.12±0.06	2.98±0.75
Contact angle [°]	≈102	≈99	≈95	≈90	≈98	≈90

5.2.1.1.2 TEM, AFM and contact angle results

TEM pictures taken from the HNBR-FKM 100-100 clearly show that the FKM is dispersed in the continuous HNBR phase (cf. Figure 5.19). The FKM is present in form of large micronscaled domains in the HNBR matrix. This phase structure does not change by incorporation of MWCNT (cf. Figure 5.20). Moreover, one can clearly recognize that MWCNT is preferentially embedded in the HNBR matrix. This finding is in line with the DMTA data and hardness results discussed before. The TEM pictures in Figure 5.20 also display that the MWCNTs are poorly dispersed, the nanotubes remained highly entangled in form of large agglomerates in the HNBR phase of the HNBR-FKM 100-100 mix. Nonetheless, MWCNT still may work as a useful tribological additive, as already demonstrated in the Ref. [29]. Comparing the high magnification AFM phase images taken from the HNBR-FKM 100-100 and HNBR-FKM 100-100 MWCNT, one can notice that the phase structure of the blend did not change by the introduction of MWCNT (cf. Figure 5.21). The dark domains in the related phase image in Figure 5.22 can clearly be assigned to MWCNT-rich agglomerates, which are dispersed in the HNBR phase. This assignment is supported by the TEM results. Recall that the size of the domains in Figure 5.22 agrees fairly with those which represent MWCNT agglomerates according to TEM images in Figure 5.20.

Results of the contact angle measurements show that incorporation of MWCNT resulted in decrease in the contact angles (cf. Table 5.4).

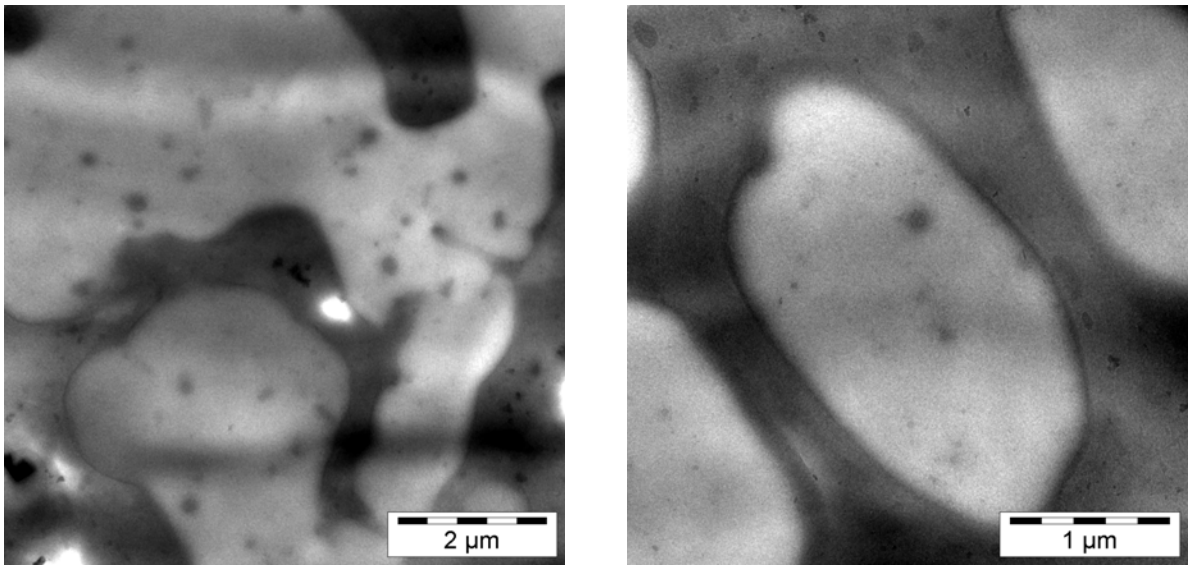

Figure 5.19 TEM pictures taken from the HNBR-FKM 100-100 compound.

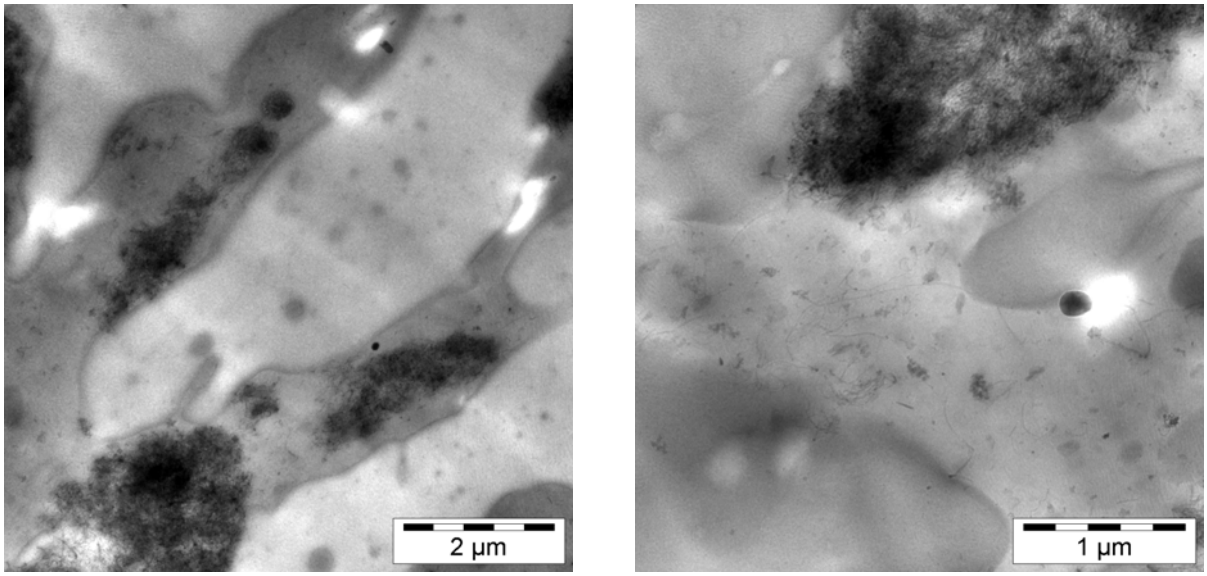

Figure 5.20 TEM pictures taken from the HNBR-FKM 100-100 MWCNT compound.

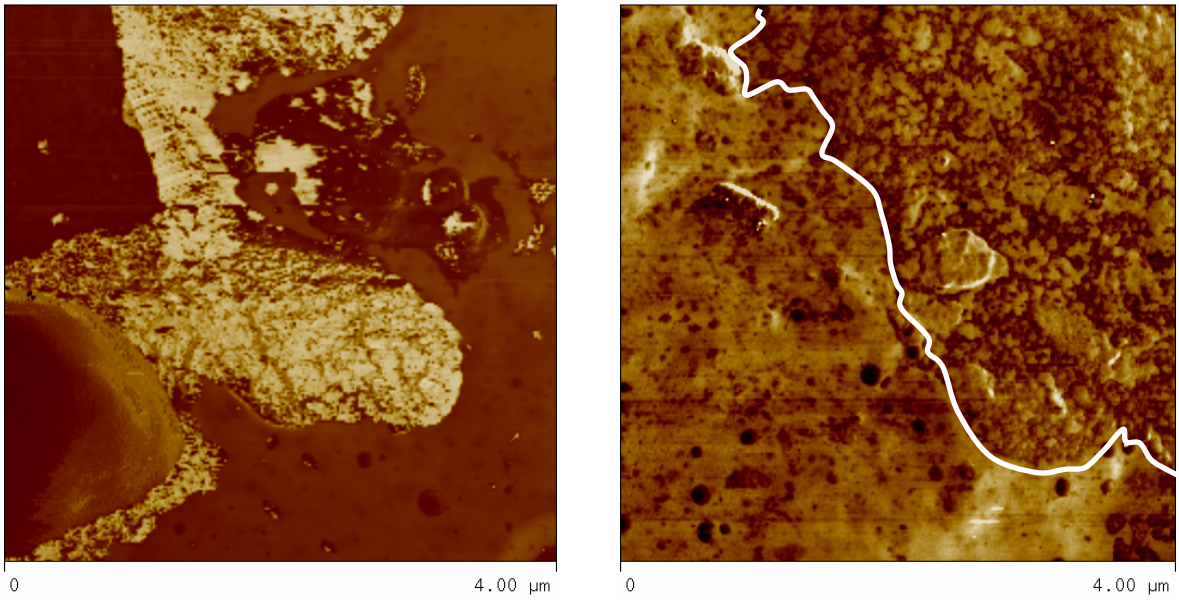

Figure 5.21 AFM phase images from the cryocut surface of HNBR-FKM 100-100 (left) and HNBR-FKM 100-100 MWCNT (right). Note: the bright phase in the sample HNBR-FKM 100-100 represents FKM. The white continuous line in the image of HNBR-FKM 100-100 MWCNT separates the HNBR (left-hand side) from that of the FKM (right-hand side). The former, i.e. HNBR, contains the agglomerated MWCNT.

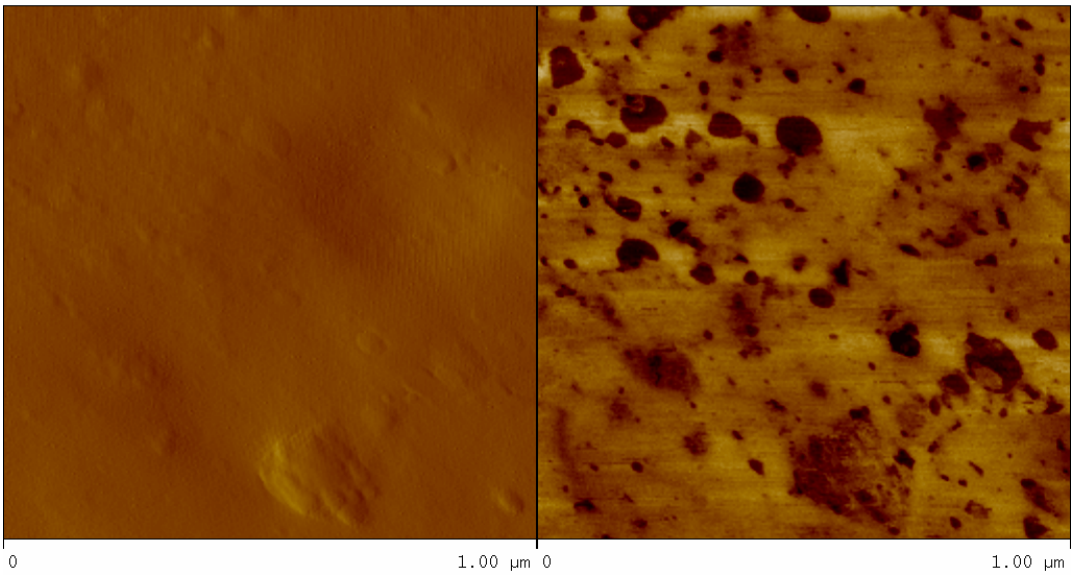

Figure 5.22 AFM amplitude (left) and phase images (right) from the cryocut surface of the HNBR-FKM 100-100 MWCNT showing MWCNT agglomerates in the HNBR phase.

5.2.1.2 Friction and wear

The COF and W_s of HNBR-FKM with and without MWCNT measured in Orbital-RBOP are summarized in Figure 5.23. Incorporation of MWCNT into HNBR-FKM increased the COF and decreased the W_s.

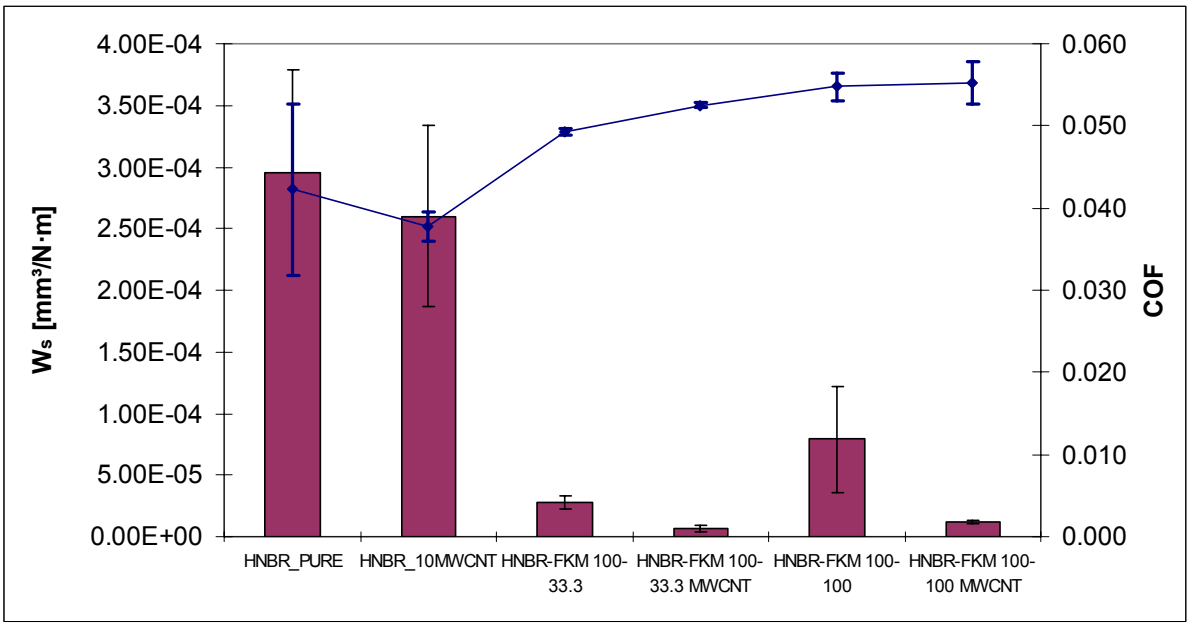

Figure 5.23 Changes of COF (line) and W_s (column) for HNBR-FKM_MWCNT in Orbital-RBOP tests.

5.2.1.3 Wear mechanisms

SEM photos taken from the rolling wear tracks of HNBR-FKM 100-33.3 with and without MWCNT after Orbital-RBOP tests are shown in Figure 5.24. In the outer region of HNBR-FKM 100-33.3, Schallamach type pattern appears with some fragments (cf. Figure 5.24a). Clusters from debris (agglomerates) were formed in the centre and inner regions (cf. Figure 5.24c). Incorporation of MWCNT changes the basic wear mechanisms in the outer region (cf. Figure 5.24b). Fatigued-induced formation of holes becomes the main wear mechanism instead of the Schallamach wavy pattern in HNBR-FKM 100-33.3. Hole development and debris clustering were found in the centre region of HNBR-FKM 100-33.3 MWCNT (cf. Figure 5.24b).

Fatigue-induced pittings and small “ironed” particles are seen in the inner region of the HNBR-FKM 100-33.3 MWCNT (cf. Figure 5.24d).

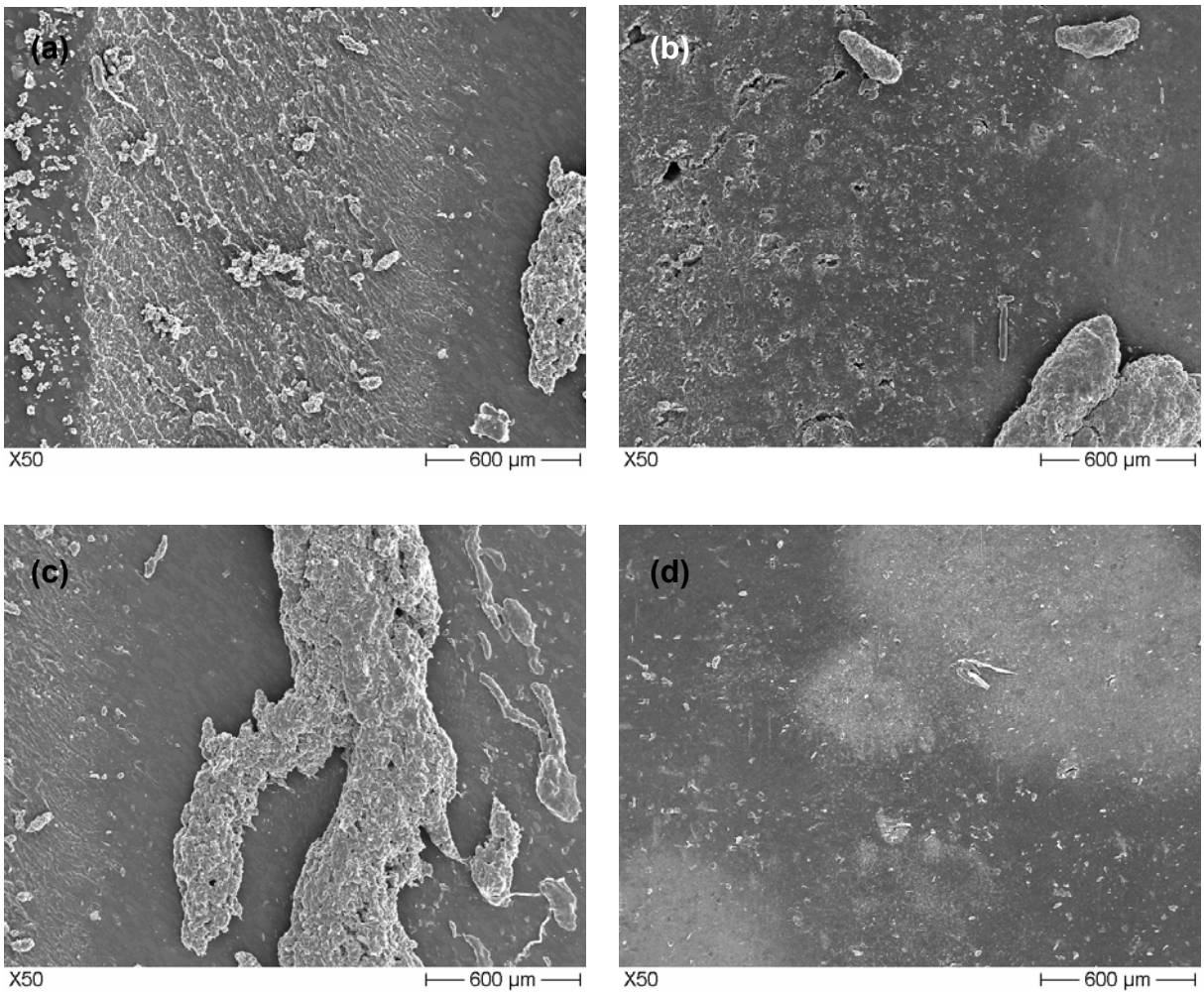

Figure 5.24 SEM photos taken from the rolling wear tracks of HNBR-FKM 100-33.3 without (a and c) and with (b and d) MWCNT after Orbital-RBOP tests. (a) outer region, (b) outer and centre regions, (c) centre and inner regions, (d) inner region. Note: rolling direction is downward.

The wear mechanisms for the HNBR-FKM 100-100 (MWCNT) did not change practically when compared to HNBR-FKM 100-33.3 (MWCNT) - cf. Figure 5.25. However, the inner region of HNBR-FKM 100-100 is full with “ironed” rolls, debris (cf. Figure 5.25c).

By comparing the worn surfaces of HNBR-FKM with and without MWCNT, we notice that the Schallamach wavy pattern disappears after MWCNT introduction. This change in the wear mechanism reflects a reduction in the specific wear rate, which was found also for other active fillers, e.g. CB, silica. It is worth noting that the Schallamach-type wear disappears with increasing reinforcement of a rubber independent of the type of the active filler used, which is in line with the finding in section 5.1.2.

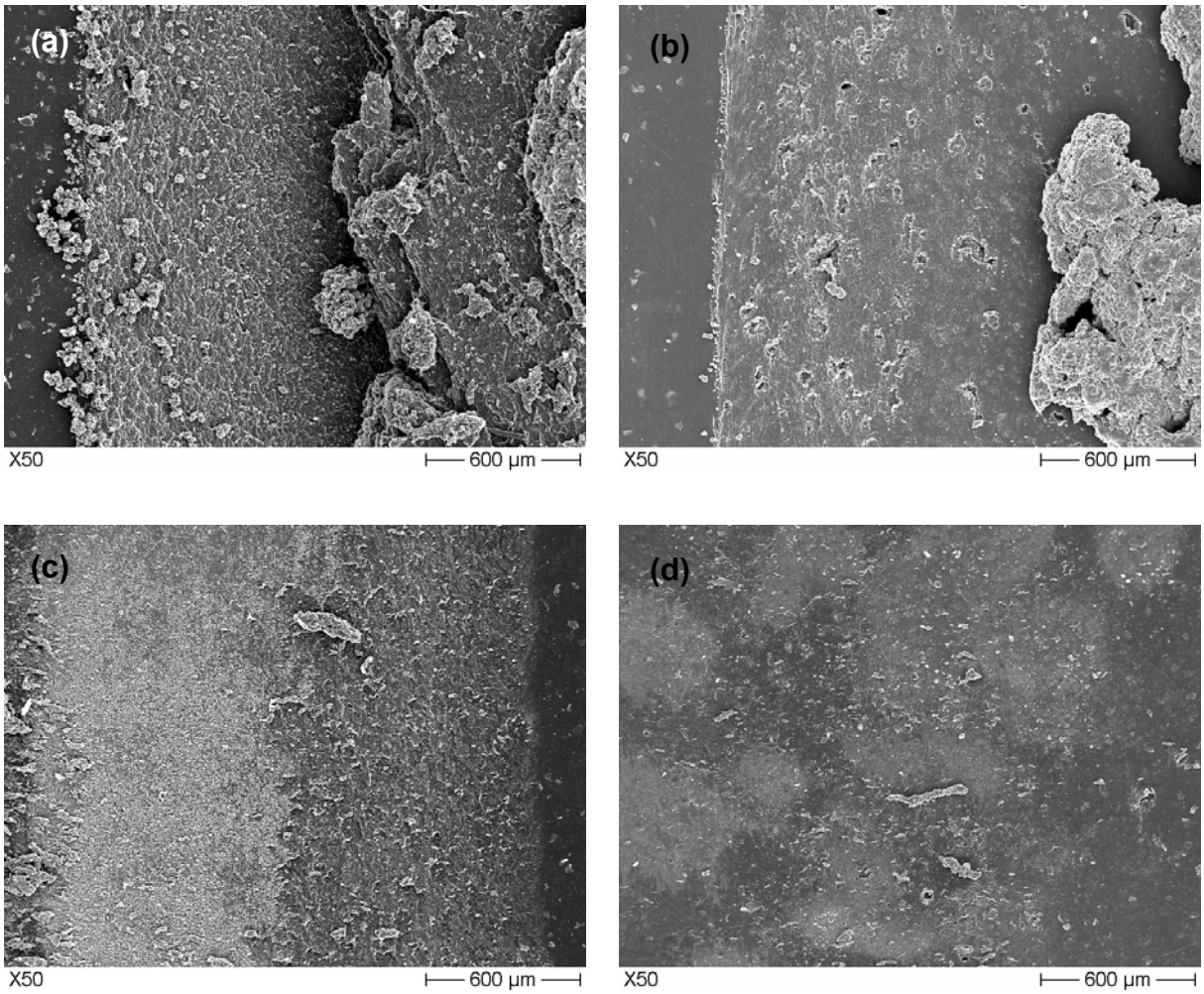

Figure 5.25 SEM photos taken from the rolling wear tracks of HNBR-FKM 100-100 without (a and c) and with (b and d) MWCNT after Orbital-RBOP tests. (a and b) outer and centre regions, (c and d) inner region. Note: rolling direction is downward.

5.2.2 Effects of FKM

5.2.2.1 Phase structure

5.2.2.1.1 DMTA response

The influence caused by the incorporation of FKM on the E' and tan δ of the HNBR-FKM blends is demonstrated in Figure 5.26. One can see clearly that incorporation of FKM reduced the stiffness of the related compounds over the both glassy and rubbery stages. The stiffness reduction owing to the introduction of FKM into HNBR may be linked with the curing. Note that the peroxide curing recipe was not adjusted for the HNBR-FKM mixes - so the content of the curatives has been for example halved for the HNBR-FKM 100-100. Further on, it was assumed that the curing processes of HNBR and FKM were running in parallel, which is likely not the case. Moreover, the interfacial adhesion between HNBR and FKM may be poor. However, the above aspects were not addressed in this work. The T_g of the HNBR and FKM at -25 and +5 °C, respectively, does not change with the HNBR/FKM composition.

The Table 5.4 demonstrates that adverse to MWCNT, blending with FKM increases M_c and decreases v_c. Again, this may be due to effects of the curing recipe (being "diluted" when adding FKM to the HNBR), difference in the cure rates between HNBR and FKM. Anyway, due to the presence of FKM in the HNBR the overall apparent crosslink density of the HNBR-FKM compounds is lower than that of the plain HNBR. However, the M_c value of HNBR-FKM 100-33.3 MWCNT is lower than HNBR_10MWCNT. This is likely linked with the higher density of MWCNT agglomerates in HNBR matrix compared to in HNBR_10MWCNT.

The density of the HNBR-FKM hybrids increases with the increasing FKM (cf. Table 5.4). The more FKM the blend contains, the softer the material is. It is interesting to note that the Martens hardness data of the MWCNT-containing HNBR-FKM compounds increases with FKM content. This can be explained by assuming that the MWCNT is predominantly present in the HNBR matrix.

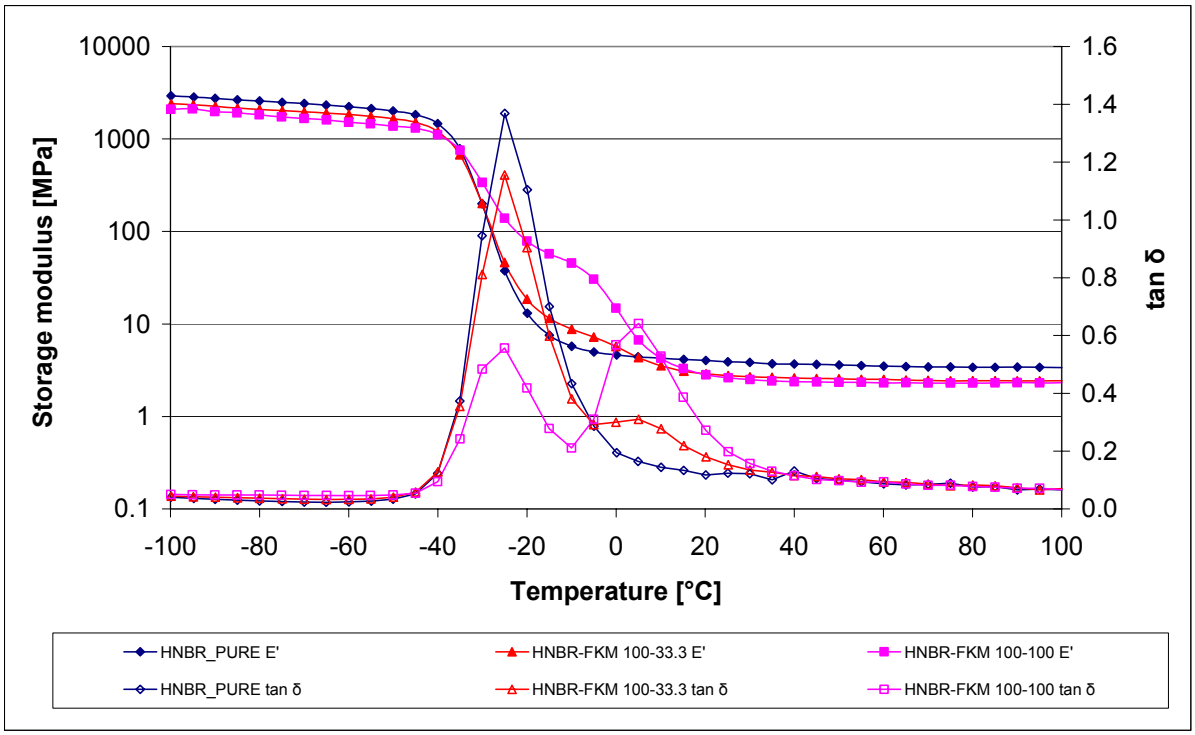

Figure 5.26 Storage modulus (E') and loss factor (tan δ) as a function of temperature for the HNBR-FKM hybrids.

5.2.2.1.2 Contact angle results

Incorporation of FKM into HNBR yielded some slight reduction in the contact angle (cf. Table 5.4). The contact angle data are similar to those published for HNBR [105] and some fluorinated latex systems [106]. Note that this finding, for which no simple explanation can be given at present, is against the expectation. Ikeda et al. [107] modified HNBR by copolymerization with fluorocontaining acrylates via peroxide crosslinking of the HNBR. The authors found that the surface tension of the HNBR was reduced by this way. This finding agreed with our working hypothesis, viz. HNBR blending with FKM would increase the contact angle which would reduce the adhesion component of friction, and finally reduce the COF. This was, however, not the case. The highly viscous FKM, being dispersed in the HNBR, did not enrich at the surface layer against the expectation.

5.2.2.2 Friction and wear

By comparing the COF and W_s of HNBR_PURE, HNBR-FKM 100-33.3 and HNBR-FKM 100-100 in Figure 5.23, it is obtained that the compounds of HNBR and FKM have higher COF and markedly lower W_s compared to HNBR_PURE. The more FKM the compound contains, the higher the COF is. This tendency in COF can be traced to the change observed for the contact angles (cf. Table 5.4). Increasing wettability, represented by smaller contact angles, should be accompanied with increased adhesion during friction and thus manifest in enhanced COF.

The specific wear rate does not show monotonous decrease with the increasing content of FKM. HNBR-FKM 100-33.3 has better rolling wear resistance than HNBR_PURE and HNBR-FKM 100-100. However, remember that HNBR and HNBR-FKM compounds are not directly comparable as the curatives became less and less with increasing FKM content. The comparison among HNBR_10MWCNT, HNBR-FKM 100-33.3 MWCNT and HNBR-FKM 100-100 MWCNT draws the same conclusions.

5.2.2.3 Wear mechanisms

The changes of the wear mechanisms caused by the introduction of FKM can be analyzed by reviewing Figures 5.8, 5.24 (a and c), 5.25 (a and c) or 5.12, 5.24 (b and d), 5.25 (b and d). Note that the worn surfaces of the pure and 10 phr MWCNT contained HNBR in the HNBR-filler series (cf. section 5.1.2) and HNBR-FKM series are quite similar even though small changes occurred to their production. The incorporation of FKM inhibits the formation of the Schallamach pattern. The space between the neighbouring waves and the height of the wave are reduced in the outer region and the Schallamach pattern disappears in the inner region in the HNBR-FKM system. No rolls are observed at the heads of the waves in HNBR-FKM. Recall that Schallamach waves with prominent roll formation were present in the inner region of the plain HNBR (cf. Figure 5.8). In the HNBR-FKM MWCNT compounds, no Schallamach wave appeared at all. However, as underlined earlier, HNBR and HNBR-FKM compounds can not be compared directly because the curatives became less and less with increasing FKM content. Nevertheless, this finding is quite unexpected as rubbers, when becoming “softer”, tend to fail by this kind of wavy pattern during unlubricated sliding and rolling wear tests (e.g. [101, 102]). One

possible reason behind this behaviour is a poor interfacial bonding between the HNBR and FKM phases.

Note that the dilution of the curing recipe can not be made responsible alone for the non monotonous changes in the friction and wear properties of the compounds with increasing content of FKM. Hirano et al. indicated in their research paper that several dynamical mechanical properties of HNBR-FKM (storage modulus, peak temperature of the loss modulus) did not follow the additivity rule in respect with the composition [36].

5.3 Elastomer/thermoplastic blend: HNBR-(p)CBT/pCBT

5.3.1 Effects of content and conversion of CBT

5.3.1.1 CBT conversion and phase structure

5.3.1.1.1 Extraction

Table 5.5 lists the results of the chloroform extraction of the hybrids. One can recognize that the CBT polymerized only in small amount during curing of the HNBR at T= 190 °C. On the other hand, the conversion of CBT to pCBT was high after annealing at T= 250 °C. Nonetheless, CBT did not polymerize completely even under the selected annealing process (cf. Table 5.5). Note that the conversion of a fully polymerized CBT is at about 97%.

Table 5.5 Density, CBT and pCBT content in the HNBR-(p)CBT/pCBT hybrids.

Designation, (Composition) HNBR-CBT	Initial CBT content [%]	Thermal treatment T [°C]	Density [g/cm³]	Chloroform extract [%]	Polymerized CBT, pCBT [%]
100-0	0	190	1.022	----------	----------
		250	1.017	----------	----------
100-50	30.4	190	1.098	28.1	7.6
		250	1.066	8.6	71.7
100-100	46.6	190	1.138	41.4	11.2

		250	1.132	4.9	89.5
100-150	56.7	190	1.161	53.9	4.9
		250	1.137	4.5	92.1

5.3.1.1.2 DSC

Figure 5.27 shows the DSC results for the heating (up 1 and up 2) and cooling (after up 1, down) of the HNBR-(p)CBT 100-100 and HNBR-pCBT system. One can notice the melting temperature of the unpolymerized CBT at T≈ 130 °C for the HNBR-(p)CBT 100-100 hybrid. On the other hand, for this system only limited melting can be observed in the range of T≈ 200-220 °C, which may be assigned to the pCBT. The fact that the CBT did polymerize during the first heating becomes obvious based on the cooling (crystallization of pCBT at T≈ 165 °C) and 2nd heating traces (well developed melting peak at T≈ 210 °C). This is in concert with earlier results [42]. Annealing at T= 250 °C changes the above scenario. The 1st heating curve of the HNBR-pCBT 100-100 exhibits a double melting peak at T≈ 220 °C representing the pCBT formed. During cooling the pCBT recrystallizes at T≈ 175 °C. This crystallization temperature is higher compared to that of the non-annealed sample. During subsequent heating (2nd heating) the pCBT shows a sharp melting peak at T≈ 220 °C in the HNBR-pCBT 100-100. One can notice that the melting of the pCBT occurs at higher temperature for the HNBR-pCBT than for the HNBR-(p)CBT during the 2nd heating. The shift in the melting temperatures toward higher values is linked with the presence of more perfect pCBT crystals.

For the HNBR-pCBT system (cf. Figure 5.27), the pCBT melting and crystallization peaks enlarge with increasing CBT content. The pCBT melting peaks at T≈ 200-220 °C in up 1 of all HNBR-pCBT blends prove that most CBT polymerized after annealing, which is in accord with the extraction data (cf. Table 5.5).

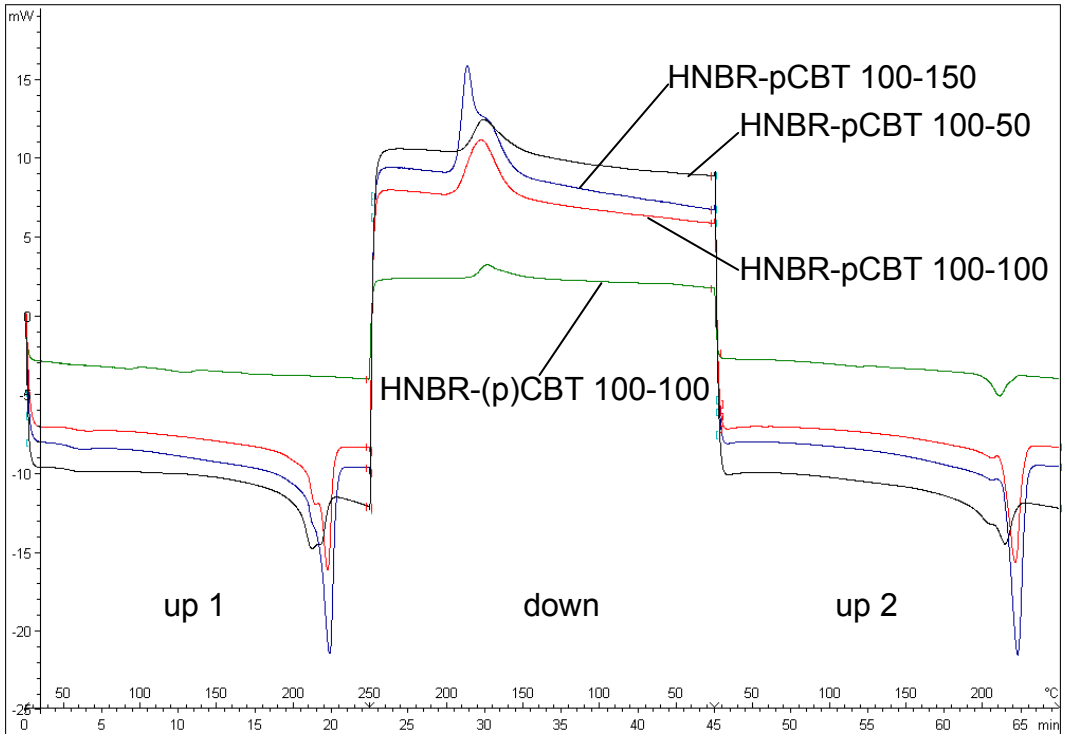

Figure 5.27 DSC traces recorded for the HNBR-(p)CBT 100-100 and HNBR-pCBT hybrids during heating (up 1 and up 2) and cooling (down).

5.3.1.1.3 DMTA

Figure 5.28 displays the storage modulus (E') and loss factor (tan δ) as a function of the temperature (T= -100 …240 °C). For both HNBR-(p)CBT and HNBR-pCBT hybrid systems, one can see that with increasing (p)CBT/pCBT amount the E' increases in a broad temperature range. HNBR has a glass transition (T_g) at T≈ -25 °C based on the related tan δ maximum (cf. Figure 5.28b). Annealing at T= 250 °C does not affect the T_g of the HNBR but slightly increases the E' values. The rubbery plateau is well developed for the plain HNBR. Based on the plateau modulus (E_{pl}, cf. Equation 2.7) at T= 25 °C, the calculated M_c values for the HNBR before and after annealing were ca. 3300 and 2850 g/mol. As a consequence, the corresponding v_c data are ca. 310 and 356 mol/m^3, respectively (cf. Equations 2.7 and 2.8). Annealing (= postcuring) of HNBR thus resulted in a better crosslinked structure, as expected.

The course of the E' vs. T traces of the HNBR-(p)CBT series differs markedly from that of the HNBR-pCBT. The E' of the former hybrids steeply decreases with the

temperature above the T_g of the HNBR. One can notice a crossover with the plateau modulus of the HNBR at T≈ 140 °C. Recall that this is matched with the melting temperature of the unpolymerized CBT. Therefore, already the DMTA results corroborate that the CBT remained mostly unpolymerized in the HNBR-(p)CBT hybrids.

The scenario is completely different for the annealed, i.e. HNBR-pCBT hybrids. Above the T_g of the HNBR the reduction in E' is much smaller for the annealed than for the parent hybrids. A drop in the E' vs. T traces can be observed only close to the melting temperature of pCBT. Between the T_g of the HNBR and melting temperature of the pCBT, the storage modulus decreases marginally with increasing temperature. This plateau-like course of E' as a function of temperature in this range suggests that the pCBT forms also a continuous phase (appearance of dual phase continuity). Note that the tan δ vs. T traces in Figure 5.28b also support the presence of this phase structure. Accordingly in the related hybrids both HNBR and pCBT phases are likely continuous. This structure should be termed to semi-interpenetrating network (semi-IPN) as the HNBR is crosslinked whereas the pCBT not. The onset of this semi-IPN due to the annealing process is topic of ongoing investigations. AFM inspection supported the presence of this semi-IPN structure (see section 5.3.1.1.5). Comparing the DMTA spectra of the hybrids before and after annealing the question arises: why the reinforcing effect of (p)CBT just after the T_g of rubber is higher than pCBT. This reinforcing effect is most likely due to formation of large crystals which have good interfacial bonding to the HNBR matrix in the HNBR-(p)CBT hybrids [42].

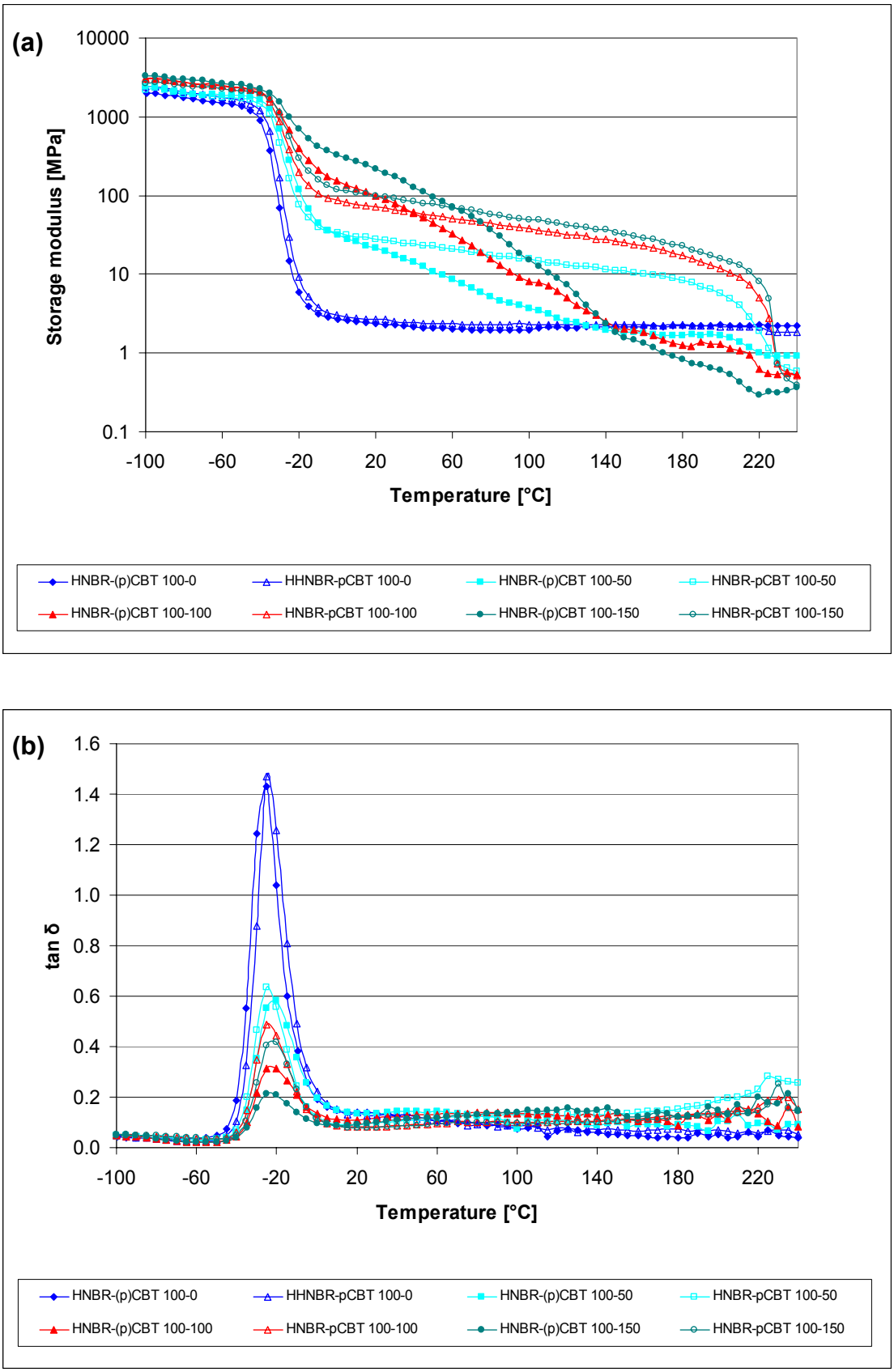

Figure 5.28 Storage modulus (E') (a) and loss factor (tan δ) (b) as a function of the temperature for the HNBR-(p)CBT (full symbols) and HNBR-pCBT (empty symbols) hybrids.

5.3.1.1.4 WAXS

Figure 5.29a displays the WAXS spectra of the CBT® 160 powder (CBT 160p) and HNBR-(p)CBT 100-100. One can clearly recognize that both spectra are very similar. This means that the CBT in HNBR-(p)CBT remained practically unpolymerized. The appearance of some new peaks is likely due to the presence of crystalline additives in the HNBR recipe. This speculation is supported by the WAXS spectrum of HNBR-pCBT 100-0 in Figure 5.29b. In order to evidence that pCBT did form, the related spectrum taken from a conventional PBT (Ultradur B4520 of BASF, Ludwigshafen, Germany) was inserted in Figure 5.29b, too. Matching position of the related peaks between PBT reference and HNBR-pCBT 100-100 confirms that pCBT has been formed due to annealing, in fact.

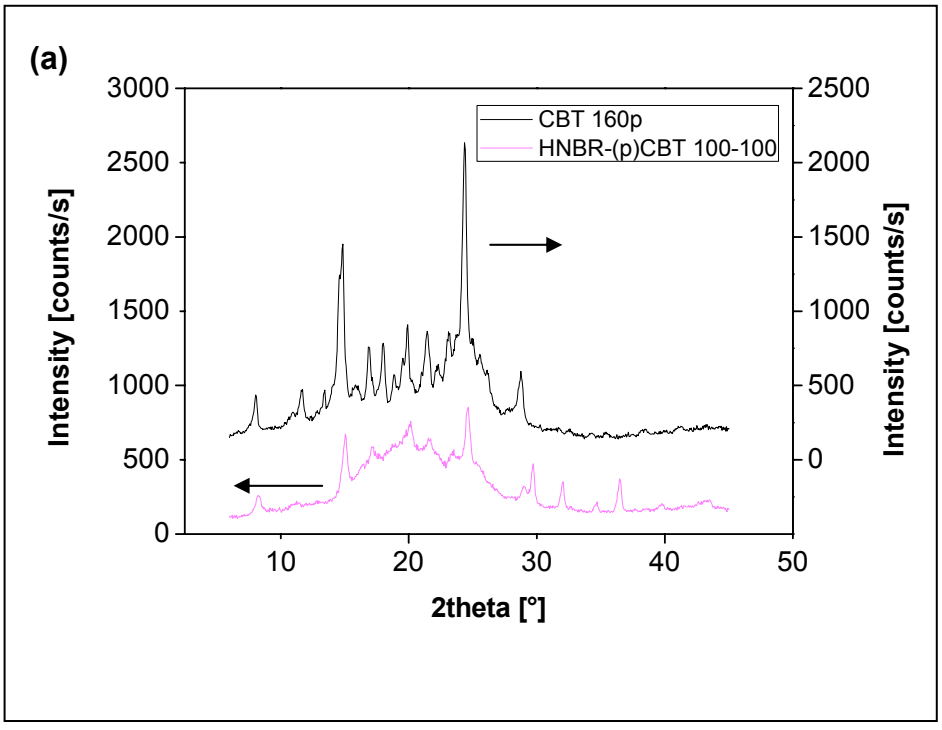

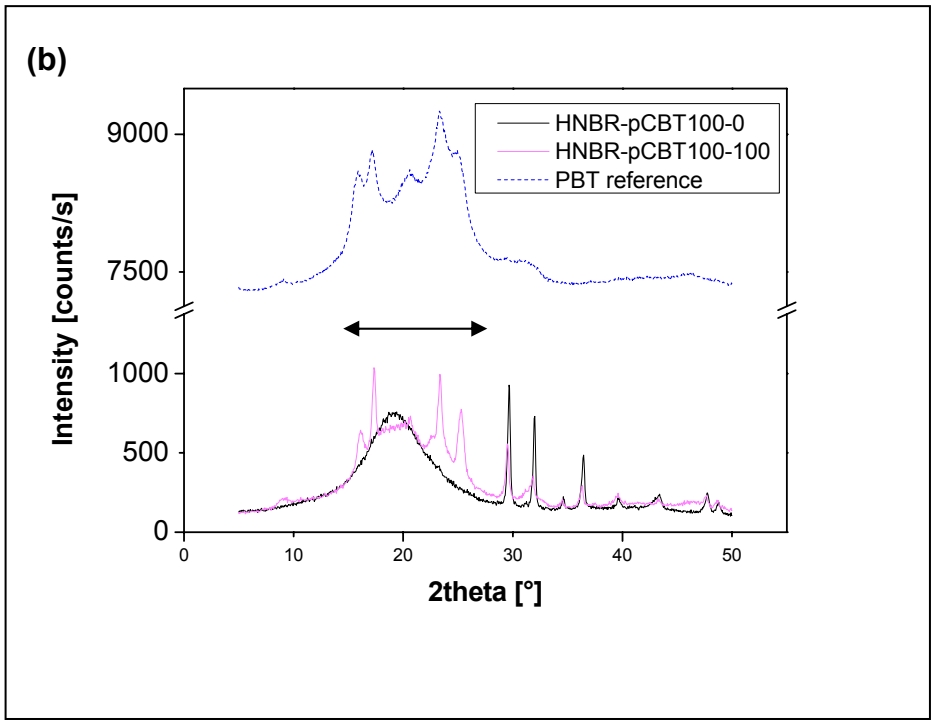

Figure 5.29 WAXS curves of CBT 160p, HNBR-(p)CBT 100-100 (a) and HNBR-pCBT 100-0 and 100-100, PBT reference (b). Note: the range with characteristic PBT peaks is indicated by arrowed line.

5.3.1.1.5 AFM

Figure 5.30 provides a strong visual proof that the CBT crystals exist in HNBR-(p)CBT 100-100. Recall that they were formed within the HNBR when the sheets were cooled from the curing to ambient temperature. Under the cooling condition, large disk- and prism-like CBT crystals developed via recrystallization from the melt. This AFM observation is in line with results from inspecting the worn surfaces of the hybrids (see later in section 5.3.1.2).

The AFM images in Figure 5.31 were taken from the cryofractured surface of HBR-pCBT 100-100. The AFM phase image in Figure 5.31b especially supports the fact that the pCBT phase is quasi-continuous, indeed. This finding corroborates that the earlier interpretation of the DMTA curves was correct.

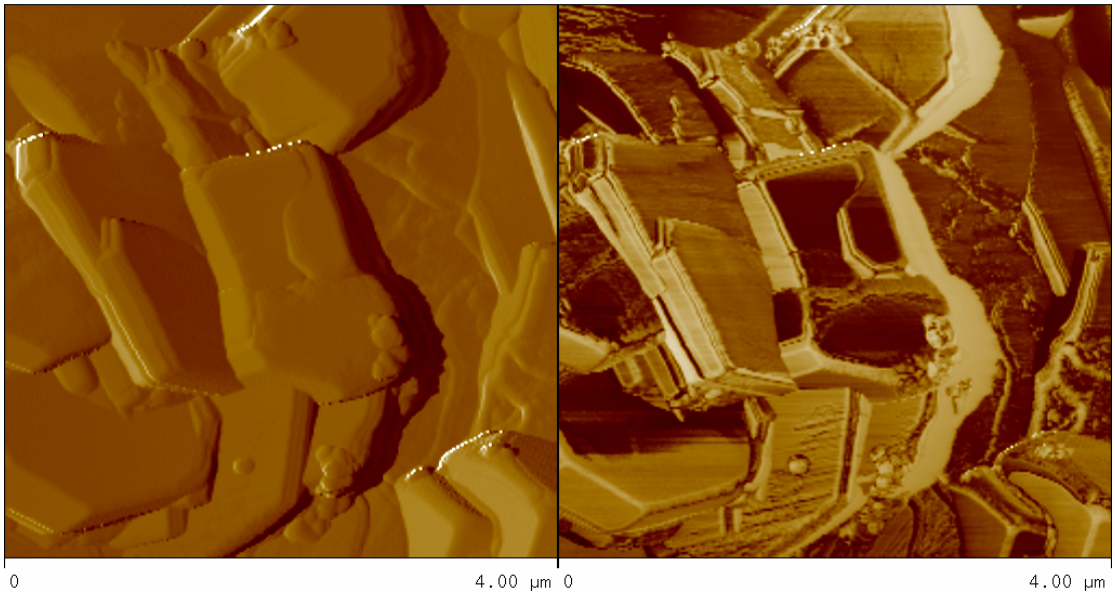

Figure 5.30 AFM amplitude (left) and phase (right) images taken from the cryofractured surface of HNBR-(p)CBT 100-100.

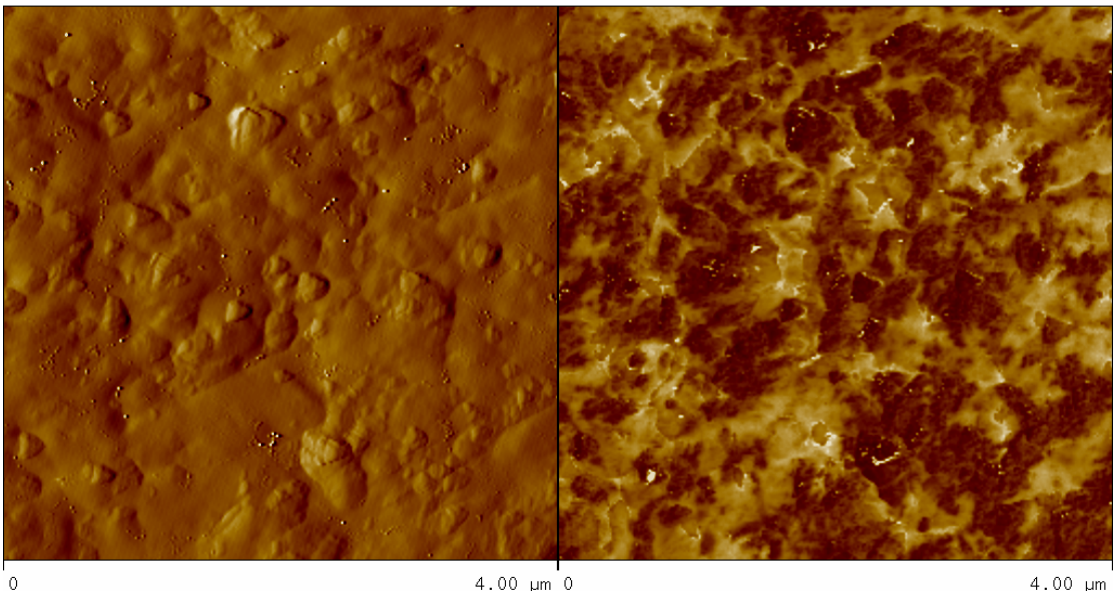

Figure 5.31 AFM amplitude (left) and phase (right) images taken from the cryofractured surface of HNBR-pCBT 100-100. Note: the dark and bright coloured phases are assigned to the pCBT and HNBR, respectively.

5.3.1.2 Friction and wear

Figure 5.32 shows the COF and W_s of HNBR-(p)CBT and HNBR-pCBT hybrids measured in Orbital-RBOP tests. One can get the impression that the compounds of HNBR and (p)CBT have higher COF and slightly lower specific wear rate values than plain HNBR. The more (p)CBT the compound contains, the lower the COF and W_s are. The maximum in the COF at the HNBR-(p)CBT 100-50 likely reflects a less homogenous dispersion of the CBT crystals compared to those hybrids which contained more (p)CBT. In presence of 100 and 150 phr pCBT in the HNBR-pCBT hybrids both the COF and W_s are smaller than those of the neat HNBR. Like to the HNBR-(p)CBT series, the COF of HNBR-pCBT passes a small maximum as a function of the pCBT content at 50 phr. This may be again linked with the dispersion state of the pCBT. The smaller COF and W_s values of the HNBR-pCBT compared to of HNBR-(p)CBT suggest that the polymerized CBT has a more beneficial affect on the rolling wear properties than the unpolymerized one (i.e. (p)CBT).

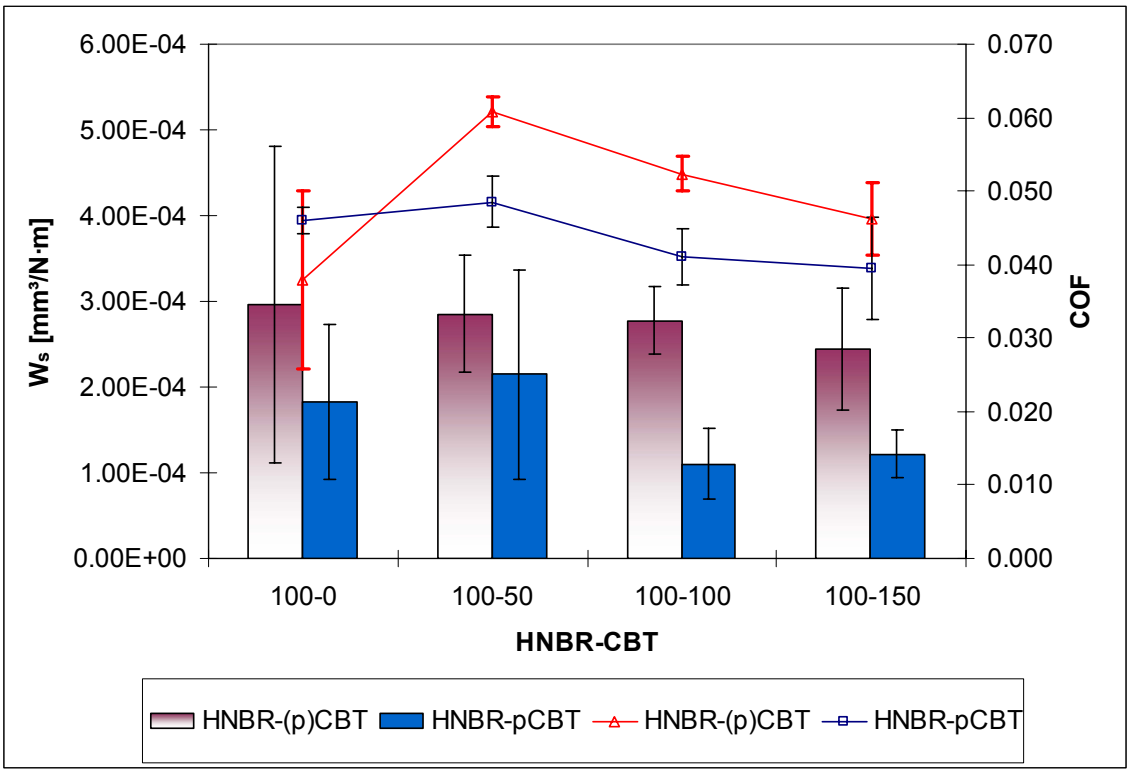

Figure 5.32 Changes of COF (line) and W_s (column) for HNBR-(p)CBT/pCBT hybrids in Orbital-RBOP tests.

5.3.1.3 Wear mechanisms

Figure 5.33 shows SEM photos taken from the rolling wear track of HNBR-(p)CBT 100-0. In the outer and inner regions, Schallamach-type pattern can be seen. The wave fronts with roll heads are more or less transverse to the rolling direction (cf. Figures 5.33a and c). This wavy pattern is, however, different in the inner and outer regions. The fronts of the waves in these two regions are adversely oriented, caused by the opposite direction of the ball movement in the two regions (cf. section 2.3.1.3.2, Figure 2.8). In the centre region very large agglomerates are present (cf. right and left handed sides of Figure 5.33b). By reviewing the wear mechanisms of

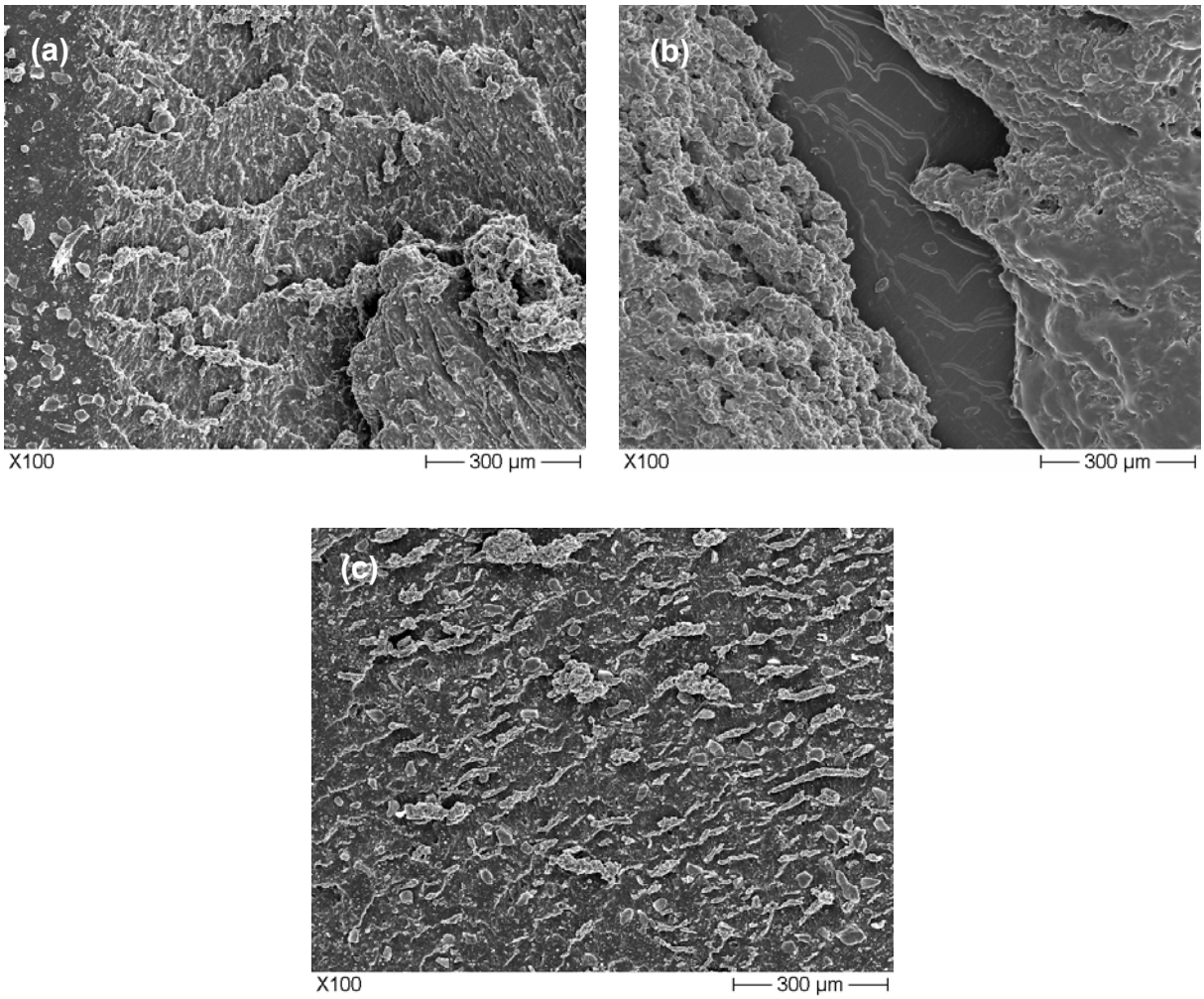

Figure 5.33 SEM photos taken from the rolling wear track of HNBR-(p)CBT 100-0 after Orbital-RBOP test. (a) outer region, (b) centre region, (c) inner region. Note: rolling direction is downward.

the pure HNBR cured at T= 175 °C for 15 min (cf. Figure 5.8, section 5.1.2.1.3), one can get the impression that changes in the temperature and pressing time did not affect the wear mechanisms in HNBR.

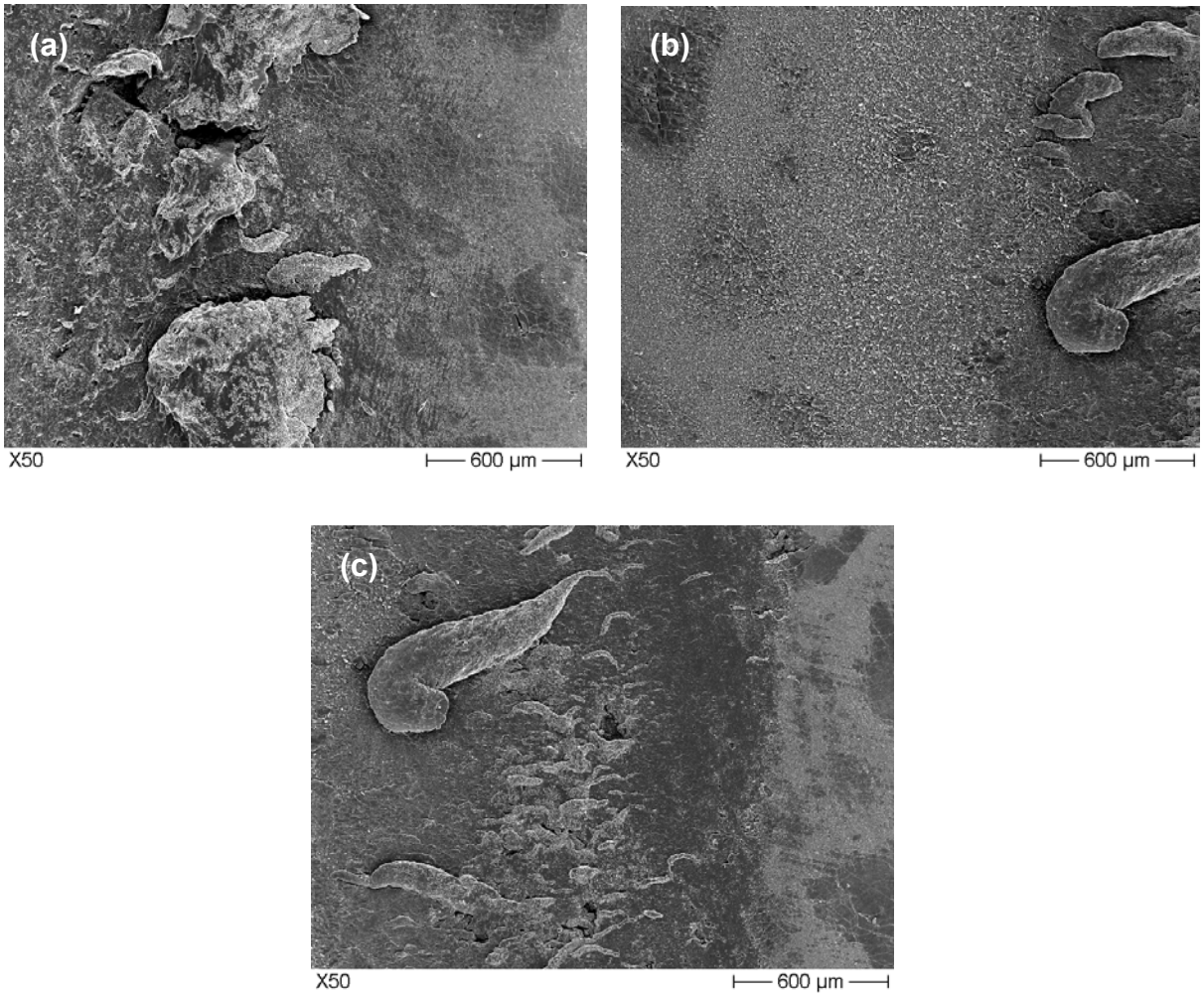

Figure 5.34 SEM photos taken from the rolling wear track of HNBR-(p)CBT 100-100 after Orbital-RBOP test. (a) outer region, (b) centre region, (c) inner region. Note: rolling direction is downward.

SEM photos taken from the rolling wear track of HNBR-(p)CBT 100-100 after Orbital-RBOP test are shown in Figure 5.34. The Schallamach-type pattern in the outer region disappeared completely (cf. Figure 5.34a). Apparently, the introduction of (p)CBT inhibits the formation of the Schallamach pattern. Note that this is usually caused by increasing amount of active fillers making the rubber harder and harder

[102, 103 and 108]. Large cracks, fragments are well discernible in the outer region (cf. Figure 5.34a). Dense fatigue-induced surface cracking, however, without prominent crack opening can be observed in the centre region (cf. Figure 5.34b). Crack opening associated with hole development and roll formation are representative wear mechanisms in the inner region (cf. Figure 5.34c).

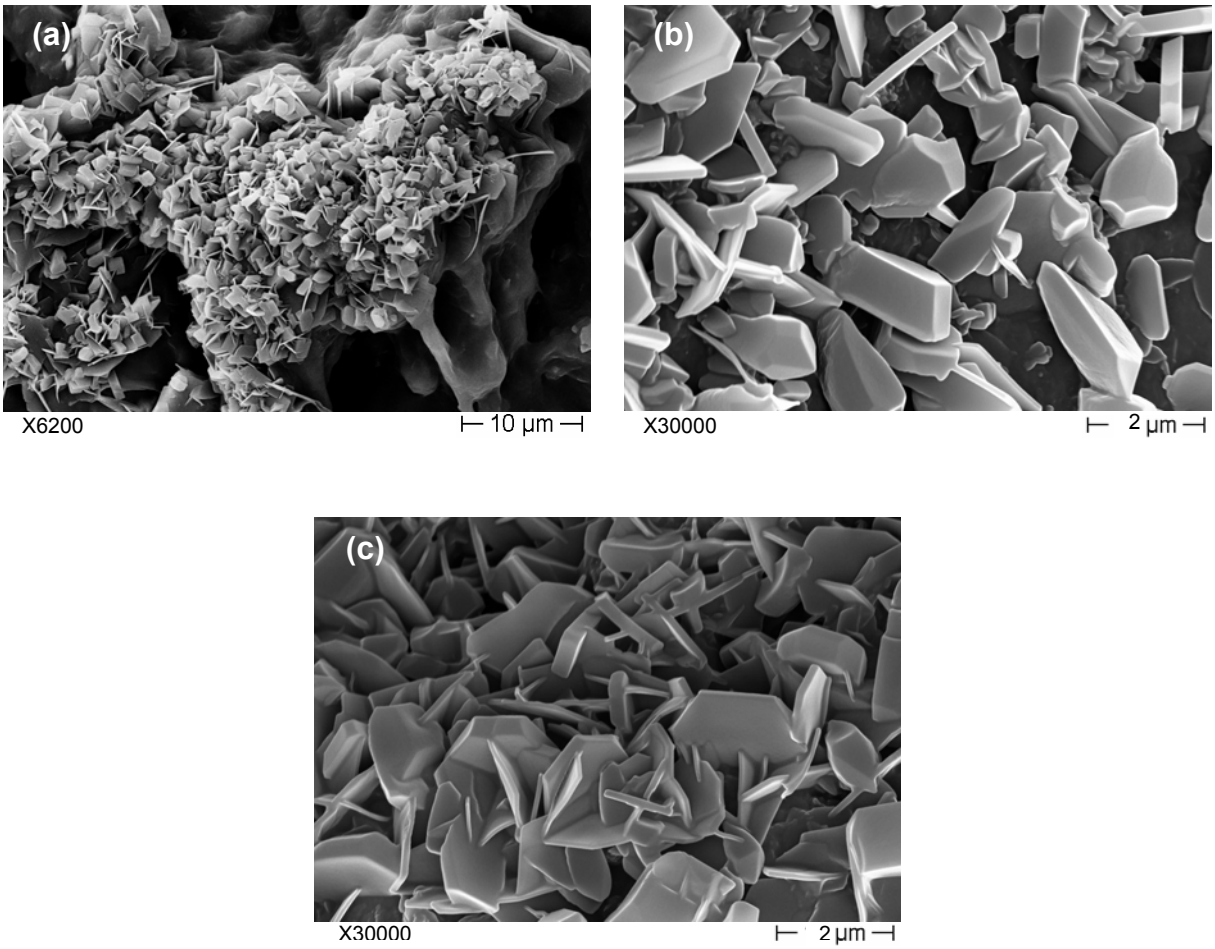

Figure 5.35 High magnification SEM photos taken from the wear tracks of HNBR-(p)CBT (a) 100-50, (b) 100-100, (c) 100-150, respectively.

In the worn surfaces of HNBR-(p)CBT hybrids, many disk- and prism-like particles are observed (cf. Figure 5.35). They have the same dimension as the crystals shown in Figure 5.30. Accordingly, they are well developed CBT crystals. The existence of such crystals and their dispersion in the HNBR matrix in the HNBR-(p)CBT hybrids may be the main reason for the higher COF compared to HNBR-pCBT series. Note

that the similar crystals were also found in the worn surfaces of HNBR-(p)CBT after sliding wear tests [42].

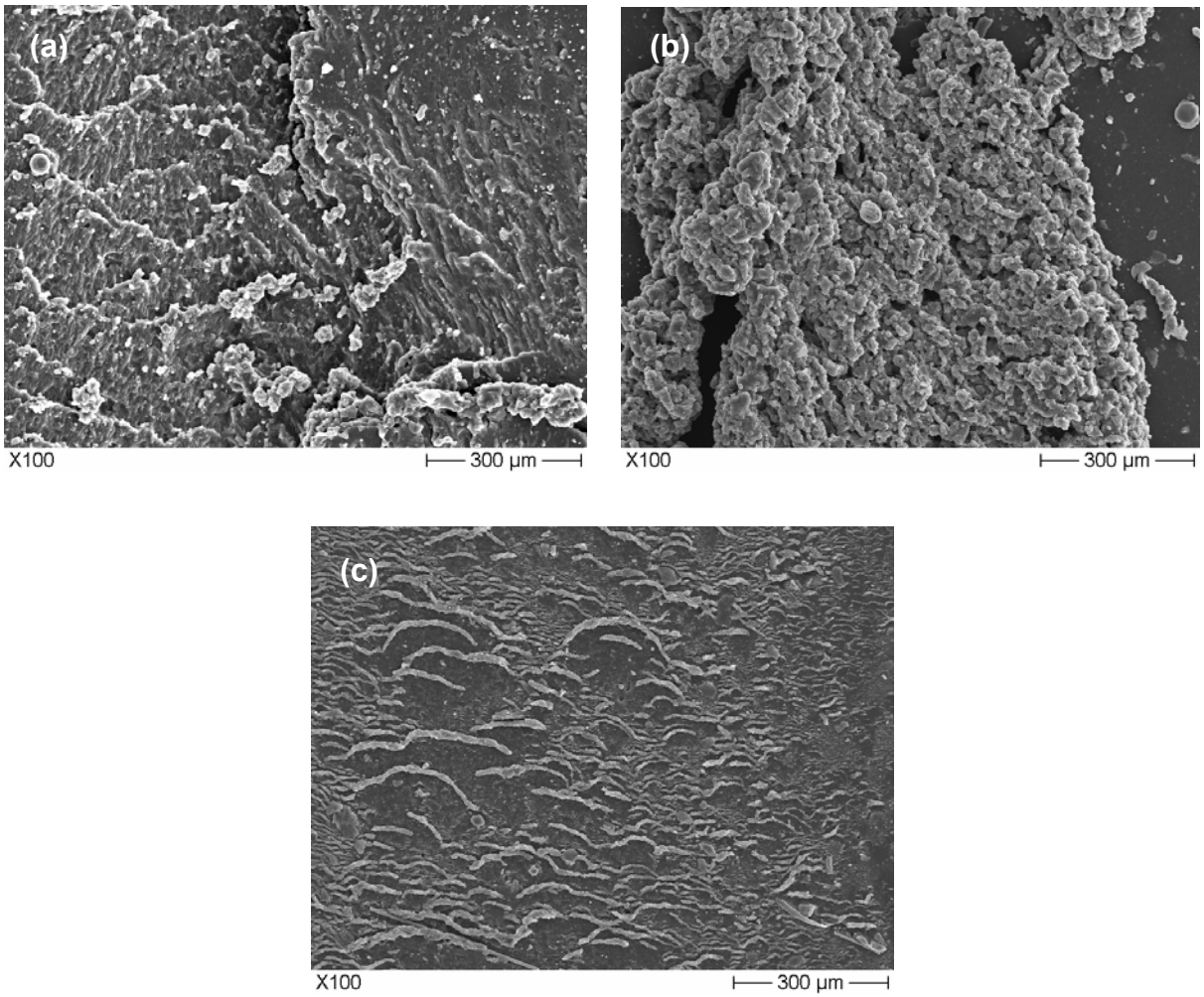

Figure 5.36 SEM photos taken from the rolling wear track of HNBR-pCBT 100-0 after Orbital-RBOP test. (a) outer region, (b) centre region, (c) inner region. Note: rolling direction is downward.

SEM photos of the worn surface of HNBR-pCBT 100-0 are shown in Figure 5.36. One can see that annealing at 250 °C does not change the wear mechanisms when comparing with HNBR-(p)CBT 100-0 (cf. Figures 5.36 and 5.33). The wear mechanisms of HNBR-pCBT hybrids are somewhat similar to those of HNBR-(p)CBT hybrids when containing the same amount of thermoplastic. Figure 5.37 shows the worn surface of HNBR-pCBT 100-100. Comparing the SEM pictures from the same

regions in Figures 5.34 and 5.37, one can observe that instead of large debris, smaller “ironed” wear particles appear after annealing. Though the wear initiation occurs by fatigue cracking (cf. especially Figure 5.37c), debris do not detach easily due to the semi-IPN structure present. This may account for the lower W_s of HNBR-pCBT compared to HNBR-(p)CBT hybrids. It has to be underlined that no recrystallized CBT could be found in the worn surfaces of HNBR-pCBT systems. Missing CBT crystals proves that CBT is mostly polymerized in the HNBR-pCBT hybrids, in fact.

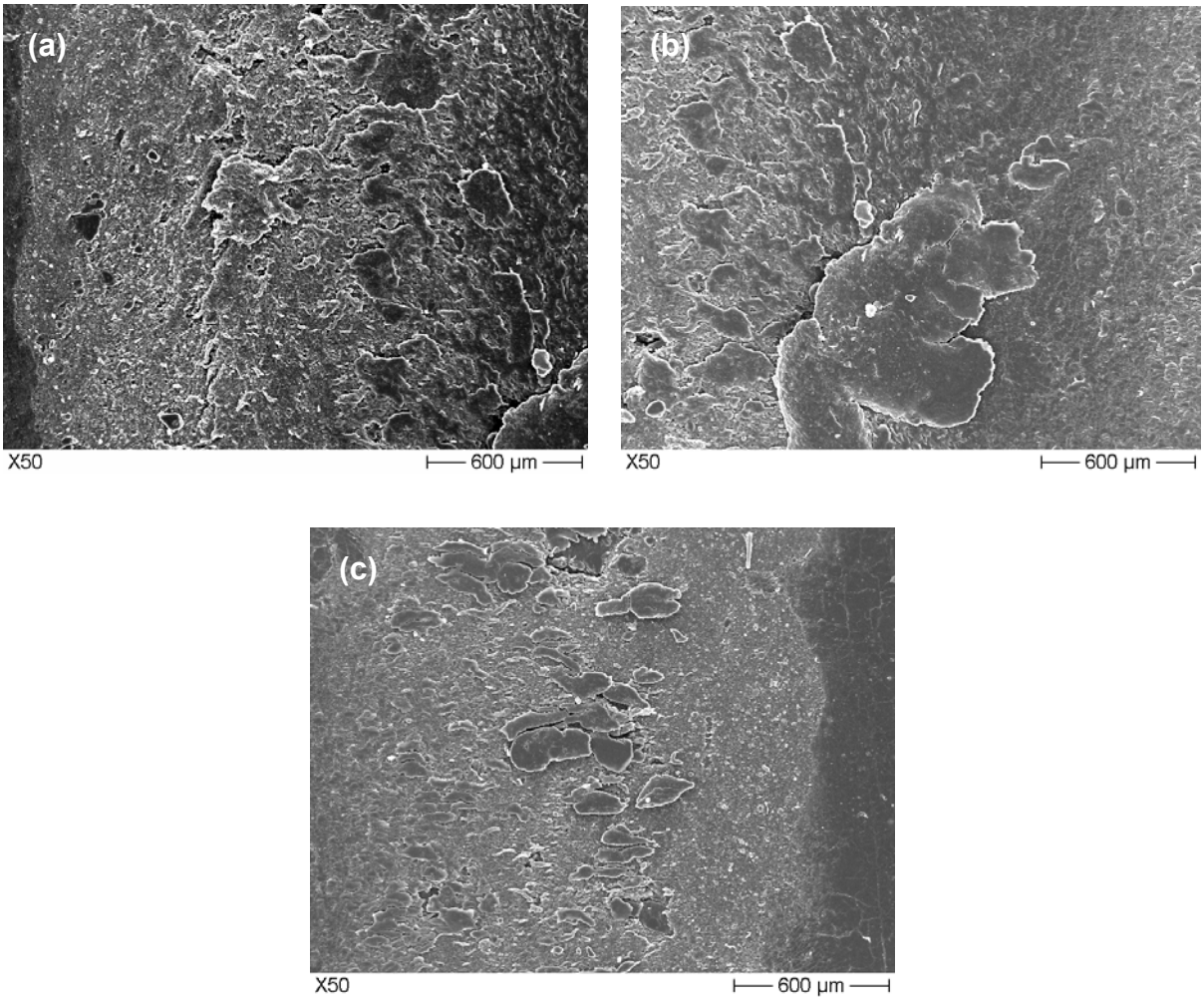

Figure 5.37 SEM photos taken from the rolling wear track of HNBR-pCBT 100-100 after Orbital-RBOP test. (a) outer region, (b) centre region, (c) inner region. Note: rolling direction is downward.

6 Finite element (FE) modelling of the friction

6.1 Model parameters for EPDM_30CB, HNBR-FKM 100-100 and HNBR-(p)CBT 100-100

EPDM_30CB, HNBR-FKM 100-100 and HNBR-(p)CBT 100-100 were selected as the sample materials in the simulation representing three types of elastomer compounds. The obtained parameters of 15-term Maxwell and Mooney-Rivlin Material Model are listed in Tables 6.1 and 6.2, respectively.

Table 6.1 Parameters of the 15-term Maxwell Model

EPDM_30CB				HNBR-FKM 100-100				HNBR-(p)CBT 100-100			
E [MPa], t [sec]				E [MPa], t [sec]				E [MPa], t [sec]			
E_0	3.70 $x10^{+03}$	E_∞	4.50 $x10^{+00}$	E_0	3.15 $x10^{+3}$	E_∞	2.30 $x10^{+00}$	E_0	3.37 $x10^{+03}$	E_∞	5.07 $x10^{+00}$
t(1)	1.61 $x10^{+03}$	e(1)	2.83 $x10^{-04}$	t(1)	7.45 $x10^{+4}$	e(1)	1.57 $x10^{-17}$	t(1)	4.24 $x10^{+10}$	e(1)	9.68 $x10^{-04}$
t(2)	1.29 $x10^{+01}$	e(2)	3.12 $x10^{-04}$	t(2)	3.16 $x10^{+02}$	e(2)	7.83 $x10^{-05}$	t(2)	3.24 $x10^{+08}$	e(2)	1.73 $x10^{-03}$
t(3)	1.53 $x10^{-01}$	e(3)	4.45 $x10^{-04}$	t(3)	1.39 $x10^{-01}$	e(3)	1.87 $x10^{-04}$	t(3)	1.51 $x10^{+06}$	e(3)	2.85 $x10^{-03}$
t(4)	9.89 $x10^{-04}$	e(4)	1.03 $x10^{-03}$	t(4)	8.21 $x10^{-04}$	e(4)	2.51 $x10^{-03}$	t(4)	1.39 $x10^{+04}$	e(4)	4.03 $x10^{-03}$
t(5)	1.18 $x10^{-06}$	e(5)	6.09 $x10^{-03}$	t(5)	1.48 $x10^{-05}$	e(5)	9.24 $x10^{-03}$	t(5)	6.68 $x10^{+01}$	e(5)	6.90 $x10^{-03}$
t(6)	8.51 $x10^{-09}$	e(6)	6.74 $x10^{-02}$	t(6)	1.14 $x10^{-07}$	e(6)	1.11 $x10^{-02}$	t(6)	2.89 $x10^{-01}$	e(6)	9.50 $x10^{-03}$
t(7)	1.42 $x10^{-10}$	e(7)	2.22 $x10^{-01}$	t(7)	9.94 $x10^{-10}$	e(7)	5.54 $x10^{-02}$	t(7)	1.94 $x10^{-03}$	e(7)	1.26 $x10^{-02}$
t(8)	1.80 $x10^{-12}$	e(8)	1.90 $x10^{-01}$	t(8)	1.46 $x10^{-11}$	e(8)	1.88 $x10^{-01}$	t(8)	2.58 $x10^{-05}$	e(8)	2.31 $x10^{-02}$
t(9)	1.27	e(9)	1.12	t(9)	2.16	e(9)	1.60	t(9)	4.57	e(9)	6.92

	$x10^{-14}$		$x10^{-01}$		$x10^{-13}$		$x10^{-01}$		$x10^{-07}$		$x10^{-02}$
t(10)	2.00 $x10^{-16}$	e(10)	5.07 $x10^{-02}$	t(10)	1.87 $x10^{-15}$	e(10)	1.10 $x10^{-01}$	t(10)	7.90 $x10^{-09}$	e(10)	1.64 $x10^{-01}$
t(11)	1.10 $x10^{-19}$	e(11)	6.91 $x10^{-02}$	t(11)	2.50 $x10^{-18}$	e(11)	8.56 $x10^{-02}$	t(11)	3.21 $x10^{-10}$	e(11)	1.86 $x10^{-01}$
t(12)	1.38 $x10^{-22}$	e(12)	4.59 $x10^{-02}$	t(12)	1.86 $x10^{-20}$	e(12)	7.49 $x10^{-02}$	t(12)	7.12 $x10^{-12}$	e(12)	1.31 $x10^{-01}$
t(13)	1.62 $x10^{-24}$	e(13)	8.62 $x10^{-02}$	t(13)	1.30 $x10^{-22}$	e(13)	7.91 $x10^{-02}$	t(13)	1.35 $x10^{-13}$	e(13)	1.12 $x10^{-01}$
t(14)	6.62 $x10^{-26}$	e(14)	6.76 $x10^{-02}$	t(14)	1.85 $x10^{-24}$	e(14)	1.11 $x10^{-01}$	t(14)	1.53 $x10^{-16}$	e(14)	1.10 $x10^{-01}$
t(15)	1.82 $x10^{-27}$	e(15)	7.87 $x10^{-02}$	t(15)	1.55 $x10^{-26}$	e(15)	1.11 $x10^{-01}$	t(15)	9.24 $x10^{-20}$	e(15)	1.65 $x10^{-01}$

Table 6.2 Parameters of the Mooney-Rivlin Material Model

	EPDM_30CB	HNBR-FKM 100-100	HNBR-(p)CBT 100-100
C_{10} [MPa]	493.33	420	448.71
C_{01} [MPa]	123.33	105	112.18

6.2 Orbital-RBOP

Because the normal load was applied by the leverage in the Orbital-RBOP test rig which vibrates up and down during the testing (cf. Figure 2.5), the measured data of normal force fluctuate in a small range.

Figure 6.1 shows the experimental and simulated normal, friction force and COF of EPDM_30CB under 170 N with 3 rpm of the ball. One can get the impression that the experimental and simulated results agree well with each other. Due to the numerical fluctuation of COF (cf. Figure 6.1b), the average experimental and simulating values in the single cycle were collected in Table 6.3 and compared. One can see that the average COF of experiment and simulation is very close to each other.

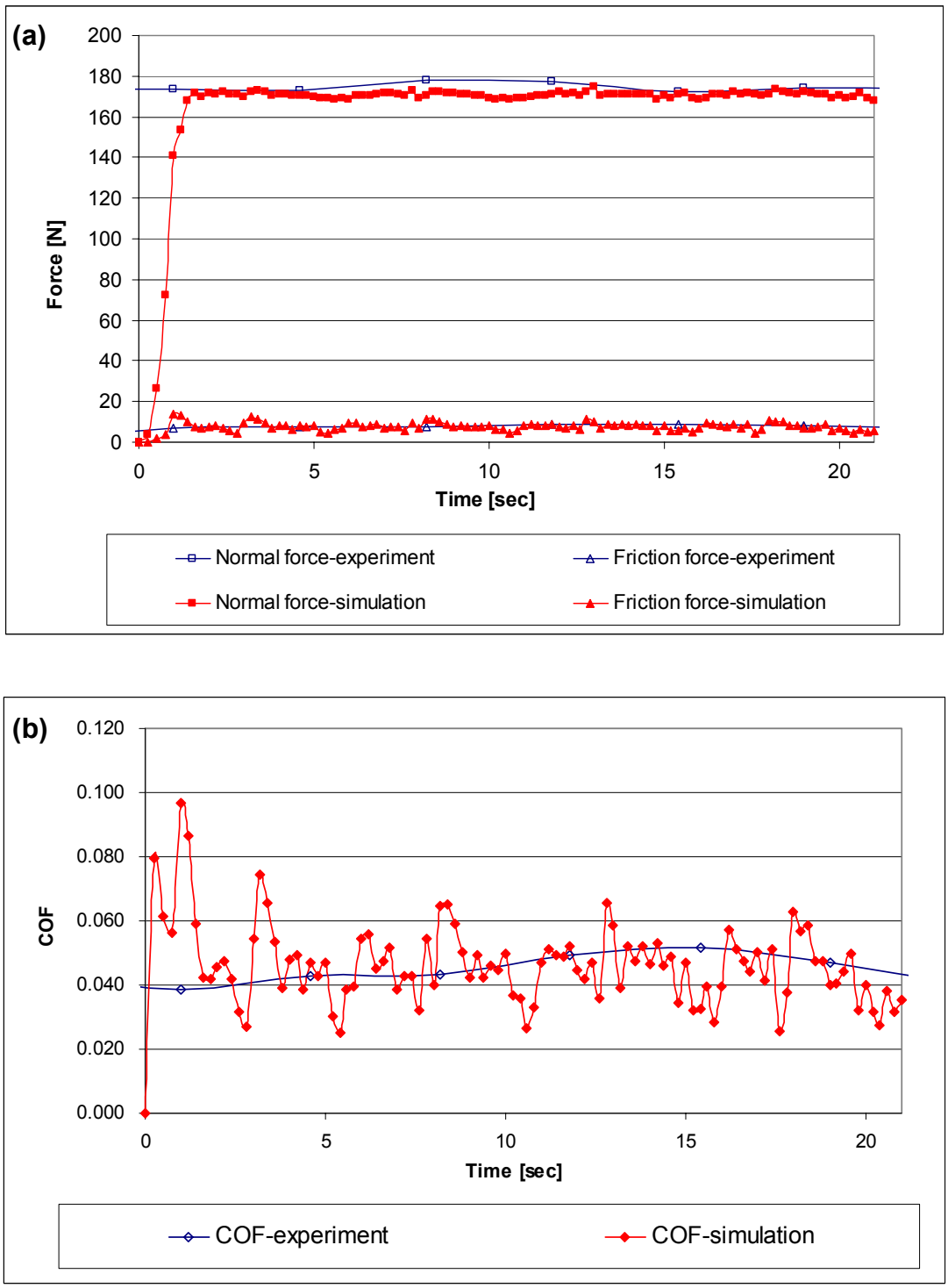

Figure 6.1 Experimental and simulated normal, friction force (a) and COF (b) for the EPDM_30CB under 170 N with 3 rpm of the ball in Orbital-RBOP.

For HNBR-FKM 100-100, the simulated friction force is a little bit higher than that of experimental one (cf. Figure 6.2a). This is the reason for the higher simulated COF compared to the experimental COF (cf. Table 6.3). The friction force and COF from simulation and experiment are in concert with each other for HNBR-(p)CBT 100-100 (cf. Figure 6.2b and Table 6.3).

Table 6.3 Average experimental and simulation COF in Orbital-RBOP

	EPDM_30CB	HNBR-FKM 100-100	HNBR-(p)CBT 100-100
Experiment COF	0.045	0.041	0.036
Simulation COF	0.046	0.069	0.034

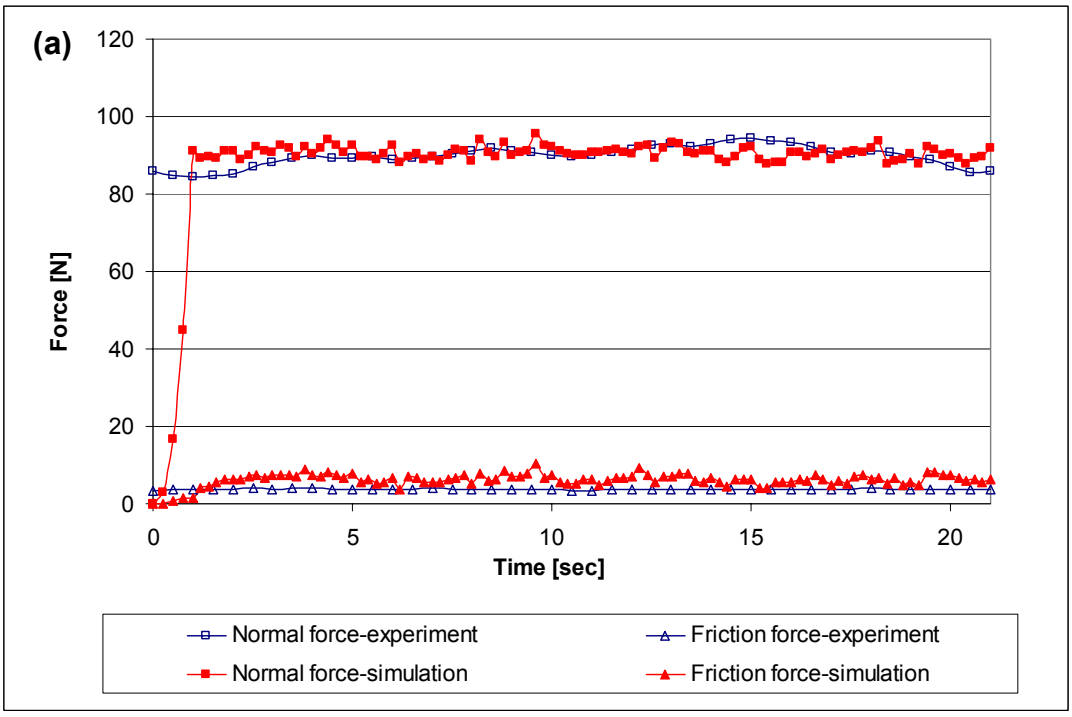

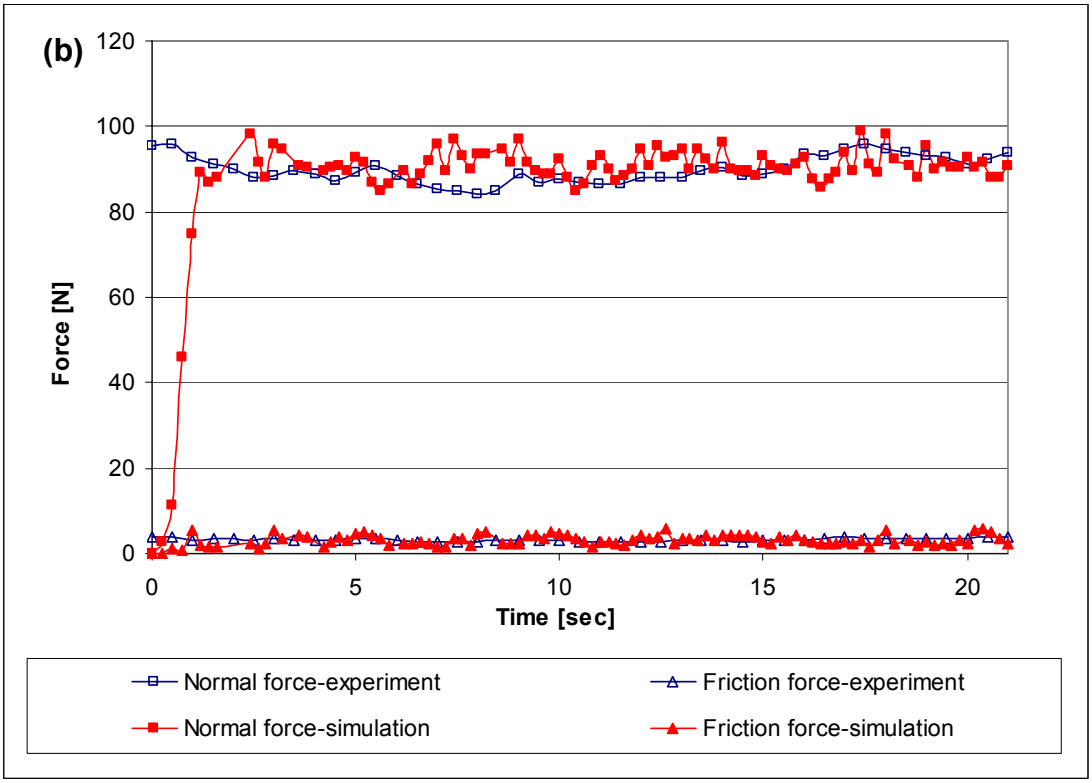

Figure 6.2 Experimental and simulated normal and friction force for HNBR-FKM 100-100 (a) and HNBR-(p)CBT 100-100 (b) under 90 N with 3 rpm of the ball in Orbital-RBOP.

6.3 Oscillating-RBOP

In this testing rig, when the ball moved in one direction, friction force was defined as positive; accordingly, when it rotated to the other direction, the force value turned to be negative. The normal force pressing the rubber surface was defined as minus.

Friction force, normal force and the calculated COF from the experiments and simulation of Oscillating-RBOP are shown in Figures 6.3-6.5. One can see that the friction force and COF of all the three representative rubber materials show good cyclic characteristic as a function of the direction of the ball's movement (positive in half a cycle, negative in the other half). The friction and normal force got from simulation for the EPDM_30CB correspond well with the experimental results (cf. Figure 6.3). The simulated COF of EPDM_30CB agrees very well with the experimental COF.

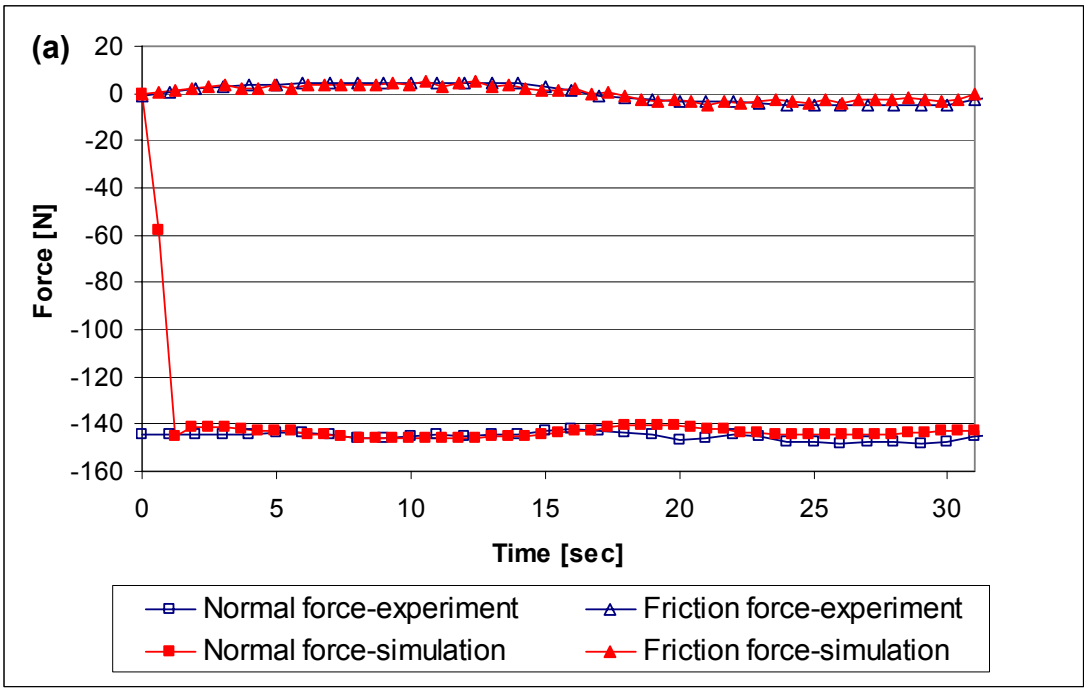

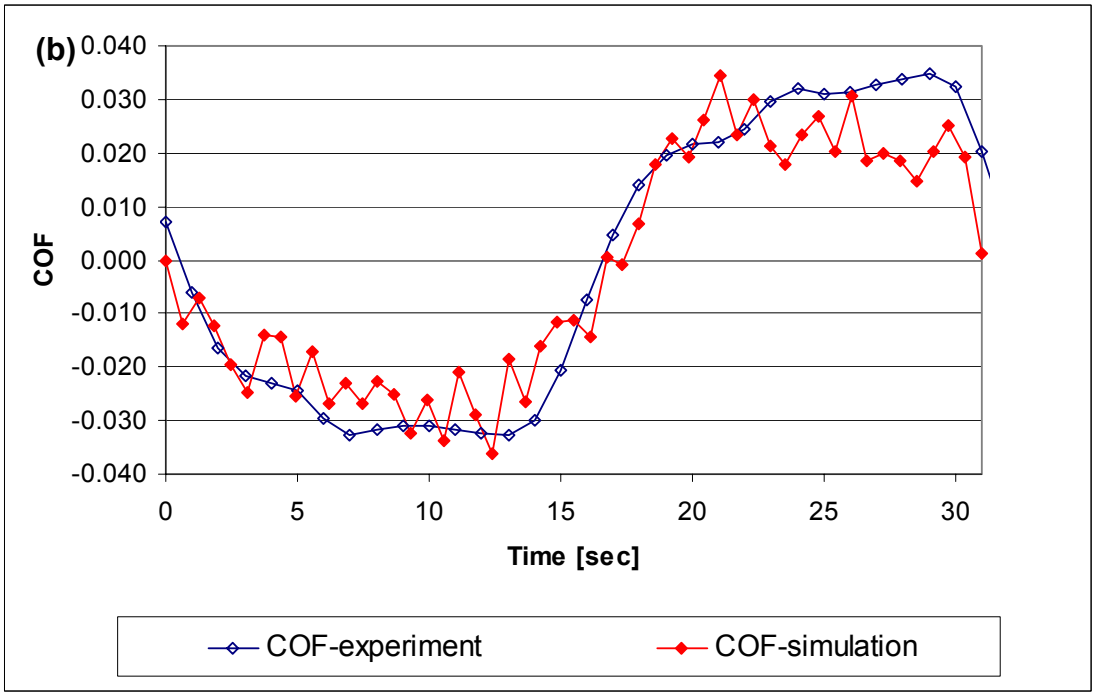

Figure 6.3 Experimental and simulated normal, friction force (a) and COF (b) for the EPDM_30CB under 140 N with 1/30 Hz in Oscillating-RBOP.

The simulation results for the HNBR-FKM 100-100 and HNBR-(p)CBT 100-100 are not as good as for the EPDM_30CB. The possible reason behind may be linked with the fact that the material parameters were not chosen properly (cf. Figures 6.4 and 6.5).

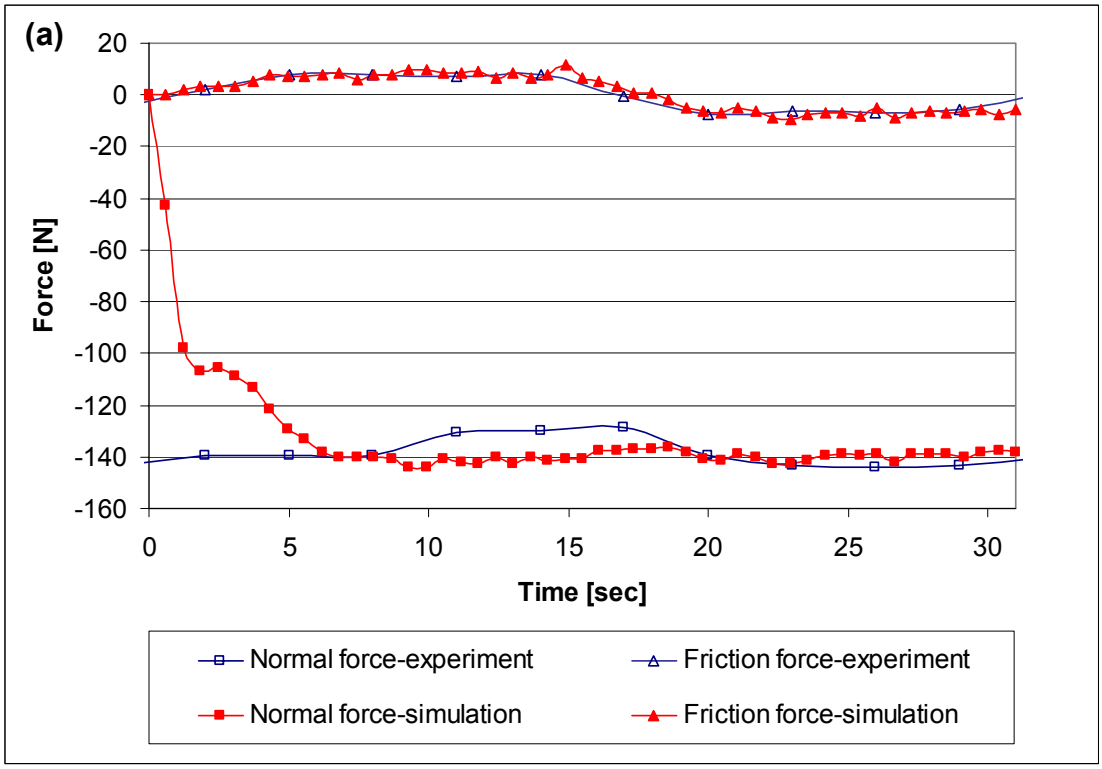

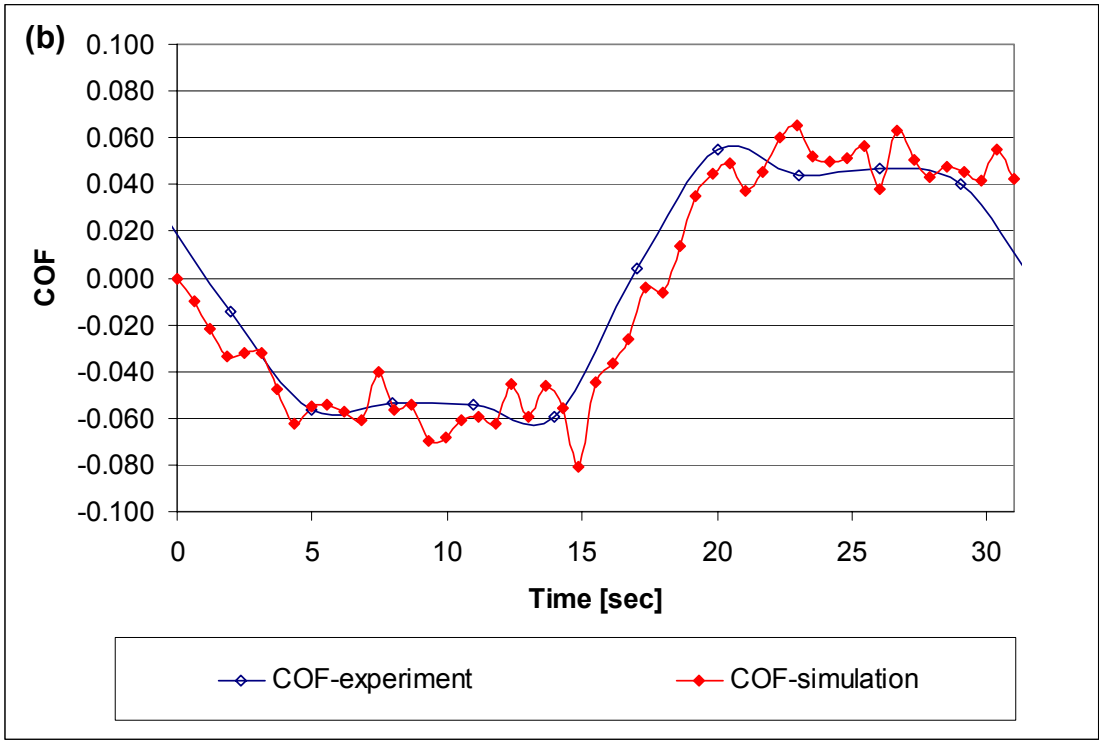

Figure 6.4 Experimental and simulated normal, friction force (a) and COF (b) for the HNBR-FKM 100-100 under 140 N with 1/30 Hz in Oscillating-RBOP.

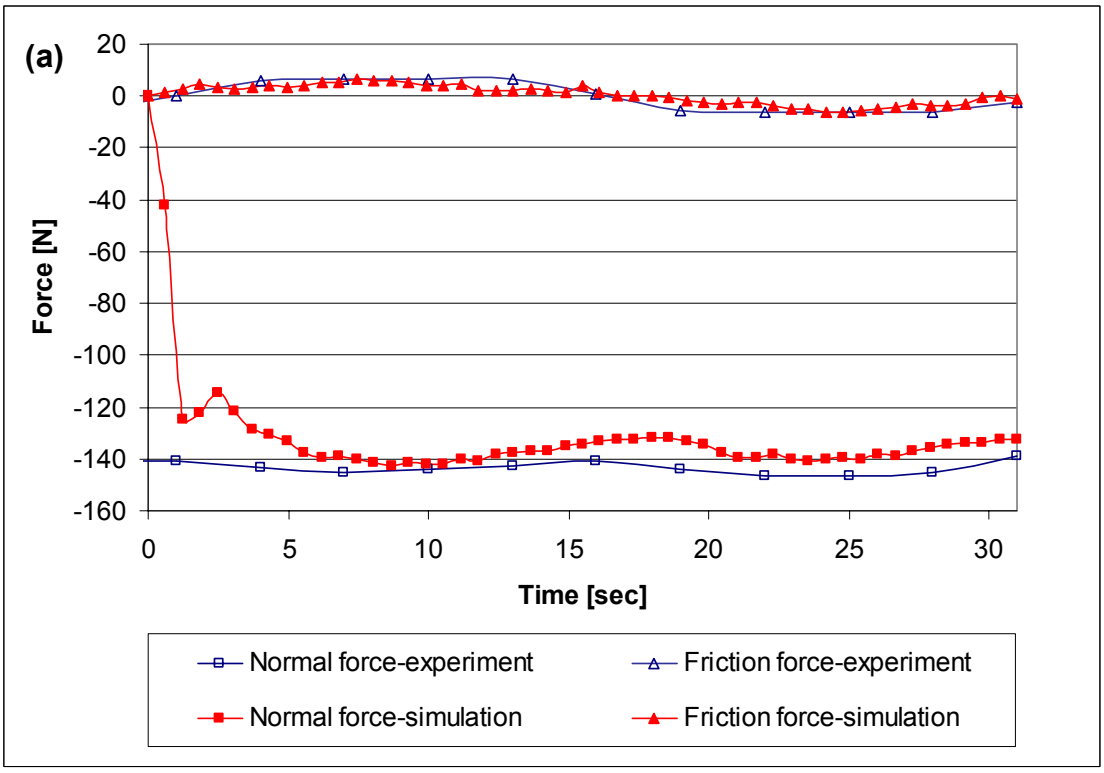

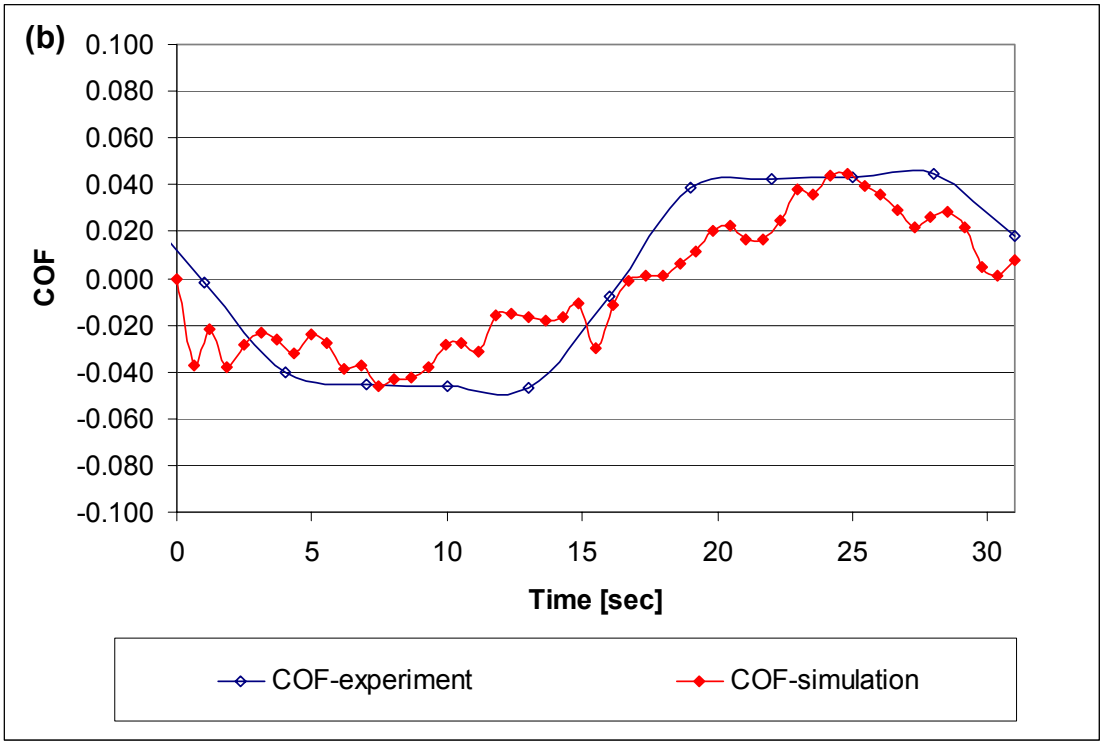

Figure 6.5 Experimental and simulated normal, friction force (a) and COF (b) for the HNBR-(p)CBT 100-100 under 140 N with 1/30 Hz in Oscillating-RBOP.

As stated above, the numerical fluctuation of COF was relatively large. By increasing the number of mesh elements in the FE-model and/or increasing the number of steps during the simulation may decrease this fluctuation; and improve further the accuracy of the calculations. However both of the listed refinements lead to an enormous increase of the CPU time (increase the calculation time greatly) or even make the calculation impossible due to reaching the computational limits.

The measurement of viscoelastic property of the rubber materials by DMTA measurements was successful. The viscoelastic behaviour of rubber materials can be described and handled by the Maxwell Material model with proper number of Maxwell elements. The agreement between the simulated and the experimental results for the different rubber compounds in different testing rigs demonstrates that the FE simulation is a useful tool to analyze the rolling process on the rubber plate and it can provide a good quantitative description of the rolling friction.

7 Summary

In this work, the unlubricated rolling friction and wear properties of various rubbery materials (EPDM_CB, HNBR_CB/silica/MWCNT, HNBR-FKM_MWCNT and HNBR-CBT) were studied in Orbital-RBOP and Oscillating-RBOP test configurations. The wear mechanisms were inspected by scanning electron microscopy (SEM). Differential scanning calorimetry (DSC), dynamic-mechanical thermal analysis (DMTA) and atomic force microscopy (AFM), etc., were adopted to determine the phase structures and network-related properties of the hybrids. The changes of the friction and wear as a function of type and amount of the additives were explored. The friction process of selected rubbers was also studied by the finite element method (FEM).

Experimental work:

1 Traditional elastomers:

1) effects of CB's content in EPDM,

Martens hardness of EPDM compounds increases with increasing CB content. Incorporation of CB increased marginally the COF and decreased the W_s. The COF in Orbital-RBOP configuration is larger than in Oscillating-RBOP, as lies in the movement of the ball. In Orbital-RBOP tests, Schallamach pattern appears in EPDM_30CB, but is less developed with further incorporation of CB. Fibrils are found in both Orbital-RBOP and Oscillating-RBOP rolling wear track of EPDM_CB system.

2) effects of fillers' content (silica/MWCNT) in HNBR,

With the increasing amount of filler the position of the glass transition temperature of the HNBR composites at -25 °C does not shift, but the stiffness in the rubbery stage of the composites increases. M_c decreases and v_c accordingly increases, with the increasing content of MWCNT and silica (exception is HNBR_10silica). The exception, i.e. HNBR_10silica has the worst crosslinking structure compared to other silica reinforced HNBR compounds and even the pure rubber. The density and the Martens hardness increase with the increasing amount of fillers (marginally for silica). The MWCNT filled HNBR compounds have higher hardness than the HNBR mixes added with the same amount of silica.

The COF changes marginally with the increasing content of silica/MWCNT. Using silica or MWCNT additives the wear resistance of the related HNBR mixes was mostly enhanced, compared to that of the pure HNBR, except HNBR_10silica. Increasing filler content raised the wear resistance of the compounds. The exception, i.e. HNBR_10silica has the smallest wear resistance compared to other silica reinforced HNBR and even the pure rubber likely due to its crosslinked structure. Incorporation of 10 phr MWCNT does not enhance the wear resistance prominently. When 20 phr fillers were added, the specific wear rate was reduced dramatically. However, only slight further decrease in W_s was found when the compounds contained more filler (i.e. 30 phr).

It is noticeable that the wear loss of the filler reinforced HNBR system correlates with the occurrence of the Schallamach type pattern. Its reduction/prohibition corresponds to a reduced W_s for both silica and MWCNT reinforcement. The introduction of active fillers (silica, MWCNT) may be the reason for the less development of the waves, as often observed in rubbery systems with active fillers.

3) effects of fillers' type (CB/silica/MWCNT) in HNBR,

The position of the glass transition temperature of the HNBR composites at -25 °C was not affected by the incorporation and type of the fillers. Introducing fillers in HNBR increased the stiffness in the rubbery stage of the composites, where the MWCNT's effect is much stronger than CB and silica. MWCNT has the strongest influence on the rubber-filler and filler-filler interactions among the fillers used. The Martens hardness of HNBR_20MWCNT is the highest among all HNBR compounds studied. CB, silica reinforced hardness too, but with a weaker effect than MWCNT.

Incorporating CB, silica and MWCNT lowered the W_s and slightly enhanced the COF. CB proved to be better in improving the rolling wear resistance of HNBR compared to silica and MWCNT. Silica and MWCNT have similar effect in reinforcing the rolling wear resistance of HNBR. The almost/completely disappeared Schallamach-type pattern in the wear tracks of filled HNBR system results in lower W_s compared to the pure HNBR.

2 Elastomer/Elastomer blend HNBR-FKM_MWCNT:

1) effects of MWCNT,

Incorporation of MWCNT increased the stiffness of HNBR-FKM compounds. They were two-phase systems: FKM was dispersed as micronscaled domains in the HNBR matrix where MWCNT is preferentially embedded. The position of T_g peaks of the rubbers was not affected by MWCNT modification. The apparent M_c decreased and v_c increased dramatically by adding MWCNT. Incorporation of MWCNT enhanced the density and the Martens hardness, reduced slightly the contact angle of the compounds.

The reinforcement of MWCNT in HNBR-FKM increased the friction and enhanced the wear resistance. The Schallamach wavy pattern disappears after MWCNT introduction. This change in the wear mechanism reflects a reduction in the specific wear rate, which was found also for other rubber-active filler systems (e.g. above rubber compounds). It can be quoted that the Schallamach-type wear diminishes with increasing reinforcement of a rubber independent of the type of the active filler used.

2) effects of FKM,

Incorporation of FKM reduced the E' of HNBR compounds. The position of T_g peaks of the rubbers did not change with the FKM blending. The E' and v_c reduction of the hybrids compared to that of HNBR can be traced to a change in the curing recipe (note that the curatives were reduced by increasing amount of the FKM in the HNBR/FKM mixes) and to a difference in the cure rates between HNBR and FKM. Incorporation of FKM into HNBR yielded reduction in the contact angle of the compounds.

The compounds of HNBR and FKM exhibited slightly higher COF and considerably lower W_s compared to the HNBR. The more FKM the compound contains, the higher the COF is. This tendency in COF can be traced to the change observed for the contact angles. Increasing wettability, represented by smaller contact angles, should be accompanied with increased adhesion during friction and thus manifest in enhanced COF. The W_s of HNBR-FKM with and without MWCNT changes marginally with increasing content of FKM. It is related to the dilution of the curing recipe and the irregularity in the dynamical mechanical response which does not follow the additivity rule in respect with the composition.

3 Elastomer/thermoplastic blend HNBR-(p)CBT/pCBT:

Effects of content and conversion of CBT

By contrast to bulk CBT, CBT did not polymerize at T= 190 °C for 25 min when incorporated in HNBR. Polymerization of CBT could be achieved, however, by annealing at T= 250 °C. The recrystallized CBT in the HNBR rubber, cured at T= 190 °C, worked as active filler and thus improved the modulus of the HNBR. Annealing of the hybrids resulted in a semi-IPN structure according to DMTA and AFM results.

Both (p)CBT (filler, dispersed in the HNBR) and pCBT (present as quasi-continuous phase) improved the resistance to unlubricated rolling wear. In this respect pCBT proved to be more beneficial than (p)CBT. COF went through a maximum as a function of the (p)CBT/pCBT content (at 50 phr of the latter) before reaching (HNBR-(p)CBT hybrids) or even falling below that of the plain HNBR (HNBR-pCBT hybrids). CBT crystals were found in the wear tracks of HNBR-(p)CBT hybrids. The introduction of (p)CBT inhibited the formation of the Schallamach pattern compared to HNBR-(p)CBT 100-0. Note that this is usually caused by increasing amount of active fillers, such as the above described rubbers. The wear mechanisms of HNBR-pCBT hybrids are somewhat similar to those of HNBR-(p)CBT hybrids when containing the same amount of thermoplastic. But the debris of HNBR-pCBT blends do not detach easily due to the semi-IPN structure present, which accounts for the lower W_s compared to HNBR-(p)CBT.

Simulation work (FEM):

EPDM _30CB, HNBR-FKM 100-100 and HNBR-(p)CBT 100-100 can represent three type of elastomers. The accordance of their FEM results in different test rigs with the experimental verification tells that this method can be used to investigate the complex mechanical behaviours of rubbery materials due to viscoelasticity with its precise quantitative description.

Based on the results obtained, the enhanced resistance to rolling wear associated with improved physico-mechanical properties of elastomers was realised by filler-reinforcing or blending. The simulation results on the blends can likely be refined by choosing more proper material parameters. Anther attention to FEM work will be the

simulation of pure EPDM and reinforced HNBR-FKM.

A further challenge is to find correlation between network-related or other parameters and tribological ones. The results in this work can be considered as part of a database which could be used for that purpose. Nonetheless, a relationship between microhardness and specific wear rate of filler reinforced rubbers has been proposed [102]. Next attention should be paid to the “generalization” of that correlation.

Appendix

The typical terms relative to the wear mechanisms used in the article and mechanisms representative figures or formation processes are as below:

1) Schallamach type pattern, wavy pattern- cf. Figure 7.1 (Figure 2.12).

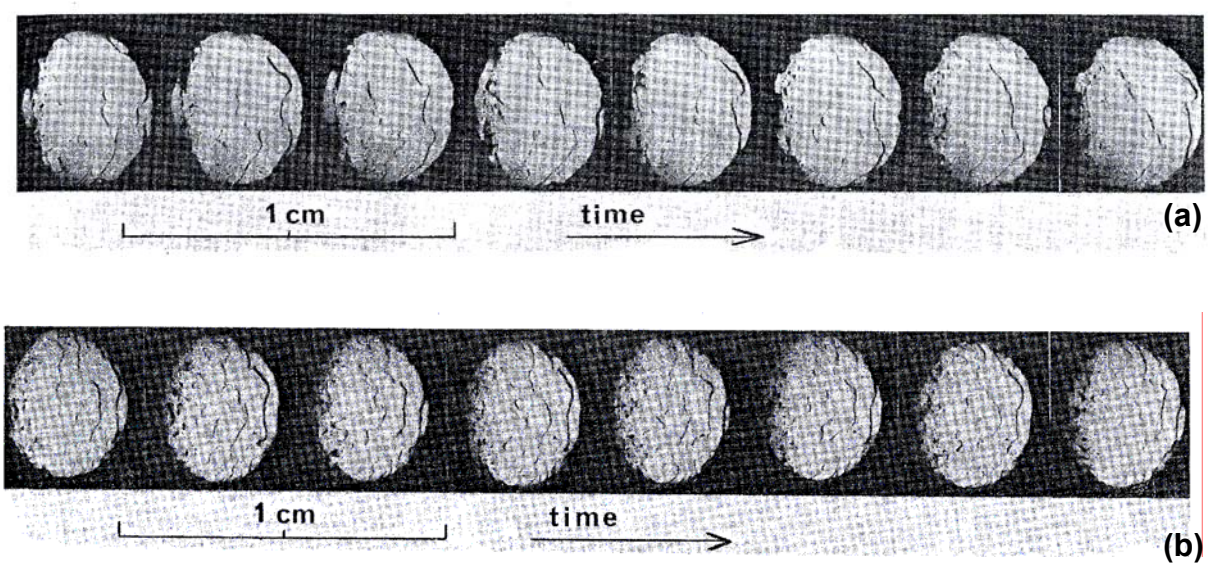

Figure 7.1 Eight frames at (1/32)s intervals of a film of the contact between (a) a transparent rubber track and a hard sphere, (b) a perspex plate and a natural rubber sphere.

2) abrasion- cf. Figure 7.2 (Figure 2.13).

Figure 7.2 Pattern abrasion of CB filled NR. Direction of abrasion: upward. Magn. 10.8 x.

3) cracks, cracking, pitting (events), holes, chipping, spalling- fatigue induced characteristics, cf. Figure 7.3 (Figure 2.14).

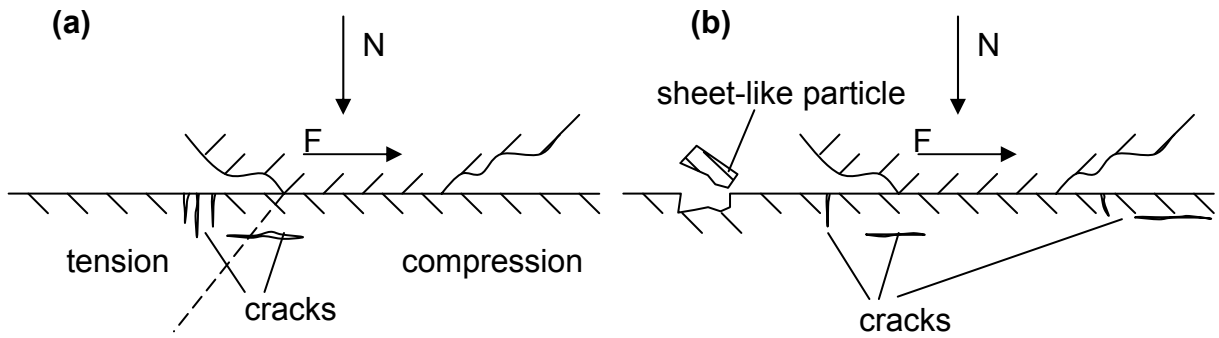

Figure 7.3 Characteristics of surface fatigue (a) and delamination (b) wear model.

4) roll formation, rollers- cf. Figure 7.4 (Figure 2.15).

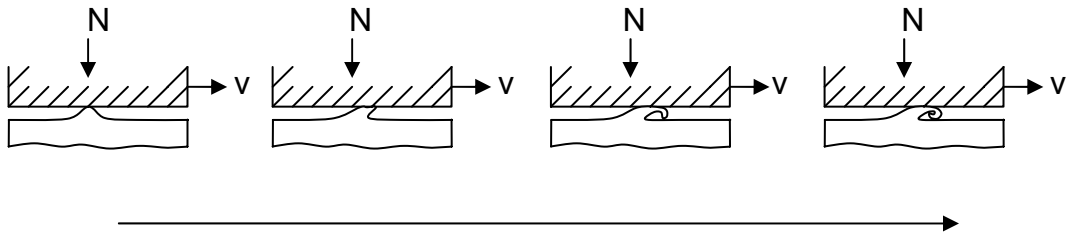

Figure 7.4 Wear by roll formation (v is velocity) [73].

5) fibrils- cf. Figure 7.5 (Figure 2.16).

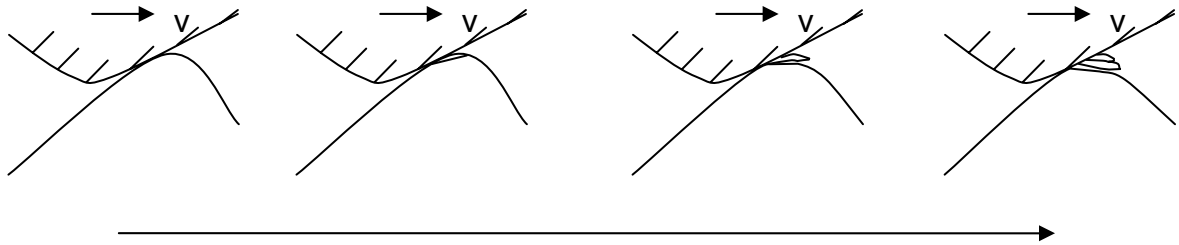

Figure 7.5 Adhesive wear [81].

6) debris, fragments, fragmentation, debris clustering, clusters from debris, agglomerates, particles- associated characteristic of other wear mechanisms, e.g. spalling.

7) ironing, flattened particles- cf. Figure 7.6.

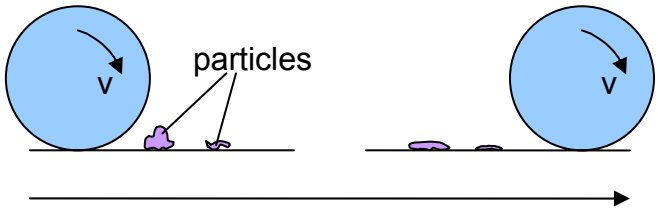

Figure 7.6 Ironing/flattened particles.

8) ploughing, tearing events- cf. Figure 7.7.

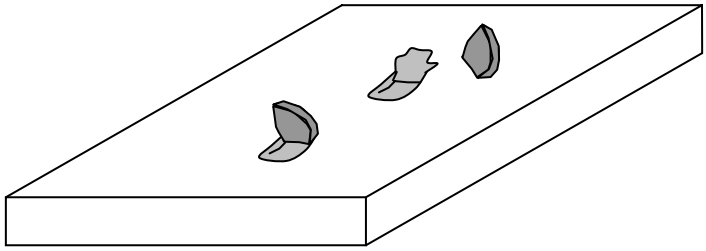

Figure 7.7 Ploughing, tearing events.

References

[1] Treloar, L. R. G.: The physics of rubber elasticity. Oxford University Press, Oxford, 2005, 1

[2] Loadman, M. J. R.: Analysis of rubber and rubber-like polymers. Kluwer Academic Publishers, London, 1998, 4-14

[3] http://en.wikipedia.org/wiki/Rubber. Accessed on 10. 05. 2009

[4] http://en.wikipedia.org/wiki/Synthetic_rubber#cite_ref-0. Accessed on 10. 05. 2009

[5] Felhös, D., Xu, D., Schlarb, A. K., Varadi, K., Goda T.: Viscoelastic characterization of an EPDM rubber and finite element simulation of its dry rolling friction. eXPRESS Polymer Letters, 2008, 2 (3), 157-164

[6] Kulkarni, S. M., Rubin, C. A., Hahn, G. T.: Elasto-plastic coupled temperature-displacement finite element analysis of two-dimensional rolling-sliding contact with a translating heat source. Journal of Tribology- Transactions of the ASME, 1991, 113 (1), 93-101

[7] Severin, D., Qiao, L.: The thermomechanical calculation of polymer roller with finite element method. In Advances in Computational Methods for Simulation (ed.: Topping, B. V. H.). Civil-Comp Press, Edinburgh, 1996, 73-77

[8] Bederna, C., Engst, W.: Analyse des Eindrück-Rollwiderstandes bei Gurtförderern mit der Methode der Finiten Elemente. KGK - Kautschuk Gummi Kunststoffe, 1998, 51 (10), 690-699

[9] Nagdi, K.: Rubber as an engineering material: guidelines for users. Hanser, Munich, 1993, 1-7

[10] http://en.wikipedia.org/wiki/Copolymer. Accessed on 10. 05. 2009

[11] Holden, G., Hansen, D. R.: Applications of thermoplastic elastomers. In Thermoplastic Elastomers (eds.: Holden, G., Kricheldorf, H. R., Quirk, R. P.). Hanser, Munich, 2004, 493-520

[12] Elias, H. -G.: Polymer adjuvants. An Introduction to Plastics. Second, completely revised edition. Wiley-Vch GmbH & Co. KGaA, Weinheim, 2003, 85-105

[13] Karger-Kocsis J.: Thermoplastic Rubbers via Dynamic Vulcanization. In Part 1: Compatibilization and Miscibility. Polymer Blends and Alloys (ed.: Shonaike, G. O., Simon, G. P.). Marcel Dekker, New York, 1999, 125-153

[14] Deanin, R. D., Manion, M. A.: Compatibilization of Polymer Blends. In Part 1: Compatibilization and Miscibility. Polymer Blends and Alloys (ed.: Shonaike, G. O., Simon, G. P.). Marcel Dekker, New York, 1999, 1-21

[15] Shaw, M. T., Aklonis, J. J., MacKnight, W. J.: Introduction to polymer viscoelasticity. Wiley & Sons, West Sussex, 2005

[16] Dick, J. S.: Vulcanizate physical properties, performance characteristics, and testing. In Rubber Technology: Compounding and Testing for Performance (ed.: Dick, J. S.). Hanser Gardner Publications, Cincinnati, 2001, 50-53

[17] Hamed, G. R.: Materials and Compounds. In Engineering with Rubber: How to Design Rubber Components (ed.: Gent, A. N.). Carl Hanser Press, Munich, 2001, 11-34

[18] http://en.wikipedia.org/wiki/Hysteresis. Accessed on 10. 05. 2009

[19] School, R.: Elastomer selection. In Rubber Technology: Compounding and Testing for Performance (ed.: Dick, J. S.). Hanser Gardner Publications, Cincinnati, 2001,132

[20] Slusarski, L., Bielinski, D. M., Affrossman, S., Pethrick, R. A.: Surface modification of elastomers to improve their tribological properties. KGK - Kautschuk Gummi Kunststoffe, 1998, 51 (6), 429-438

[21] Wildberger, A., Geisler, H., Schuster, R. H.: Modification of elastomer surfaces using atmospheric plasma. KGK - Kautschuk Gummi Kunststoffe, 2007, 60 (1-2), 24-31

[22] Majumder, P. S., Bhowmick, A. K.: Friction behaviour of electron beam modified ethylene–propylene diene monomer rubber surface. Wear, 1998, 221 (1), 15-23

[23] Zhang, S. W.: Tribology of elastomers. Tribology and Interface Engineering Series, No. 47. Elsevier, New York, 2004

[24] Khan; M. S., Lehmann, D., Heinrich, G., Gohs, U., Franke, R.: Structure-property effects on mechanical, friction and wear properties of electron modified PTFE filled EPDM composite. eXPRESS Polymer Letters, 2009, 3 (1), 39-48

[25] Bayer, R. G.: Wear analysis for engineers. HNB publishing, New York, 2002

[26] Elizabeth, K. I., Alex, R., Varghese, S.: Evaluation of blends of natural rubber and hydrogenated nitrile rubber containing chemically modified natural rubber. Plastics Rubber and Composites, 2008, 37 (8), 359-366

[27] Xu, D., Karger-Kocsis, J., Apostolov, A. A.: Hybrids from HNBR and in situ polymerizable cyclic butylene terephthalate (CBT): Structure and rolling wear properties. European Polymer Journal, 2009, 45 (4), 1270-1281

[28] Herrmann, W., Uhl, C., Heinrich, G., Jehnichen, D.: Analysis of HNBR-montmorillonite nanocomposites - Morphology, orientation and macroscopic properties. Polymer Bulletin, 2006, 57 (3), 395-405

[29] Felhös, D., Karger-Kocsis, J., Xu, D.: Tribological testing of peroxide cured HNBR with different MWCNT and silica contents under dry sliding and rolling conditions against steel. Journal of Applied Polymer Science, 2008, 108 (5), 2840-2851

[30] Huang, A. M., Wang, X. P., Jia, D. M., Li, Y. M.: Thermal stability and aging characteristics of HNBR/clay nanocomposites in air, water and oil at elevated temperature. E-Polymers, 2007, Article Number, 051

[31] Gatos, K. G., Karger-Kocsis, J.: Effect of the aspect ratio of silicate platelets on the mechanical and barrier properties of hydrogenated acrylonitrile butadiene rubber (HNBR)/layered silicate nanocomposites. European Polymer Journal, 2007, 43 (4), 1097-1104

[32] Lu, Y. L., Liu, L., Yang, C., Tian, M., Zhang, L. Q.: The morphology of zinc dimethacrylate reinforced elastomers investigated by SEM and TEM. European Polymer Journal, 2005, 41 (3), 577-588

[33] Yang, X., Giese, U., Schuster, R. H.: Characterization of permeability of elastomers - Part I - HNBR. KGK - Kautschuk Gummi Kunststoffe, 2008, 61 (6), 294-300

[34] http://www.sealseastern.com/PDF/FluoroAcsChapter.pdf. Accessed on 10. 05. 2009

[35] http://en.wikipedia.org/wiki/FKM. Accessed on 10. 05. 2009

[36] Hirano, K.; Suzuki, K.; Nakano, K.; Tosaka, M.: Phase separation structure in the polymer blend of fluorocarbon elastomer and hydrogenated nitrile rubber. Journal of Applied Polymer Science, 2005, 95 (1), 149-156

[37] Brunelle, D. J.: Synthesis and polymerization of cyclic polyester oligomers. In Modern Polyesters: Chemistry and Technology of Polyesters and Copolyesters (ed.: Scheirs, J., Long, T. E.). Chichester, Wiley, 2003, 117-142

[38] Mohd Ishak, Z. A., Shang, P. P., Karger-Kocsis, J.: A modulated DSC study on the in situ polymerization of cyclic butylene terephthalate oligomers. Journal of Thermal Analysis and Calorimetry, 2006, 84 (3), 637-641

[39] Parton, H., Baets, J., Lipnik, P., Goderis, B., Devaux, J., Verpoest, I.: Properties of poly(butylene terephthalate) polymerized from cyclic oligomers and its composites. Polymer, 2005, 46 (23), 9871-9880

[40] Harsch, M., Karger-Kocsis, J., Apostolov, A. A.: Crystallization-induced shrinkage, crystalline, and thermomechanical properties of in situ polymerized cyclic butylene terephthalate. Journal of Applied Polymer Science, 2008, 108 (3), 1455-1461

[41] Karger-Kocsis, J., Shang, P. P., Mohd Ishak, Z. A., Rösch, M.: Melting and crystallization of in-situ polymerized cyclic butylene terephthalates with and without organoclay: a modulated DSC study. eXPRESS Polymer Letters, 2007, 1 (2), 60-68

[42] Karger-Kocsis, J., Felhös, D., Bárány, T., Czigány, T.: Hybrids of HNBR and in situ polymerizable cyclic butylene terephthalate (CBT) oligomers: Properties and dry sliding behaviour. eXPRESS Polymer Letters, 2008, 2 (7), 520-527

[43] Wang, M. J.: Effect of filler-elastomer interaction on tire tread performance part III. KGK - Kautschuk Gummi Kunststoffe, 2008, 61 (4), 159-165

[44] Iijima, S.: Helical microtubules of graphitic carbon. Nature, 1991, 354 (6348), 56-58

[45] Xiong, J. W., Zheng, Z., Qin, X. M., Li, M., Li, H. Q., Wang, X. L.: The thermal and mechanical properties of a polyurethane/multi-walled carbon nanotube composite. Carbon, 2006, 44 (13), 2701-2707

[46] Wei, Z.; Zhao, Y. P.; Ruan, S. L.; Gao, P.; Yu, T. X.: A study of the tribological behavior of carbon-nanotube-reinforced ultrahigh molecular weight polyethylene composites. Surface and Interface Analysis, 2006, 38 (4), 883-886

[47] Jacobs, O.; Xu, W.; Schädel, B.; Wu, W.: Wear behaviour of carbon nanotube reinforced epoxy resin composites. Tribology Letters, 2006, 23 (1), 65-75

[48] Chen, H. Y.; Jacobs, O.; Wu, W.; Rudiger, G.; Schädel, B.: Effect of dispersion method on tribological properties of carbon nanotube reinforced epoxy resin composites. Polymer Testing, 2007, 26 (3), 351-360

[49] Enomoto, K.; Yasuhara, T.; Kitakata, S.; Murakami, H.; Ohtake, N.: Frictional properties of carbon nanofiber reinforced polymer matrix composites. New Diamond and Frontier Carbon Technology, 2004, 14 (1), 11-20

[50] Wang, C.; Dong, B.; Gao, G. Y.; Xu, M. W.; Li, H. L.: A study on microhardness and tribological behavior of carbon nanotubes reinforced AMMA-CNTs copolymer nanocomposites. Materials Science and Engineering A - Structural Materials Properties, Microstructure and Processing, 2008, 478 (1-2), 314-318

[51] Chen, W. X.; Li, F.; Han, G.; Xia, J. B.; Wang, L. Y.; Tu, J. P.; Xu, Z. D.: Tribological behavior of carbon-nanotube-filled PTFE composites. Tribology Letters, 2003, 15 (3), 275-278

[52] Du, J. H.; Bai, J.; Cheng, H. M.: The present status and key problems of carbon nanotube based polymer composites. eXPRESS Polymer Letters, 2007, 1 (5), 253-273

[53] Song, H. J.; Zhang, Z. Z.; Men, X. H.: Surface-modified carbon nanotubes and the effect of their addition on the tribological behavior of a polyurethane coating. European Polymer Journal, 2007, 43 (10), 4092-4102

[54] http://en.wikipedia.org/wiki/Vulcanization. Accessed on 10. 05. 2009

[55] Anes, J. M., Nase, R. S., White, C. H.: Use of plastics for parenteral packaging. In Pharmaceutical Dosage Forms: Parenteral Medications, Volume 1 (eds.: Avis, K. E., Lieberman, H. A., Lachman, L.). Informa Healthcare, London, 1992, 429-430

[56] Blau, P. J.: Friction Science and technology: from concepts to applications. Second edition. CRC Press, Boca Raton, 2009

[57] http://zhidao.baidu.com/question/51538072.html. Accessed on 10. 05. 2009

[58] http://en.wikipedia.org/wiki/Friction#cite_note-Meriam-4#cite_note-Meriam-4. Accessed on 10. 05. 2009

[59] http://www.i3721.com/xx/tbjak/s4nj/jjbzrd7c/200605/25754.html. Accessed on 10. 05. 2009

[60] Seireg, A. A.: Friction and lubrication in mechanical design. Marcel Dekker Inc, New York, 1998, 1-4

[61] Desaguliers, J. T.: Some experiments concerning the cohesion of lead, by the same. Philosophical Transactions, 1724, 33 (381-391), 345-347

[62] Bowden, F. P., Tabor, D.: The area of contact between stationary and between moving surfaces. Proceedings of the Royal Society of London Series A-Mathematical and Physical Sciences, 1939, 169 (938), 391-413

[63] Czichos, H.: Introduction to friction and wear. In Friction and Wear of Polymer Composites (ed.: Friedrich, K.). Composite Materials Series, Volume 1. Elsevier, New York, 1986.

[64] Gent, A. N., Henry, R. L.: Rolling friction on viscoelastic substrates. Transactions of the Society of Rheology, 1969, 13 (2), 255-271

[65] Greenwood, J. A., Tabor, D.: Deformation properties of friction junctions. Proceedings of the Physical Society Section B, 1955, 68 (9), 609-619

[66] Greenwood, J. A., Tabor, D.: The friction of hard sliders on lubricated rubber: the importance of deformation losses. Proceedings of the Physical Society, 1958, 71(6), 989-1001

[67] Greenwood, J. A., Minshall, H., Tabor, D.: Hysteresis losses in rolling and sliding friction. Proceedings of the Royal Society of London Series A- Mathematical and Physical Sciences, 1961, 259 (129), 480-507

[68] Tabor, D.: The mechanism of rolling friction. 2. The elastic range. Proceedings of the Royal Society of London Series A- Mathematical and Physical Sciences, 1955, 229 (1177), 198-220

[69] Evans, I.: The rolling resistance of a wheel with a solid rubber tyre. British Journal of Applied Physics, 1954, 5, 187-188

[70] May, W. D., Morris, E. L., Atack, D.: Rolling friction of a hard cylinder over a viscoelastic material. Journal of Applied Physics, 1959, 30 (11), 1713-1724

[71] Flom, D. G., Bueche, A. M.: Theory of rolling friction for spheres. Journal of Applied Physics, 1959, 30 (11), 1725-1730

[72] Halling, J.: Mechanics of rolling motion. In Principles of Tribology (ed.: Halling, J.). Macmillan Press, London, 1975, 182-198

[73] Sarkar, A. D.: Friction and wear. Academic Press, London, 1980

[74] Burwell, J. T.: Survey of possible wear mechanisms. Wear, 1957, 1(2), 119-141

[75] Suh, N. P.: Surface Interactions. In Tribological Technology (ed.: Senholzi, P. B.), Volume 1. Martinus Nijhoff, The Hague, 1982, 37-208

[76] Tabor, D.: Wear: a critical synoptic review. Journal of Lubrication Technology-Transactions of the ASME, 1977, 99 (4), 387-395

[77] Schallamach, A.: How does rubber slide? Wear, 1971, 17 (4), 301-312

[78] Schallamach, A.: Friction and abrasion of rubber. Wear, 1958, 1 (5), 384-417

[79] Fukahori, Y., Yamazaki, H.: Mechanism of rubber abrasion. 1. Abrasion pattern-formation in natural-rubber vulcanizate. Wear, 1994, 171 (1-2), 195-202

[80] Fukahori, Y., Yamazaki, H.: Mechanism of rubber abrasion. 2. General rule in abrasion pattern-formation in rubber-like materials. Wear, 1994, 178 (1-2), 109-116

[81] Kuhlmann-Wilsdorf, D.: Effects of local high pressures and extreme shears at tribological contact spots. Tribology Research: from Model, Experiment to Industrial Problem (ed.: Dalmaz, G., Lubrecht, A. A., Dowson, D., Priest, M.). Tribology Series, 39 (ed.: Dowson, D.). Elsevier, Amsterdam, 2001, 417-428

[82] Dealy, J. M., Larson, R. G.: Structure and rheology of molten polymers: from structure to flow behavior and back again. Hanser Gardner Publications, Cincinnati, 2006, 329

[83] Brinson, H. F., Brinson, L. C.: Polymer engineering science and viscoelasticity: an introduction. Springer, Berlin, 2007, 75-97

[84] Wineman, A. S., Rajagopal, K. R.: Mechanical response of polymers: an introduction. Cambridge University Press, Cambridge, 2000, 28-53

[85] Help Volume A: Theory of user information. MSC.MARC Product documentation. MSC Software Corporation, Version 2005, 2005

[86] Ferry, J. D.: Viscoelastic properties of polymers. John Wiley and Sons, New York, 1971

[87] http://en.wikipedia.org/wiki/Differential_scanning_calorimetry. Accessed on 10. 05. 2009

[88] Wetton, R. E.: Dynamic mechanical thermal analysis of polymers and related systems. In Developments in Polymer Characterisation (ed. Dawkins, J. V.). Springer, Berlin, 1986, 179-222

[89] Williams, D. B., Carter, C. B.: Transmission electron microscopy: a textbook for materials science. Kluwer Academic / Plenum Publishers, London, 1996

[90] Santer, S.: SEM and AFM: Complementary techniques for high resolution surface investigation. Presentation on 06. 07. 2004. http://www.imtek.uni-freiburg.de/cpi/images/images/vl-ofa/OFA-afm-sem.pdf

[91] Russell, P., Batchelor, D., Thornton, J.: SEM and AFM: Complementary Techniques for High Resolution Surface Investigations. Veeco Metrology Group. http://www.eetindia.co.in/ARTICLES/2002MAR/2002MAR25_DA_AN.PDF?SOURCES=DOWNLOAD

[92] Morita, S.: Introduction. In Noncontact Atomic Force Microscopy (eds.: Morita, S., Wiesendanger, R., Meyer, E.). Springer, Berlin, 2002, 1-10

[93] Wilkes, G. L., Stein, R. S.: Physicochemical approaches to the measurement of molecular anisotropy. In Structure and Properties of Oriented Polymers (eds.: Ward, I. M.). Springer Netherlands, Dordrecht, 1997, 59-69

[94] Pickover, C.: Archimedes to hawking. Oxford University Press, Oxford, 2008, 41-51

[95] Universalhärteprüfung, Deutsche Norm. 1997

[96] Kinloch, A. J.: Adhesion and Adhesives: science and technology. Springer Netherlands, Dordrecht, 1987, 18-51

[97] Dukhin, S. S., Kretzchmar, G., Miller, B.: Dynamics of adsorption at liquid interfaces. Series editors: Möbius, D., Miller, R. Elsevier, New York, 163-166

[98] Grundke, K.: Characterization of polymer surfaces by wetting and electrokinetic measurements-contact angle, interfacial tension, zeta potential. In Polymer Surfaces and Interfaces: Characterization, Modification and Applications (ed.: Stamm, M.). Springer, Berlin, 2007, 124-127

[99] Goldstein, J., Newbury, D., Joy, D., Lyman, C., Echlin, P., Lifshin, E., Sawyer, L., Michael, J.: Scanning electron microscopy and x-ray microanalysis. Springer Netherlands, Dordrecht, 2002

[100] Reimer, L.: Scanning electron microscopy: physics of image formation and microanalysis. Springer, Berlin, 1998

[101] Karger-Kocsis, J., Mousa, A., Major, Z., Békési, N.: Dry friction and sliding wear of EPDM rubbers against steel as a function of carbon black content. Wear, 2008, 264 (3-4), 357-365

[102] Xu, D., Karger-Kocsis, J., Schlarb, A. K.: Rolling wear of EPDM and SBR rubbers as a function of carbon black contents: correlation with microhardness. Journal of Materials Science, 2008, 43 (12), 4330-4339

[103] Felhös, D., Karger-Kocsis, J.: Tribological testing of peroxide-cured EPDM rubbers with different carbon black contents under dry sliding conditions against steel. Tribology International, 2008, 41 (5), 404-415

[104] Xu, D., Karger-Kocsis, J., Major, Z., Thomann, R.: Unlubricated Rolling Wear of HNBR/FKM/MWCNT Compounds Against Steel. Journal of Applied Polymer Science, 2009, 112 (3), 1461-1470

[105] Martínez, L., Álvarez, L., Huttel, Y., Méndez, J., Román, E., Vanhulsel, A., Verheyde, B., Jacobs, R.: Surface analysis of NBR and HNBR elastomers modified with different plasma treatments. Vacuum 2007, 81 (11-12), 1489-1492

[106] Ha, J. -W., Park, I. J., Lee, S. -B.: Hydrophobicity and sliding behavior of liquid droplets on the fluorinated latex films. Macromolecules, 2005, 38 (3), 736-744

[107] Ikeda, T.; Yamada, B.; Tsuji, M.; Skurai S.: In situ copolymerization behaviour of zinc dimethacrylate and 2-(N-ethylperfluoro-octanesulphonamido)ethyl acrylate in hydrogenated nitrile-butadadiene rubber during peroxide crosslinking. Polymer International, 1999, 48 (6), 446-454

[108] Barquins, M.: Adherence, friction and wear of rubber-like materials. Wear, 1992, 158 (1-2), 87-117

Publication List

Journals

1 Xu, D., Karger-Kocsis, J., Schlarb, A. K.: Rolling wear of EPDM and SBR rubbers as a function of carbon black contents: correlation with microhardness. Journal of Materials Science, 2008, 43 (12), 4330-4339

2 Karger-Kocsis, J., Felhös, D., Xu, D., Schlarb, A. K.: Unlubricated sliding and rolling wear of thermoplastic dynamic vulcanizates (Santoprene (R)) against steel. Wear, 2008, 265 (3-4), 292-300

3 Felhös, D., Karger-Kocsis, J., Xu, D.: Tribological testing of peroxide cured HNBR with different MWCNT and silica contents under dry sliding and rolling conditions against steel. Journal of Applied Polymer Science, 2008, 108 (5), 2840-2851

4 Xu, D., Karger-Kocsis, J., Schlarb, A. K.: Rolling friction and wear of organoclay-modified thermoplastic polyurethane rubbers against steel. KGK - Kautschuk Gummi Kunststoffe, 2008, 61 (3), 98-106

5 Felhös, D., Xu, D., Schlarb, A. K., Varadi, K., Goda, T.: Viscoelastic characterization of an EPDM rubber and finite element simulation of its dry rolling friction. eXPRESS Polymer Letters, 2008, 2 (3), 157-164

6 Xu, D., Karger-Kocsis, J., Apostolov, A. A.: Hybrids from HNBR and in situ polymerizable cyclic butylene terephthalate (CBT): Structure and rolling wear properties. European Polymer Journal, 2009, 45 (4), 1270-1281

7 Xu, D., Karger-Kocsis, J.: Unlubricated Rolling and Sliding Wear of Carbon Black Reinforced and In Situ Cured Polyurethane Containing EPDM Compounds against Steel. Journal of Applied Polymer Science, 2009, 115 (3), 1651-1662

8 Karger-Kocsis, J., Felhös, D., Xu, D.: Mechanical and tribological properties of rubber blends composed of HNBR and in situ produced polyurethane. Wear, 2009, in press

9 Xu, D., Karger-Kocsis, J., Major, Z., Thomann, R.: Unlubricated rolling wear of

HNBR/FKM/MWCNT compounds against steel. Journal of Applied Polymer Science, 2009, 112 (3), 1461-1470

10 Xu, D., Karger-Kocsis, J., Schlarb A. K.: Friction and wear of HNBR with different fillers under dry rolling and sliding conditions. eXPRESS Polymer Letters, 2009, 3 (2), 126-136

11 Xu, D., Karger-Kocsis, J.: Rolling and sliding wear properties of hybrid systems composed of uncured/cured HNBR and partly polymerized cyclic butylene terephthalate (CBT). Tribology International, 2010, 43 (1-2), 289-298

Conferences

1 Xu, D., Karger-Kocsis, J., Schlarb, A. K.: Unlubricated rolling wear of rubber/thermoplastic (HNBR/(p)CBT) compounds against steel. Tribologie-Fachtagung, Göttingen, 22-24.09.2008

Curriculum Vitae

Personal information

Name: Dan Xu

Born date: Nov.4th, 1980

Born place: Liaoning, China

Nationality: Chinese

Education

2006- PhD study, Institut für Verbundwerkstoffe GmbH (Institute for Composite Materials), University of Kaiserslautern, Germany

2003-2006 Master's degree in materials processing engineering, University of Science and Technology Beijing, China

1999-2003 Bachelor's degree in metallic materials engineering, University of Science and Technology Beijing, China

1996-1999 High School Liaohua, Liaoning, China

1992-1996 First Middle School Liaohua, Liaoning, China

1987-1992 Third Primary School Liaohua, Liaoning, China